2003

Development and modeling of iron-gallium alloys

Rick Allen Kellogg
Iowa State University

Development and modeling of iron-gallium alloys

by

Rick Allen Kellogg

A dissertation submitted to the graduate faculty

in partial fulfillment of the requirements for the degree of

DOCTOR OF PHILOSOPHY

Major: Engineering Mechanics

Program of Study Committee:
Alison B. Flatau, Major Professor
Arthur E. Clark
Thomas A. Lograsso
J.Adin Mann III
Ambar K. Mitra
Alan M. Russell

Iowa State University

Ames, Iowa

2003

Graduate College
Iowa State University

This is to certify that the doctoral dissertation of

Rick Allen Kellogg

has met the dissertation requirements of Iowa State University

Signature was redacted for privacy.

Committee Member

Signature was redacted for privacy.

Committee Member

Signature was redacted for privacy.

Committee Member

Signature was redacted for privacy.

Committee Member

Signature was redacted for privacy.

Committee Member

Signature was redacted for privacy.

Major Professor

Signature was redacted for privacy.

For the Major Program

TABLE OF CONTENTS

ACKNOWLEDGEMENTS

Many people deserve recognition for their contributions, which made it possible for me to complete this dissertation. I was fortunate to have the support of a superb Ph.D. committee: Dr. Alison Flatau, Dr. Art Clark, Dr. Thomas Lograsso, Dr. Adin Mann, Dr. Ambar Mitra and Dr. Alan Russell. I owe special thanks to my major professor Alison Flatau for encouraging me to pursue my Ph.D. work, and for her unwavering confidence and steady guidance throughout the research and academic process. I was privileged to collaborate with Art Clark and greatly appreciate his insights to magnetism as well as his thoughtful advice. Working closely with Tom Lograsso and Alan Russell on the material science aspects of this research was a wonderful learning experience. I am grateful to Marilyn Wun-Fogel for her support throughout my graduate career. I greatly appreciate the contributions of Dr. Shu-Fan Cheng and Dr. Fran Laabs for their crystallographic analysis efforts and the assistance by Dr. Bill McCallum with powder metallurgy. Dr Steve Martin and Dr. Steve Poling deserve thanks for contributing laboratory resources. I appreciate the accommodations made by Ames Lab and the Material Processing Center headed by Larry Jones to facilitate material production and analysis. Amy Ross, Lanny Lincoln and Scott Hoover all deserve recognition for lending their time, knowledge and expertise in the material processing efforts. Undergraduate students Nick LaPointe, Nick Burgart and Troy LaPointe made outstanding efforts toward the design and construction of laboratory test equipment, which proved essential to the success of this research. The assistance provided by AEEM technicians Tom Elliot and Bill Rickard and the secretarial staff was essential to completion of my degree. I would like to recognize the financial support provided by the Office of Naval Research through the "Graduate Traineeship Award" with oversight by Dr. Jeffrey Simmen and Jan Lindberg, as well as NSWC Carderock, Office of Basic Energy Sciences and the National Science Foundation. I am grateful to Iowa State University and the Department of Aerospace Engineering and Engineering Mechanics for providing academic and administrative support. Finally, I'd like to thank my friends and family for their generous patience and support extended throughout the duration of my Ph.D. program.

ABSTRACT

Alloys of iron substituted with non-magnetic gallium (Galfenol) appear promising as mechanically robust actuator/sensing materials. They offer desirable properties including tensile strengths and magnetostrictive strains, respectively, on the order of 100 MPa and 100 $x10^{-6}$. To advance the understanding of these materials, this dissertation examines the alloys' magnetic and mechanical response as a function of applied magnetic field, mechanical stress, temperature, stoichiometry and crystallographic morphology. Characterizations of the alloys' single-crystal magnetostrictive, elastic and plastic properties are used to facilitate the development and modeling of polycrystalline forms of the material having preferred crystallographic orientations (i.e. texture). The polycrystalline forms have potentially higher production yields and superior mechanical properties over those of single crystals. Iron-gallium alloys textured by different manufacturing processes reveal which production methods result in the most desirable magnetostrictive and mechanical performance envelopes. Growth and deformation processing techniques such as directional solidification, extrusion, forging and rolling were used to impart a variety of different texture distributions. Single-crystal tensile test were used to determine the material's elastic constants, yield stress, slip systems and their critical resolved shear stress as well as ultimate strength and percent elongation. Observations of the single-crystal alloys' remarkable in-plane auxeticity (or negative Poisson's ratio) and quadratic correlations of the Poisson's ratio magnitude to the level of gallium substitution are reported. Potential applications based on in-plane auxeticity are explored. Elastic properties, as determined from tensile testing on single-crystal specimens, provided the basis for the development and use of a Magnetostrictive Micromechanics Finite-Element Model (MMFEM) that captured the coupled magnetic and mechanical behavior of polycrystalline specimens. The MMFEM correctly reflects the bulk magnetostrictive capability of polycrystalline specimens having well-characterized texture distributions and provides a tool for predicting the magnetostrictive performance of textures yet to be produced.

1. INTRODUCTION

1.1 Motivations for magnetostrictive material research

Magnetostrictive materials are distinguished by the phenomenon of dimensional changes occurring with changes in magnetization. Consistent with le Chatelier's principle, magnetostrictive materials also experience an inverse effect where magnetization changes accompany changes in applied stress. Since James Joule's 1842 discovery of magnetostriction in iron, extensive work has been undertaken to develop and use magnetostrictive materials for actuation and sensing devices. Examples of magnetostrictive materials include the common ferromagnetic materials Fe, Ni and Co, which have maximum magnetostrictive strain magnitudes on the order of 10 $x10^{-6}$ m/m [Lee 1955]. Additionally, high performance rare earth-Fe_2 alloys such as Terfenol-D ($Tb_{0.3}Dy_{0.7}Fe_2$) have been developed that generate "giant" magnetostrictive strains on the order of 1000 $x10^{-6}$ [Clark 1980]. Considering any of these magnetostrictive materials for use in actuation and sensing applications under harsh mechanical conditions, we are left with a shortfall. None possess the combined desired properties of mechanical toughness and appreciable magnetostrictive strain capability simultaneously. Although polycrystalline Fe, Ni and Co have favorable mechanical properties with elongations exceeding 20% and tensile strengths more than 250 MPa, their magnetostrictive strain capabilities are small [Metals Handbook 1948]. And while the rare earth-Fe_2 alloys develop giant magnetostrictive strains they, suffer from brittleness and low tensile strengths of roughly 28 MPa [Butler 1988].

The prospect of developing a mechanically robust magnetostrictive material has motivated this research effort. Providing the focus for this research, previous work has shown that alloys of iron substituted with non-magnetic gallium (Fe-Ga alloys are also known as Galfenol) appear promising in filling the role as a mechanically robust material with substantial magnetostrictive capability [Clark 2000c]. In preliminary tests, as cast polycrystalline $Fe_{83}Ga_{17}$ has been shown to endure tensile stresses up to 440 MPa with strains approaching 0.25% before failure [Lograsso 2000]. Furthermore, studies of single crystal $Fe_{83}Ga_{17}$ have shown the alloy to exhibit "large" magnetostrictive strains on the order of 100 $x10^{-6}$ with low saturating fields of several hundred oersteds as well as displaying a limited

temperature dependence over a -20 to 80°C range [Cullen 2001, Kellogg 2002, Clark 2002a, Clark 2000b]. Assuming the magnetostrictive properties of single crystal Fe-Ga alloy may be generated in a polycrystalline form having a high degree of crystallographic orientation, the alloy's combined attributes are particularly attractive from the perspective of transducer design for shock prone environments. Additional benefits of Fe-Ga alloys include substantially lower material costs than rare-earth based magnetostrictive alternatives and the potential for high-yield production of polycrystalline forms. Raw material cost for $Fe_{81}Ga_{19}$ is approximately $0.08/g and it might be produced by rapid deformation processing of bulk quantities (Chapter 2). For comparison, Terfenol-D ($Tb_{27}Dy_{73}Fe_{195}$) raw material cost is approximately $0.50/g and current production techniques utilize carefully controlled crystal growth processes [Snodgrass 2003]. A final consideration in the manufacture and use of the Fe-Ga alloys is that they are not toxic and do not required any special handling.

1.2 Crystallography

The Fe-Ga alloys to be examined in this work possess a body centered cubic (BCC) α-Fe structure with the gallium atoms randomly substituted throughout the lattice structure (hence the "α" prefix) as depicted in Figure 1.1a. Polycrystalline metals are often isotropic due to their overall random crystallographic distribution, however single crystal and strongly textured polycrystalline BCC metals exhibit a high degree of anisotropy in their physical characteristics. As the mechanical and magnetic properties of Fe-Ga alloys are inherently anisotropic with respect to the crystal lattice, a brief review of the Miller indices nomenclature will facilitate later discussions on the directional magnetic, elastic and plastic behaviors of interest.

Miller indices are used to identify a specimen's crystallographic orientation and the inherently directionally dependent responses arising from a given state of loading. Grouped Miller indices of a particular fiber direction and families of equivalent fiber directions are represented as the vectors $[u\ v\ w]$ and $\langle u\ v\ w \rangle$, respectively. Similarly, a plane surface is denoted by the notation $(h\ k\ l)$ with indices representing the plane-normal vector. The family of equivalent planes is given as $\{h\ k\ l\}$. Representative of a Fe-Ga alloy, Figure 1.1b shows a schematic of the BCC structure indicating several fiber directions (i.e. vectors relative to the

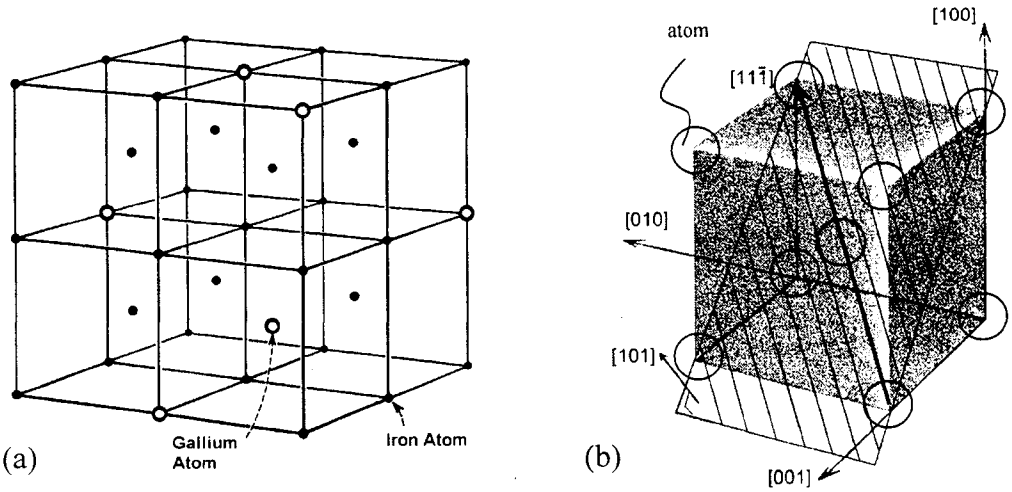

Figure 1.1 a) Iron BCC crystal lattice with randomly substituted gallium. b) Schematic of BCC crystal with the crystallographic nomenclature for the (101) plane, and [11$\bar{1}$] and <100> fiber directions highlighted.

material coordinate system) and a (101) plane. The positive Cartesian axes are coincident with three of six possible vectors from the <100> fiber group while the negative axes are coincident with the other three. The highlighted [11$\bar{1}$] fiber lies within the (101) plane and is one of the eight-member <111> fiber group. The (101) plane is one of twelve belonging to the {110} family of planes. (Note that the "{110}" designation is arbitrary and could also be written as {101}, {011} etc.) Sheet textures are defined by the combination of a plane-normal vector and a direction vector. For example the notation "(001)<100>" represents a cube sheet texture. In this case, the plane of the sheet surface is normal to the <001> direction and the crystallographic axes of all grains within the sheet are collectively aligned into the <100> direction.

Directional descriptions of magnetostrictive strain λ also adhere to the Miller indices nomenclature. For example the constants λ_{100} and λ_{111} refer to the material properties of saturation magnetostriction in the <100> and <111> family fiber directions respectively. Although all material properties in a particular family of fiber direction are equivalent, the value of magnetostriction measured in any particular fiber direction is dependent to a first approximation on the prevailing state of magnetization. The precise relationships between the directionality of material properties, magnetization and magnetostriction will be examined in the next section.

1.3 Magnetization and magnetostriction

The general magnetization and magnetostrictive processes of ferromagnetic materials are described first to provide a foundation for the mathematical modeling of magnetostriction. Thereafter, the theory representing the anisotropic magnetostrictive properties of cubic crystals is discussed, since it can be used to quantify the magnetostrictive properties of Fe-Ga alloys. With a fundamental description of the magnetization and magnetostrictive processes in hand, a review of the literature on nonmagnetic species substitution in iron, with an emphasis on gallium-substituted iron and the effect of stoichiometry, is presented. In conclusion, the piezomagnetic relationships describing the magnetic and mechanical coupling of magnetostrictive materials are provided as basis for understanding the output characteristics of magnetostrictive transducers and sensors.

1.3.1 Ferromagnetic processes

Ferromagnetic materials exhibit two regimes of magnetostriction. The first one, spontaneous magnetostriction denoted by λ_o, is the strain that occurs upon cooling of a ferromagnetic material through its Curie temperature. At temperatures above the Curie temperature, thermal energy disrupts the collective alignment of magnetic moments and prevents the formation of magnetic domains. As the specimen is cooled below the Curie temperature, the Weiss mean field (i.e. the imaginary internal magnetic field said to facilitate long-range ordering of moments) promotes magnetic moments to transition from an unordered paramagnetic state into a collection of randomly oriented domains accompanied by spontaneous magnetostriction. For isotropic materials, this spontaneous magnetostriction is one-half that of saturation magnetostriction, which will be discussed next. The Curie temperature of the gallium substituted α-iron alloys is in the neighborhood of 675°C [Kubaschewski 1982].

The second regime of magnetostriction, which is most pertinent to the operation of actuation and sensing devices, occurs below the Curie temperature where magnetization changes arise from applied magnetic fields. The process of magnetostriction may be described in a classical sense where it is assumed that a material's crystal lattice spacing is dependent on the orientation of the local magnetic moment. (Similarly, the lattice spacing

dependence exists over broader regions where the collectively oriented moments compose a magnetic domain.) The crystal lattice is spatially elongated in the direction of the magnetic moment's (or domain's) magnetization vector assuming that a positive material magnetostriction constant exists in this direction. Accompanying the lattice elongation, a strain of opposite sign occurs in the direction transverse to the magnetization vector as a consequence of volume conservation. The end result is asymmetrical lattice spacing with the material's strain being determined by orientation of the magnetic moments. Should all the magnetic moments become aligned, thus forming a single domain in the direction of the applied magnetic field, little further magnetostriction is possible. Relative to the zero strain state of a demagnetized specimen, this maximum strain condition is called technical saturation magnetostriction and is denoted by λ_s. Beyond the point of technical saturation forced magnetostriction does occur with high levels of applied magnetic field. Forced magnetostriction is a small effect that accompanies a reduction in the thermally induced precession of magnetic moments about the applied field direction.

The magnetization and magnetostriction response of a ferromagnetic material having a positive magnetostriction constant in the direction of magnetization are summarized graphically in Figure 1.2a and Figure 1.2b respectively. Following the initial response to the applied field H (from the origin), in stage I, as reversible magnetization slowly increases from zero with partial magnetization, magnetostrictive strain also increases slowly. Stage II follows with a rapid increase in irreversible magnetization due to domain wall motion. (Domain wall motion describes the translation of a domain boundary where the growth of one domain occurs at the expense of a neighboring domain.) Accompanying this rapid magnetization, magnetostriction also progresses rapidly to form the "burst region" of the magnetostrictive response. With stage III, magnetization and magnetostriction increase at a diminishing rate as moments rotate reversibly into alignment with the applied magnetic field. At this point, magnetization and magnetostriction reach their technical saturation values of M_s and λ_s respectively. Beyond technical saturation magnetization and technical saturation magnetostriction, slight increases in magnetization and magnetostriction occur as magnetic moments are forced out of precession into complete alignment with the applied field. After the initial response to increasing H, cyclic field application results in stable hysteretic

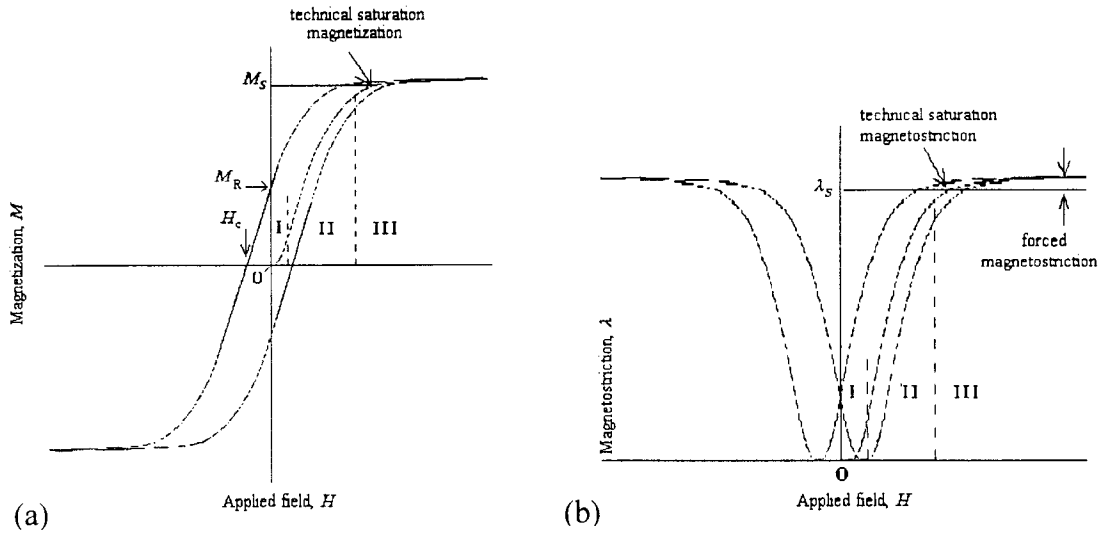

Figure 1.2. Simulated (a) magnetization and (b) magnetostriction curves of a ferromagnetic material to the initial application of an applied magnetic field H.

magnetization and magnetostriction loops. Key points on the magnetization plot include the remanent magnetization M_R and coercive field H_c. M_R corresponds to the material's residual magnetization at zero H and H_c. indicates the field required to drive the magnetization to zero [Cullity 1972].

Magnetization values are given in units of amps/meter (A/m). Additionally, the magnetic field H possesses units of amps/meter (A/m) or oersted (Oe) where 79.58 A/m = 1 Oe. Either unit for H will be used interchangeably through out this document.

Related to the M versus H curve, the magnetic flux density (or magnetic induction) B, having units of tesla, is often used to express a material's magnetic response to applied fields. Induction and magnetization follow the simple relation $B = \mu_o(M+H)$, where the constant $\mu_o = 4\pi \times 10^{-7}$ Henry/m is the permeability of free space. Similar to Figure 1.2a, a B versus H curve would have a remnant induction B_R and coercive field H_c, however no saturation value of B exists, as it would continue to increase with increasing magnetic field at a rate of $\mu_o H$ even though a maximum value of M has been attained.

1.3.2 Anisotropic magnetization and magnetostriction of cubic crystals

The different curvatures of the magnetization plot, like the one shown in Figure 1.2a, reflect anisotropy (i.e. directional dependence) in the magnetic properties of the material.

anisotropies. Magnetocrystalline and magnetostrictive anisotropy are intrinsic properties of the material. On the other hand, stress anisotropy arises from the coupling of these two properties, and is manifested as the magnetomechanical effect. The nature of these anisotropies is discussed next in terms of the material's energy state. The section will conclude with an expression describing anisotropic magnetostriction for saturation magnetization conditions.

There are three important crystallographic directions reflected in the magnetocrystalline anisotropy of cubic crystals. Previous work has shown for iron that the <100>, <110> and <111> directions, respectively, are considered to be the magnetically "easy", "medium" and "hard" directions [Honda 1926]. That is to say, arriving at the saturation magnetization value M_S (M_S is a material constant without respect to direction) via different directions of magnetization, requires different levels of applied field H. M_S is reached with a low H in the <100> direction, an intermediate H is required in the <110> direction and a high H is necessary in the <111> direction. Figure 1.3 shows a schematic of the magnetization response to an applied field for iron.

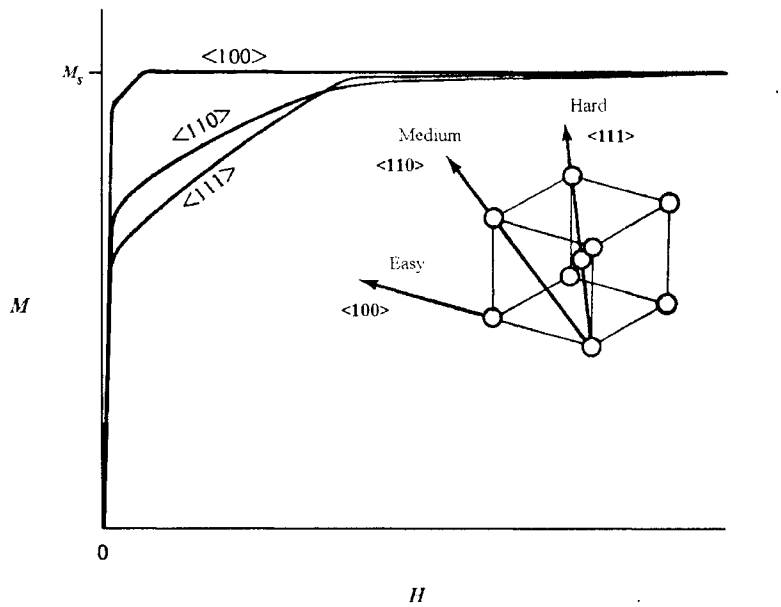

Figure 1.3 Magnetization curves for various directions of an iron cubic single crystal [Honda 1926].

The magnetocrystalline anisotropy that causes these various magnetization curves acts as a force tending to hold the magnetic moments (or domains), and hence the magnetization vectors, in alignment with the magnetically easy crystallographic directions. An applied field must do work to rotate the magnetization vector away from an easy axis. The material converts this work to crystal anisotropy energy E_a. The crystal anisotropy energy for a cubic system (Equation 1.1) is expressed as a series expansion in terms of the three direction cosines α_i that M_s makes relative to the crystallographic axes. The magnetic anisotropy constants K_0, K_1, K_2, ... are material dependent and have units of energy/volume. The higher order terms may generally be neglected [Cullity 1972].

$$E_a = K_0 + K_1\left(\alpha_1^2\alpha_2^2 + \alpha_2^2\alpha_3^2 + \alpha_3^2\alpha_1^2\right) + K_2\left(\alpha_1^2\alpha_2^2\alpha_3^2\right) + \ldots \qquad (1.1)$$

Using Equation 1.1 and the appropriate direction cosines, the magnetocrystalline energies for M_s having <100>, <110> and <111> directions are respectively K_0, $(K_0 + K_1/4)$ and $(K_0 + K_1/3 + K_2/27)$. Bozorth has shown that for cubic crystals with magnetically easy axes, as is observed in iron, if $K_0 = 0$, then K_1 must be positive and K_2 is limited to a range between $-K_1/4$ and $+\infty$ [Bozorth 1951].

Stress anisotropy also contributes to the energy balance of a crystal through the magnetoelastic energy E_{me}. E_{me} arises from the directional dependence of M_s interacting with anisotropic crystal strains, which are induced by a stress σ as given by the expression:

$$E_{me} = -\frac{3}{2}\lambda_{100}\sigma\left(\alpha_1^2\gamma_1^2 + \alpha_2^2\gamma_2^2 + \alpha_3^2\gamma_3^2\right) - 3\lambda_{111}\sigma\left(\alpha_1\alpha_2\gamma_1\gamma_2 + \alpha_2\alpha_3\gamma_2\gamma_3 + \alpha_3\alpha_1\gamma_3\gamma_1\right) \qquad (1.2)$$

The magnetostrictive strain constants λ_{100} and λ_{111} are material specific and the direction cosines γ_i are defined by the direction of applied stress relative to the crystallographic axes. Notation for stress follows the usual convention where σ is positive for tension.

The total energy state for a region of constant M_s may be determined with E_a and E_{me} provided that the external applied magnetic field energy E_m (Equation 1.3) is also known. E_m accounts for the coupling between the applied magnetic field H and M_s where Ω is the angle between them.

$$E_m = -\mu_o M_s H \cos\Omega \tag{1.3}$$

Through minimization of the sum of E_a , E_{me} and E_m, the equilibrium energy state of the material may be found for static applied magnetic field and stress conditions. If the directions of applied stress and magnetic field are known, the direction cosines for the saturation magnetization vector may be determined. Knowledge of the saturation magnetization direction ultimately becomes useful for determining a material's state of magnetostriction, as will be explained next.

Lee derives a theory for the anisotropic magnetostriction of single crystals using two material constants as a first approximation in modeling the saturation magnetostriction. A derivation of this model is given by Lee [Lee 1955]. The equilibrium strain state of a crystal is determined by minimization of the sum of a crystal's anisotropic magnetic, magnetostrictive and elastic energies. The significant result of this theory is given in Equation 1.4, which provides the saturation magnetostriction λ_s, for a cubic crystal magnetized to saturation from an ideal demagnetized state. The direction cosines α_i and β_i represent the saturation magnetization and strain measurement directions relative to the crystal axes respectively. The magnetostriction constants λ_{100} and λ_{111} are material properties to be identified experimentally.

$$\lambda_s = \frac{3}{2}\lambda_{100}\left(\alpha_1^2\beta_1^2 + \alpha_2^2\beta_2^2 + \alpha_3^2\beta_3^2 - \frac{1}{3}\right) + 3\lambda_{111}\left(\alpha_1\alpha_2\beta_1\beta_2 + \alpha_2\alpha_3\beta_2\beta_3 + \alpha_3\alpha_1\beta_3\beta_1\right) \tag{1.4}$$

From a practical standpoint it difficult to achieve an ideal demagnetized state in a specimen with any certainty, however Equation 1.4 remains quite useful. For example, the net change in magnetostriction in the [100] crystal direction may be calculated for a change in the saturation magnetization vector from one that is initially perpendicular ($\perp$) into one that is parallel ($\parallel$) with the [100] direction. This is equivalent to taking the [100] direction magnetostriction generated by a saturating applied magnetic field in the [100] direction minus the [100] direction magnetostriction generated by a saturating applied magnetic field in the [010] direction:

for $\lambda_\perp$ the direction cosines are $\alpha_2 = 1$, $\alpha_1 = \alpha_3 = 0$ and $\beta_1 = 1$, $\beta_2 = \beta_3 = 0$

for $\lambda_{\|}$ the direction cosines are $\alpha_1 = 1,\ \alpha_2 = \alpha_3 = 0$ and $\beta_1 = 1,\ \beta_2 = \beta_3 = 0$ substituting these values gives:

$$\lambda_{\|} - \lambda_{\perp} = \frac{3}{2}\lambda_{100}\left(1+0+0-\frac{1}{3}\right) + 3\lambda_{111}(0+0+0) - \left[\frac{3}{2}\lambda_{100}\left(0+0+0-\frac{1}{3}\right) - 3\lambda_{111}(0+0+0)\right]$$

$$\lambda_{\|-\perp} = \lambda_{\|} - \lambda_{\perp} = \frac{3}{2}\lambda_{100}.$$

The net magnetostriction result of $(3/2)\lambda_{100}$ calculated above is also the solution for any 90°change in the direction of the M_s vector into one parallel with the [100] direction and is a measure of the material's maximum usable magnetostriction. In transducer applications having ideal performance, the magnetic moments are prealigned orthogonally to the [100] actuation direction by compressive stress, through the minimization of E_{me}, and an applied magnetic field is used to rotate the M_s vector, through the minimization of E_m, 90° into the [100] direction. However, the real performance of these magnetostrictive elements typically falls short of $(3/2)\lambda_{100}$ maximum potential due to a lack of 90° moment rotation. Full 90° rotation for all moments is not achieved since the material's finite geometry and internal demagnetization effects induce complex domain structures through energy minimization. These domain structures are difficult to overcome and inhibit complete moment alignment in the orthogonal directions by the compressive stress.

The relationships for λ_s (Equation 1.4) may also be extended to the analysis of magnetostriction in polycrystalline cubic materials through volume integration, however assumptions regarding uniform stress or strain between differently oriented grains must be carefully considered to achieve useful results [Cullity 1972]. A finite element model addressing grain interactions that arise from saturation magnetostriction will be described in Chapter 5.

1.3.3 Magnetostriction in Fe-Ga alloys

Investigations into the physical behaviors of iron and iron substituted with various non-magnetic species preceded the development of gallium substituted iron-based alloys as a magnetostrictive material. Considering the magnetostrictive response in nearly pure iron, work by Tatsumoto in 1959 demonstrated the effect of temperature on the anisotropic

magnetostriction constants in BCC single crystal iron where the iron exhibits anomalous behaviors. In this case, measurements showed that the directional saturation magnetostrictions λ_{100} ranged between 21 $x10^{-6}$ and 23 $x10^{-6}$ and that λ_{111} increased from -25 $x10^{-6}$ to -20 $x10^{-6}$ as the temperature was increased from -100 °C to +100 °C [Tatsumoto 1959]. With these results in mind, a subsequent analysis on the effect of species substitution in iron was quite surprising. Work by R.C. Hall examined the room temperature anisotropy and magnetostriction of single crystal BCC iron substituted with non-magnetic elements including V, Cr, and Al. Hall's results showed reductions in the magnetocrystalline anisotropy constant K_1 (making the material easier to magnetize in the <100> directions) for additions of Al up to 17 atomic percent (at. %). Commensurate with these substitutions, saturation magnetostrictions increased with $\lambda_{100} \sim 85$ ppm and $\lambda_{111} \sim 0$ for the 17 at. % substitution levels [Hall 1959]. Hall also showed similar results for substitutions of V and Cr [Hall 1960]. The overall trend with these non-magnetic substitutions in iron was for a decrease in magnetocrystalline anisotropy and a significant increase magnetostriction. In short, larger magnetostrictions could be achieved in substituted iron with lower applied magnetic field levels.

Building on this prior work, the investigation of gallium substitution in iron by Clark *et al.* led to the development of Galfenol (Ga – gallium, fe-iron, and nol – Naval ordinance laboratory) as a prospective magnetostrictive transducer/sensing material. This magnetostrictive alloy is a single-phase solid solution with a disordered substitution of Ga in BCC α-Fe as depicted in Figure 1.1a. Typical compositions are $Fe_{100-x}Ga_x$ where $13 \leq x \leq 19$. These alloys have recently been shown to exhibit large magnetostrictions, with some approaching 400 $x10^{-6}$ at room temperature. The saturation magnetostriction (λ_{100}) is over 10-fold that of non-substituted Fe, yet the rhombohedral magnetostriction (λ_{111}) remains almost unchanged [Clark 2000c]. The binary phase diagram of Figure 1.4 shows that Ga substitutions up to ~17 at. % will retain a disordered equilibrium state down to 300°C. Given a decline in the rate of diffusion with decreasing temperature, this disordered state is maintained at room temperature as well. However, above ~17 at. % Ga ordered intermetallics such as the $D0_3$ and B_2 structures may form. This ordering will later be shown to be an

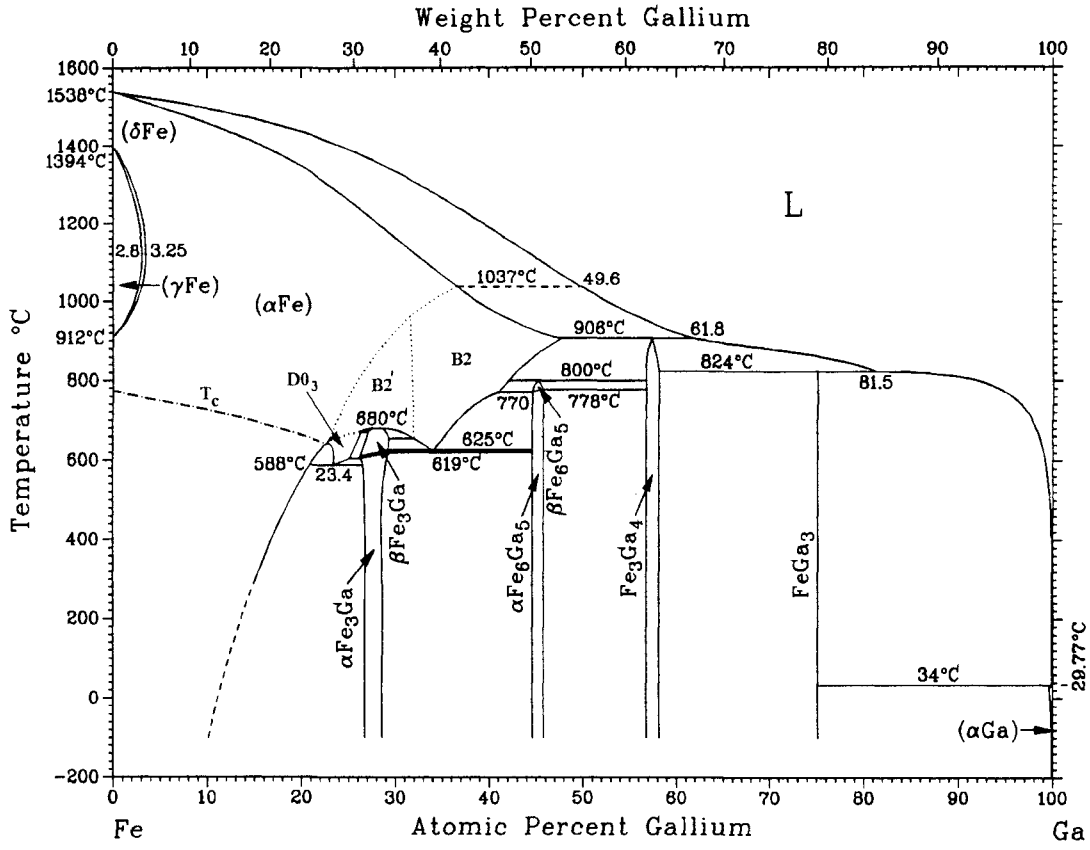

Figure 1.4 Binary Fe-Ga phase diagram [after Kubaschewski 1982, Massalski 2002]. Detail above 30% Ga has been omitted. Symbols including γ, α, DO_3, B_2, β ... represent different crystallographic structures. See an introductory text on material science for further explanation; for example [Barrett 1952].

important factor in limiting the alloy's magnetostrictive capability. Heat treatments such as quenching from 1000°C are often used to maintain a disordered Ga distribution for substitutions levels between 17 and 19 at. %.

The effect of Ga concentration on the experimentally determined magnetostrictive constants λ_{100} and λ_{111} for Fe-Ga single crystals at room temperature is shown in Figure 1.5. The 3/2 factor for the ordinate values reflect the magnetostrictions measured due to rotation of M_s from an orthogonal direction into one of final alignment with the [100] or [111] direction of interest. (i.e. the net strain in the [100] direction is 150% that of λ_{100}.) There is a prominent double peak in $(3/2)\lambda_{100}$ with Ga concentration. Additionally, quenching markedly

increases $(3/2)\lambda_{100}$ over that of furnace cooled alloys for Ga concentrations between ~17 and 22 at. %. The quenching benefit is achieved by avoiding $D0_3$ and B2 crystal structures [Clark 2001]. This ordering phenomenon and disruption of the magnetostrictive response has been observed before in aluminum-substituted iron [Hall 1959, Birkenbeil 1961]. The measured values of $(3/2)\lambda_{111}$ show significant increases with increasing Ga concentration up to 27 at. %. However, the $(3/2)\lambda_{111}$ dependence is particularly sensitive in the 17 to 20 at.% range where $(3/2)\lambda_{111}$ changes sign. The values of λ_{100} and λ_{111}, determined from Figure 1.5, will later be used in a model predicting the saturation magnetostriction capability of polycrystalline Fe-Ga alloys.

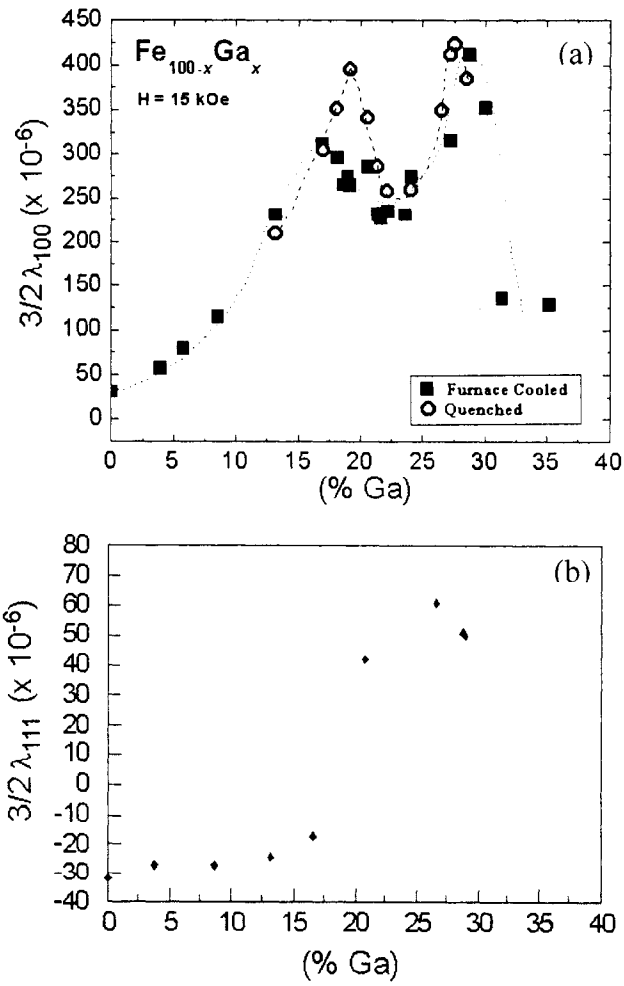

Figure 1.5 Magnetostrictive constants for Fe-Ga single crystal alloys as a function of at.% Ga concentration. a) $(3/2)\lambda_{100}$ for quenched and furnace cooled heat treatments, b) $(3/2)\lambda_{111}$ for furnace cooled heat treatment. [Clark *et al.* 2003].

The broad application of magnetostrictive Fe-Ga alloys as a transduction material requires knowledge of its characteristics for various temperature and stress conditions. Studies of single crystal $Fe_{83}Ga_{17}$ have shown the alloy to exhibit large saturation magnetostrictions with $(3/2)\lambda_{100} \geq 300$ ppm for temperatures ranging from -95° to + 22°C. Departing from iron's anomalous λ_{100} magnetostrictive behavior, Fe-Ga alloys show consistent decreases in $(3/2)\lambda_{100}$ with temperature that approximately follow an $M_s(T)^3$ relationship, where T is in kelvin. Figure 1.6a, from Clark's study, shows these results for single crystal $Fe_{85}Ga_{15}$ and $Fe_{83}Ga_{17}$. Clark *et al.* also measured the [100] magnetostriction of single crystal $Fe_{83}Ga_{17}$ under constant compressive stress levels ranging from 15.5 to 96 MPa at room temperature as shown in Figure 1.6b. Fe-Ga alloys attained saturation magnetizations of 1.8 tesla with internal magnetic fields (i.e. applied field minus the material's demagnetization field) of roughly 300 oersted [Clark 2000a, Clark 2000b].

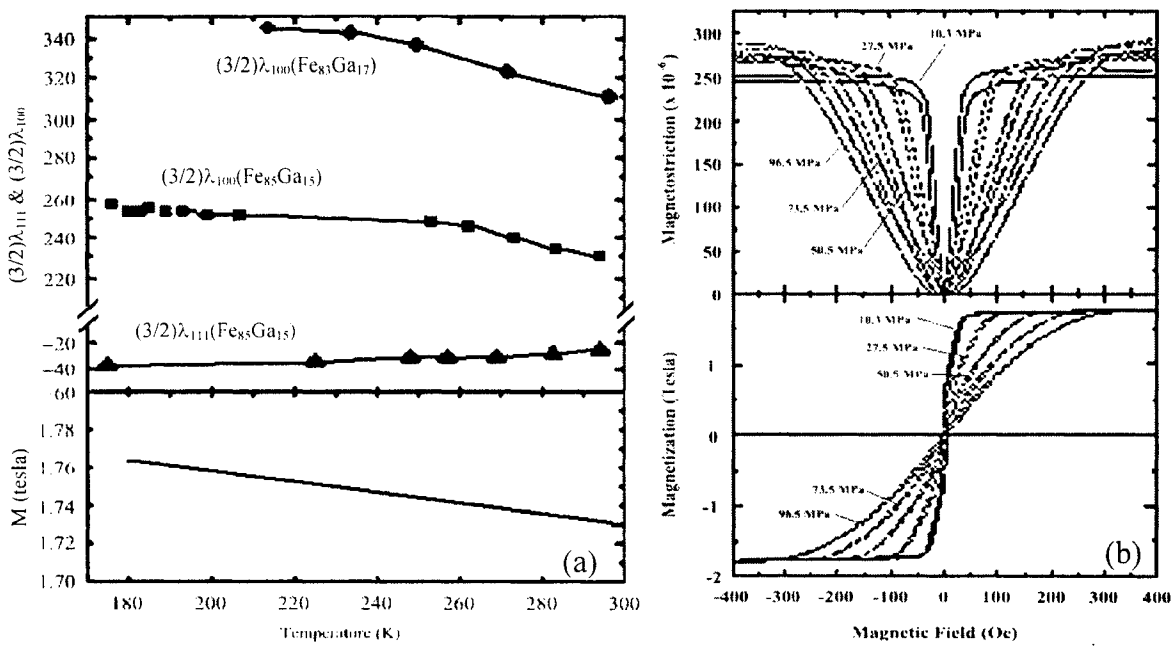

Figure 1.6 a) $(3/2)\lambda_{100}$ and$(3/2)\lambda_{111}$ as a function of temperature for $Fe_{85}Ga_{15}$ at $H = 20$ kOe. Magnetization data for $Fe_{82}Ga_{18}$ was taken from Kawamiya *et al.* [Kawamiya 1972]. b) Room temperature magnetostriction and magnetization of $Fe_{83}Ga_{17}$ as a function of internal magnetic field (H) for various levels of compressive stress. Reprinted with permission of Clark *et al.* from [Clark 2000a].

An understanding of the exact mechanism of magnetostriction in iron and non-magnetic species substituted iron remains incomplete, however research efforts on Al substituted iron have established correlations between temperature, stoichiometry, crystallography and magnetic and mechanical properties [Leamy 1967a, Leamy 1967b, Shull 1976]. This previous work on Al substituted iron and ongoing research with Ga substituted iron has given rise to qualitative theories [Cullen 2001, Lograsso 2003]. Summarizing the existing qualitative theory, Al and Ga are large atoms relative to Fe, however they fit into the α-Fe BCC crystal lattice sites, randomly replacing Fe for substitution concentrations less than 19 at. %. Pairs of the substituting species situated along the edges of the cubic lattice structure tend to facilitate a short-range order, therefore resulting in an anisotropic condition and internal strain. As the material is magnetized, magnetic moment rotation gives rise to a magnetoelastic interaction and anisotropic magnetostriction favoring the <100> directions. It has been shown that if Al or Ga substitution is excessive, i.e. greater than ~17 at. %, a low-energy long-range ordering arises between the substituted atoms. A $D0_3$ or B2 crystallographic structure then results (Figure 1.4) with an accompanying decrease in the magnetic order and a significant reduction in the magnetostrictive effect [Kawamiya 1972, Clark 2001]. Attempting to improve on the ambiguity of this qualitative theory, efforts by Wu *et al.* are focused modeling the magnetostrictive effect at a quantum level from first principles [Wu 2002].

1.3.4 Piezomagnetic relationships

Regardless of the incomplete description of Fe-Ga alloys' exact magnetostrictive mechanism, a simple model using linear piezomagnetic relationships provides insight to the material's coupled magnetic and mechanical (i.e. magnetomechanical) nature. Although the magnetostrictive process is inherently nonlinear, linear approximations of the magnetomechanical processes are useful in describing an axial magnetostrictive response over a limited change in applied magnetic field and/or stress. The linearized one-dimensional piezomagnetic equations at, constant temperature, take into consideration incremental changes in the applied magnetic field ΔH and stress $\Delta\sigma$, which are linearly superimposed to give the incremental changes in strain $\Delta\varepsilon$ and magnetic flux density ΔB as [Calkins 1997]

$$\Delta\varepsilon = \frac{\Delta\sigma}{E_y^H} + d_{33}\Delta H \tag{1.5a}$$

and

$$\Delta B = d_{33}^*\Delta\sigma + \mu^\sigma \Delta H \,. \tag{1.5b}$$

The material properties of Young's Modulus E_y^H and permeability μ^σ represent values pertaining to constant magnetic field H and constant stress σ conditions respectively. The piezomagnetic coefficient d_{33} symbolizes the axial magnetostriction coefficient and represents the change in strain per change in magnetic field at a constant stress. The parameter d_{33}^* represents the change in magnetic induction per change in stress at a constant magnetic field.

Providing a figure of merit for the transduction capability of magnetostrictive materials, the coupling factor k_{cc} may be derived from the piezomagnetic equations [Calkins 1997]. The square of the coupling factor is defined as

$$k_{cc}^2 = \frac{d_{33}d_{33}^* E_Y^H}{\mu^\sigma}, \tag{1.6}$$

where $0 < k_{cc}^2 < 1$. This coupling provides the relationships between the constant field and constant induction elastic modulus

$$E_Y^H = E_Y^B\left(1 - k_{cc}^2\right) \tag{1.7}$$

as well as the constant strain and constant stress permeabilities

$$\mu^\varepsilon = \mu^\sigma\left(1 - k_{cc}^2\right). \tag{1.8}$$

Materials with higher coupling factors possess larger transduction capabilities (i.e. more effective conversion of energy between magnetic and mechanical states). However, high coupling factors also imply low permeabilities, which make them difficult to magnetize (see Equation 1.6). Values of k_{cc} expected in Ga substituted iron may be as high as 0.5 [Clark

2000a]. For comparison, coupling factors in Terfenol-D have been measured as high as 0.7 to 0.8 [Clark 1980]. The coupling factor k_{cc} may be determined experimentally using the mechanical or magnetic relationships of Equations 1.7 and 1.8.

1.4 Polycrystalline material properties and texturing

The texturing, or preferential orientation, of the crystallographic structure in metals has long been used to tailor their physical characteristics. Textured materials such as grain-oriented silicon-iron steels have been developed as magnetically efficient transformer cores. Another common use of texturing is in structural applications where textured sheet metals offer improved formability as well as tailored anisotropic strength and fatigue characteristics.

This research is focused on the development of crystallographic textured iron-substituted alloys to produce materials that achieve highly magnetostrictive, magnetic and favorable structural properties simultaneously. In order to engineer these optimized alloys it is necessary to understand the effect of crystallographic texture, grain size and processing on the material's magnetic and mechanical properties. Because the iron-substituted alloys of interest possess a BCC structure, the focus of this section is to examine the factors affecting the mechanical properties of BCC materials. This section begins with a review of the texturing requirements for optimizing the magnetoelastic properties of gallium-substituted iron alloys. Subsequently, aspects of crystallographic texture-dependent properties including the elastic and plastic response, effect of grain boundaries, fracture mechanics, cyclic strain hardening/softening, fatigue and environmental susceptibility will be examined.

1.4.1 Iron - gallium texturing

The degree of texturing of the iron-gallium alloys having a BCC structure for a stoichiometry near $Fe_{83}Ga_{17}$ is of particular interest. The single crystal magnetostrictive performance is retained, where $(3/2)\lambda_{100} \sim 300$ ppm, while avoiding the potential complications of the ordered $D0_3$ and B2 structures which exhibit reduced magnetostrictive capability. Additionally, for this stoichiometry, maximum magnetostrictive performance is maintained without the need for quenching heat treatments (Section 1.3.3). The resulting magnetomechanical capability of these materials are desirable for transducer and structural

applications where the generation of displacement and force is needed. Although the maximum magnetomechanical performance of Fe-Ga alloys is achieved in a <100> oriented single crystal, the single crystals are costly to produce and their mechanical characteristics such as yield strength are known to be variable due to crystal surface defects.

Given the drawbacks of single crystal material, polycrystalline forms textured by rolling or other methods provide an attractive alternative with the potential for improved mechanical robustness and cost-effective production. The maximum magnetomechanical response of the Fe-Ga alloy is achieved with a cube texture. Representative of the cube texture, a segment of {100}<001> oriented polycrystalline sheet is shown in Figure 1.7. The [100] loading direction anticipated during in-service use is also indicated.

1.4.2 Elastic properties

Metals are typically thought of as having single values for their Young's modulus and Poisson's ratios since they are commonly used in their isotropic (non-textured) polycrystalline forms. However, the elastic properties of single crystal material and highly textured material are generally anisotropic. This anisotropy in elastic characteristics can dramatically affect the performance of engineering materials and even lead to unusual characteristics such as negative Poisson's ratios.

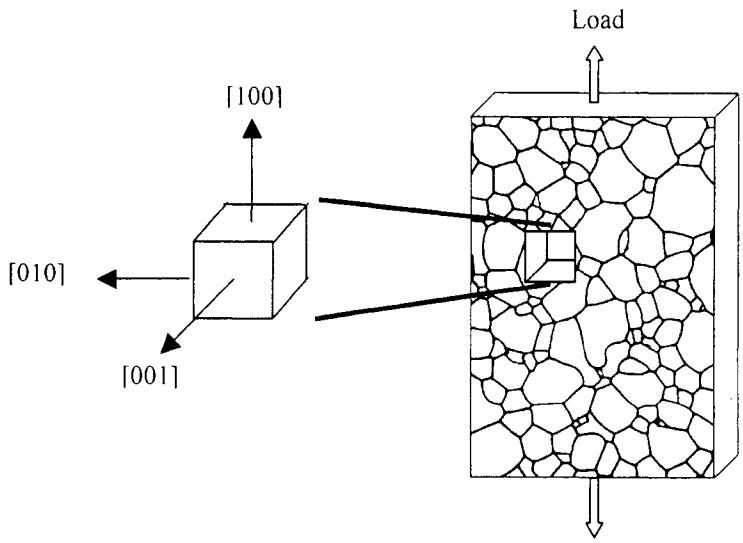

Figure 1.7. The {100}<001> cube sheet structure desired for gallium-substituted iron alloys.

By definition, polycrystalline materials are a bound collection of single crystals as depicted in Figure 1.7. Within the single crystals, the mechanical properties of the BCC crystal lattice are inherently anisotropic due a directional dependence in the atomic packing density (Fig. 1.1b). For example, single crystal iron's lowest Young's modulus has been measured at 131 MPa in the [100] direction, while an intermediate modulus value of 219 MPa occurs in the [110] direction. The maximum elastic modulus value of 283 MPa was found in the [111] direction. [Lyman 1948]. The directional properties of polycrystalline materials, consisting of these anisotropic single crystals, may vary significantly depending on the degree and type of texturing present. For example, wiredrawn iron exhibits a [110] fiber texture in the direction of drawing thus giving intermediate axial elastic modulus values compared to the radial direction. In contrast, sheet products can display near isotropic behaviors, in plane, if the texture reflects alignment of the proper plane parallel to the sheet surface. For example, textured (111) polycrystalline sheet steels exhibit the highest in plane stiffness possible as no soft <100> crystal directions lie in plane [Titerov 1998].

The mathematic relationships for the anisotropic elastic properties of BCC materials will be developed further in section 1.5 to provide a foundation for modeling the Fe-Ga alloys' stress-strain response induced by saturation-magnetostriction generated strains. Modeling and analysis of a material's bulk magnetostrictive response, utilizing these relationships, are presented in Chapter 5. The elastic relationships governing the expression of a material's auxetic (negative Poisson's ratio) behaviors will also be inspected.

Aside from influencing the overall external material behavior, the effect of elastic anisotropy is an important factor governing the material's internal behavior. Depending on the degree of texturing, the individual grains within a polycrystalline material may occupy a range of orientations with neighboring grains experiencing different degrees of interaction. Consequently, the loading of a polycrystalline body results in stress and strain variations within and between crystals. These stress and strain variations are important factors when considering the plastic behavior, failure modes and environmental susceptibility of textured polycrystalline materials.

1.4.3 Plastic properties

When engineering a material, one must consider how the crystal morphology will affect the plastic response to loading. The plastic deformation of a metal coincides with the formation and movement of dislocations, which consist of atomic irregularities in the crystal lattice structure. Two basic dislocation types include the edge and screw dislocations. An extra half plane of atoms in the crystal lattice characterizes the edge dislocation, while an atomic misalignment similar to a step along the edge of a cube distinguishes a screw dislocation [Honeycombe 1968]. The movement of these dislocations is in turn affected by anisotropic material properties as well as crystallographic imperfections including grain boundaries, vacancies and interstitial atoms. Throughout the process of plastic deformation, dislocations grow and move as a result of applied stresses exceeding the yield strength of the material. Some members of the family of BCC metals are considered to be "hard" where a yield stress greater than 10 MPa are required to generate yield in single crystals [McLean 1962]. Controlling the extent of plastic deformation, the fractional strength of the polycrystal compared to a perfect single crystal depends on crystal size, arrangement and imperfections. The particular mechanisms of plastic deformation in BCC metals are now considered.

Dislocations exist in networks within the grains where they tend to form threefold nodes in BCC metals with angles of 96° in three dimensional space. Providing an avenue for plastic deformation through the disruption of these dislocation networks, BCC metals exhibit eight different slip Burgers vectors (or distinct dislocation morphologies). There are several modes of common dislocation dynamics associated with these systems. "Slip" occurs when an applied stress drives a dislocation to move along a plane through the crystal lattice. This results in the material above the plane shifting location relative to the material below the plane. "Cross slip" occurs when dislocation motion transfers from one plane to an intersecting plane. Common slip systems favored in the BCC metals are in the [111] direction on (110) planes and in multiple directions on the (112) and (123) planes. The highest ductility in BCC metal is typically developed with the easy slip plane oriented at 45° to the stress direction [Prasad 1994]. As an example of anisotropic plastic deformation, the slip mechanisms in high purity (99.96%) α-Fe are considered. At room temperature the primary slip system is {110}<111> with slip occurring at a critical resolved shear stress

(τ_{CRSS}) of 27.5 MPa [Dieter 1988]. The {110} set of planes is favored for slip as they are the planes of highest planar atomic packing density, thus presenting the lowest energy barrier to dislocation movement. Similarly the <111> family of slip directions are favored as they possess the highest linear atomic packing density within the {110} planes. Secondary slip occurs in pure α-Fe on the {211}<111> and {321}<111> since these planes have lower relative atomic packing densities and require the addition of more energy to trigger dislocation movement.

Figure 1.8 depicts a plot of shear stress vs. elongation for two BCC α-Fe single crystals having differing orientations. The crystal orientation of trace 1 initially underwent strain softening, before developing modest strain hardening through simple slip mechanisms. The crystal orientation of trace 2 produced immediate and rapid strain hardening with increasing elongation through the interaction of multiple slip systems (i.e. complex slip). In both cases, the regions of positive slope indicate the presence of strain hardening due to dislocation interactions and a reduction in dislocation mobility. Although not observed for these crystal orientations, a nearly horizontal stress-strain curve would indicate easy glide generated by a single slip system [McLean 1962].

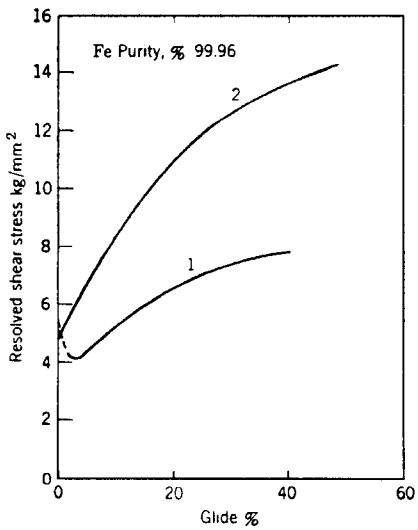

Figure 1.8. Shear stress versus strain curves of BCC meta α-Fe single crystals collected at room temperature. Crystallographic orientations generating: 1) simple slip with modest strain hardening; 2) complex slip with rapid strain hardening, [after McLean 1962].

Since polycrystalline material possesses a range of crystallographic orientations, for a given stress a broader range of energy is required to activate dislocations and overcome the stable atomic configuration than in a single crystal. Consequently, polycrystals have been observed to slip less suddenly than single crystals. It has been observed that the intersection of dislocations and the planes of easy slip result in an impediment to dislocation motion thus reducing ductility. Processing conditions of a metal such as cold working and annealing have a large impact on the dislocation density and structure. Rough estimates of the dislocation concentrations for general metals are listed in Table 1. Cold working and annealing have opposite effects where the annealed materials have a lower dislocation concentration. Consequently, annealed materials inherently have a larger potential to be deformed plastically while retaining ductility. When determining material processing schedules for texturing purposes it is important to note that changes in annealing temperature have a larger impact on dislocation network size and concentration than grain size. Activated by thermal energy, the crystal lattice becomes more regular as dislocations begin "annealing out" at ½ $T_{melting}$ in kelvin [McLean 1962]. Consequently, attempts to increase grain size through recrystallization will wipe out any previous dislocation structure. Having the opposite effect of annealing, dislocation mobility may be tied-up by the point defects. These point defects include vacancies and interstitial sites, which are generally produced by cold working.

Material condition	Dislocation concentration/ cm^2
Carefully grown, annealed, pure single crystal	$0 - 10^3$
Typical annealed single crystal	$10^5 - 10^6$
Annealed polycrystalline	$10^7 - 10^8$
Heavily cold worked polycrystalline	$10^{11} - 10^{12}$

Table 1. Typical dislocation concentrations of BCC metals for varying degrees of processing [McLean 1962].

1.4.4 Grain boundaries

With the goal of producing textured iron-substituted alloys possessing optimized mechanical properties in addition to the desired magnetic properties, one must consider the effect of grain boundaries. Grain boundaries have long been known to significantly influence material characteristics such as yield strength, ductility and crack propagation through their effect on dislocation movement.

Grain boundaries are defined as an atomic misfit, over a distance two to three atoms wide, which separate grains or localized areas of homogeneous crystallographic orientation. The size and geometry of grain boundaries are governed by the minimization of energy, hence satisfying surface tension and space filling rules. Grain boundaries raise the overall energy of the material and act as preferred sites for the absorption and emission of defects. During the process of annealing, in which thermal energy promotes atomic rearrangement and the elimination of grain boundaries, precipitates and solutes may impede grain boundary migration. Precipitates and solutes are often used to control a metal's crystallography and modify the material properties through the control of grain sizes.

In addition to grain boundaries, a more subtle but similar crystallographic structure exists. Sub-boundaries within individual grains are commonly observed where the crystal lattice exhibits misorientations up to 1°. Unlike grain boundaries, the sub-grain boundaries are thought to have little influence on the material's mechanical properties.

Grain boundaries affect a material's mechanical properties in several ways. One-way is due to the change in crystallographic direction from grain to grain, which causes slip planes to become discontinuous across the grain boundary. As a result, dislocations are tied up at the boundaries thus requiring the activation of several slip systems to move. This increase in activation energy is one source of strain hardening under cyclic loading conditions.

A second effect on material properties is developed through grain boundaries' ability to impede the mobility of dislocations. By this action, an increase in the quantity of grain boundaries per unit volume of material (through decreasing grain size) will increase the yield stress. Observations of many metals have shown good correlations where yield stress, ductility and hardness are proportional to $(\text{grain size})^{-1/2}$. (These empirical relationships

eventually do fail however for exceedingly fine grain sizes.) To quantify the yield stress correlation, a flow-stress relationship has been developed which assumes that all grains are the same size and shape and that the grain boundaries have the same properties. The flow-stress equation is listed in Equation 1.9 where σ is the flow-stress at a given plastic strain, σ_o is a constant for the flow-stress of a grain in tension, K is a constant representing the flow coupling effect of the boundary and d is the mean grain diameter [Kurzyalowski 1996].

$$\sigma = \sigma_o + \frac{K}{d^{1/2}} \tag{1.9}$$

Another grain boundary effect is that at higher temperatures grain boundaries provide a shear system resulting in voids and creep. Finally, grain boundaries may provide a path for crack propagation if intergranular adhesion is poor.

Grain boundaries and grain size have many implications for the material designer. Although finer grain sizes improve mechanical characteristics such as yield strength, they may also be detrimental from a magnetic perspective. Grain boundaries tend to impede magnetic domain wall motion, leading to larger energy losses in changing magnetic fields. Material texturing techniques will have to strike the proper balance between the desired mechanical and magnetic properties through the control of grain size and their boundaries.

1.4.5 Fracture

The highest true breaking strengths of metals rarely exceed $E/5$ to $E/10$, where E is the material's elastic modulus. Theoretically, a maximum strength of $E/2$ is achievable. However, due to structural heterogeneity, failure does not begin everywhere simultaneously. There are five common types of failure processes: ductile, brittle, adiabatic shear, creep, and fatigue fracture. Of these, ductile and brittle fracture processes will be examined for their relevance to the design of textured materials. The high temperature phenomena of creep and high-speed effect of adiabatic shear are considered to be beyond the scope of interest at this time. Fatigue will be discussed in a later section.

Ductile failures under tensile stress (experimentally observed as a cup and cone morphology) are conveniently divided into three stages. In stage one, the specimen necks

down and cavities form around point imperfections. As necking continues in stage two, the cavities join to form a larger cavity that spreads transversely through the specimen. In the third stage, the cavity develops into a crack propagating at 45°outward to the surface. The influence of material structure on ductile fracture is manifested in two ways. First, a strong relationship has been demonstrated where the fracture stress is proportional to (grain size)$^{-1/2}$. This is known as the Hall-Petch relationship and has the same form as the previously discussed relationship of yield stress to grain size [Jimenez 1995]. Second, crystallographic texture causes anisotropy in the observed fracture strengths. Typically, BCC materials are more ductile in the cast and or working direction. This is most likely due to availability of active slip planes accommodating induced shear stress.

Brittle fracture occurs when crack propagation proceeds in the absence of plastic deformation. The fracture travels along a cleavage plane within the grains and/or along grain boundaries. A tough/brittle transition temperature T_o may be observed where brittle fracture occurs below T_o and ductile fracture occurs above T_o. Below T_o, the yield stress exceeds the fracture stress. For reference, $T_o \cong$ -200°C for mild steel. The stress required to propagate the fracture path depends on the cohesive strength of the atoms. The lower the required stress is for fracture, the lower the amount of plastic work or deformation that can be done before failure occurs. The controlling factor is the energy of the two new surfaces after fracture. Depending on their chemical nature, the presence of solutes can either impede or promote brittle crack propagation along grain boundaries. The presence of oxygen in iron (as little as 0.01%) has been shown to raise T_o by 200°C thus changing the fracture path from a transcrystalline (100) failure to an intergranular failure [McLean 1964]. The method of heat treatment and cooling rate is an important factor in controlling the solute concentration along grain boundaries. Slow cooling generally allows time for compositional segregation. Thus, water quenching tends to lower the tough/brittle transition temperature. Increasing grain size also has the same effect as operating at lower temperature, thus decreasing the fracture stress relative to the yield stress. Crack propagation across a grain boundary is generally impeded since cleavage planes across the boundary usually do not coincide. To continue propagation of the cleavage plane, the crack must propagate intergranularly until it initiates the crack in the adjoining crystal. Lastly, strain rate is an important factor in determining the type

fracture. Sufficiently high strain rates may exceed the flow rate of the material thus favoring brittle failure over deformation. For example, notched specimens behave in an increasingly brittle manner with higher strain rates developed at the notch root.

By taking advantage of the proper working direction, cube textured Fe-Ga alloys should exhibit superior ductility in the expected direction of loading, i.e. on the [100] direction. Given the fracture-stress relationship to grain size, texturing efforts should also strive for the smallest grain size possible. To suppress intergranular brittle failures, solutionizing heat treatments and quenching must be considered, particularly for Ga substitution >17 at. %, to limit the formation of grain boundary precipitates. Finally, oxygen contamination during texturing processes should be avoided to suppress intergranular brittle failures.

1.4.6 Cyclic strain hardening/softening and fatigue

Textured iron-gallium alloys may find use in transducer or structural systems where cyclical stress overloads resulting in plastic strains occur. Therefore, an examination of cyclic strain hardening/softening processes leading to fatigue in BCC metals is necessary for the appropriate design and application of these materials.

Whether a metal will undergo cyclic strain hardening or softening when first subjected to cyclic plastic deformation generally depends on the material's processing history. Cold worked and solute or precipitate hardened materials cyclic soften while as-annealed materials cyclic harden. An empirical relationship describing strain hardening/softening is the power law relationship of Equation 1.10 where stress amplitude σ_a is a function of the plastic strain amplitude ε_a, the cyclic strength coefficient k, and the cyclic strain hardening exponent n [Bily 1993]. This relationship has been observed for metals in general. However, with an adequate database, this relationship may be used to determine how quickly a specific textured BCC material strain hardens/softens, thus ultimately leading to fatigue life predictions.

$$\sigma_a = k(\varepsilon_a)^n \tag{1.10}$$

Examining the details of strain hardening/softening at a microscopic level offers some insights to the mechanisms that will be active in textured BCC metals. According to microscopic theory of plastic deformation, the flow stress at any point on the stress-strain hysteresis loop (in the region of plastic deformation) represents impediments to dislocation movement. To a first approximation, in BCC metals this is described by Equation 1.11 where the externally applied stress $\sigma_{applied}$ is in equilibrium with the sum of internal stresses. These internal stresses include short-range stress $\sigma_{short\text{-}range}$ due to point defects and long-range stress $\sigma_{long\text{-}range}$ due to a pile up of dislocations.

$$\sigma_{applied} = \sigma_{short-range} + \sigma_{long-range} \tag{1.11}$$

The short-range stresses are known to be strongly dependent on temperature and strain rate while long-range stresses are related to dislocation density and configuration. In BCC metals, the temperature dependence of short-range stress is due to the activation of screw dislocations. Above the transition temperature T_o, typically $(0.1 - 0.2)T_{melt}$ (in kelvin), screw dislocations move as easily as edge dislocations. For pure iron, measurements have shown that T_o = room temperature for strain rates of 10^{-5} 1/sec. For comparison, typical fatigue processes occur at strain rates of 10^{-3} to 10^{-2} 1/sec. Consequently, strain hardening/softening and ultimately the fatigue response of iron-substituted alloys will likely be governed by low temperature processes involving edge dislocations [Bily 1993].

Gauging the scale of the temperature dependent microscopic processes just described, strain hardening has been described as weak in BCC metals. The three factors attributed to a weak strain hardening response are the ease of cross slip, weakness of attractive junctions and the occurrence of pencil glide (slip occurring in the [111] direction on numerous planes) [Bily 1993].

Despite the "weak" effect of strain hardening in BCC metals, consideration of grain size is also warranted. It has been shown that plastic anisotropy dominates the strain hardening process due to grain boundary interruption of slip for up to several percent of elongation. Thereafter, the rate of strain hardening is the same in single and polycrystals [McLean 1964]. In other words, fine-grained materials strain harden faster than their large-grain counterparts if the elongation is not excessive.

Following strain hardening/softening, cyclic loading of sufficient amplitude and/or duration promotes fatigue damage and ultimately fatigue failure. Cyclic plastic deformation is the primary cause for the accumulation of damage during cyclic loading. Plastic deformation of the material volume can cause changes in the material properties while localized plastic deformation may lead to microcracks developing at nucleation sites. The three stages of the fatigue process include:

1. Strain hardening/softening occurring due to interaction of dislocations.
2. Nucleation of fatigue cracks in localized zones of plastic slip (persistent slip bands).
3. Propagation of fatigue cracks into high stress region of localized zones of plastic deformation.

Having examined the processes facilitating fatigue, it is obvious that the fatigue properties of metals are significantly influenced by their microstructure. With the goal of designing fatigue resistant textured BCC materials, several additional effects of grain structure should be considered. Fine grains provide better fatigue resistance through reduction of strain along slip bands thus decreasing the irreversible slip that leads to damage accumulation. Furthermore, fine grains provide more grain boundaries thus assisting in transcrystalline crack arrest. Finally, anisotropy developed through cold working improves fatigue resistance for loading conditions in the direction of working due to elongated grain structure in the direction of loading [Stephens 2001].

1.4.7 Environmental susceptibility

Another factor to be considered in the design of textured BCC metals is their susceptibility to environmental effects. In particular, brittle failure and fatigue properties can be heavily dependent on surface effects such as corrosion. Corrosion is known to facilitate brittle failure at lower stress levels and shorten fatigue life. Randomly oriented grains in polycrystalline materials tend to perpetuate these effects due to the individual grains' anisotropic properties. The grains' varying orientations lead to stress concentration at the grain boundaries thus hastening crack formation and the penetration of corrosion. In contrast, the low-angle grain boundaries of a highly textured material may reduce these stress

concentrations and tend to resist corrosion. Also affecting a material's corrosion resistance, oxide formation has been shown to be dependent on the crystal orientation at the surface. Although composition sensitive, the rate of growth of iron oxides has been found to be lowest on (110) iron alloy sheet surfaces. The oxide film that does form is tightly bound, thus reducing metal loss due to further oxidation [Titerov 1998].

1.4.8 Material texturing summary

Considering the general trends in strength, fatigue and corrosion resistance of general BCC metals, the prospects for achieving acceptable mechanical properties in heavily textured iron-substituted alloys are good. The goal will be to produce fine-grained polycrystalline structure free of defects and impurities in order to promote higher yield strengths and crack propagation resistance. Although anisotropy of the desired {100}<100> cube texture will result in a soft material in the loading direction, the use of low-angle grain boundaries and elongated crystals in the direction of loading will promote ductility and resistance to low cycle fatigue failure. Additional benefits of a highly textured material containing low-angle grain boundaries will be resistance to the penetration of surface corrosion.

1.5 Cubic crystal elasticity relationships

The elastic anisotropy of the BCC crystal lattice may be associated with the directional dependence in the atomic packing density (Figure 1.1b), which is ultimately attributed to the crystal lattice existing in its lowest energy configuration. Anisotropic elastic properties are used to describe the material's stress-strain relationships relative to its crystallographic axes (i.e. the material coordinate system). The following section reviews the elasticity relationships for cubic systems and the rotational coordinate transformation method that allows the bulk elastic properties in the global coordinate system to be described in terms of material stiffness constants [Mason 1958]. These transformation methods will allow quantities such as Young's modulus and Poisson's ratios to be described in terms of the material elastic constants and visa versa.

1.5.1 Stress-strain transformations

Analysis of a material's anisotropic elastic properties is facilitated using the generalized Hook's law (Equation 1.12). In the case of cubic crystals, symmetry permits the relationships between stress σ_i and strain e_j to be completely defined using the three second-order engineering elastic constants c_{11}, c_{12} and c_{44} [Nye 1985].

$$\sigma_i = c_{ij} e_j \tag{1.12}$$

where $i = 1, 2, \ldots 6; j = 1, 2, \ldots 6,$ and $c_{11} = c_{22} = c_{33}$; $c_{12} = c_{21} = c_{13} = c_{31} = c_{32} = c_{23}$; $c_{44} = c_{55} = c_{66}$. All other $c_{ij} = 0$.

This engineering stress-strain relationship may be expanded for the material coordinate system as:

$$\begin{bmatrix} \sigma_{11} \\ \sigma_{22} \\ \sigma_{33} \\ \tau_{23} \\ \tau_{13} \\ \tau_{12} \end{bmatrix} = \begin{bmatrix} c_{11} & c_{12} & c_{12} & & & \\ c_{12} & c_{11} & c_{12} & & & \\ c_{12} & c_{12} & c_{11} & & & \\ & & & c_{44} & & \\ & & & & c_{44} & \\ & & & & & c_{44} \end{bmatrix} \begin{bmatrix} \varepsilon_{11} \\ \varepsilon_{22} \\ \varepsilon_{33} \\ \gamma_{23} \\ \gamma_{13} \\ \gamma_{12} \end{bmatrix}$$

where the engineering shear stress and engineering shear strain are represented respectively by τ and γ. Principle stress and strains are equivalent for the tensor and engineering representation thus the usual σ and ε notation are used.

The numbered subscripts for the stress and strain variables indicate the material coordinate system. The first subscript represents the material face upon which the stress is applied and the second subscript represents the direction in which the applied stress acts. Figure 1.9 depicts the stress and strain components in a loaded body for the material coordinate system.

Rotational coordinate transformation of the material stress-strain relationship will allow the global elastic response to be determined for arbitrary grain orientations. To accomplish this, tensor notation is used. The tensor representation of Hooke's law (Equation 1.12) is given in Equation 1.13 where the conversion of engineering shear strains to tensor shear strains requires that $\varepsilon_{23} = \gamma_{23}/2$, $\varepsilon_{13} = \gamma_{13}/2$, and $\varepsilon_{12} = \gamma_{12}/2$. A compensating factor of 2 has been applied to the corresponding terms of the stiffness matrix.

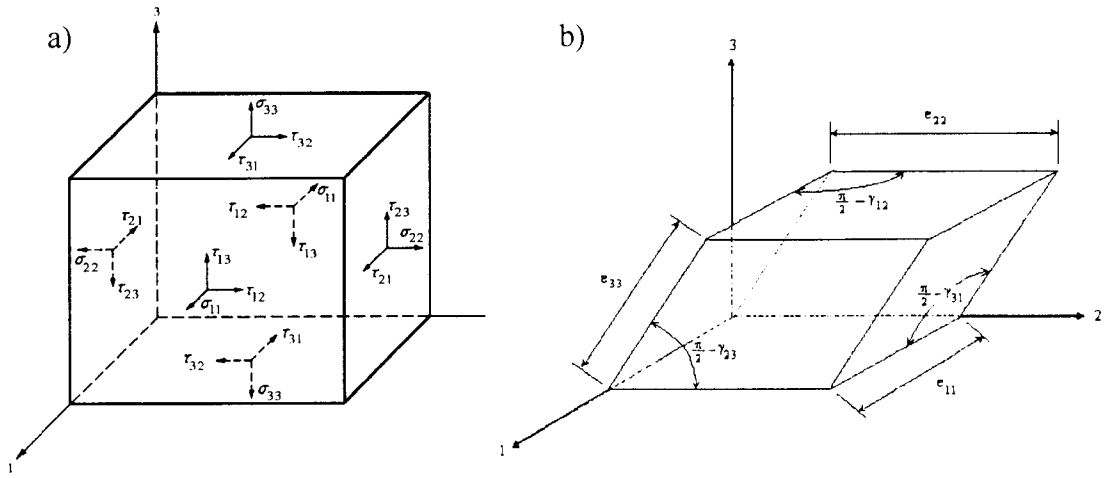

Figure 1.9 A point in a loaded body as represented in the material coordinate system for a) stress components, b) strain components.

$$\begin{bmatrix} \sigma_{11} \\ \sigma_{22} \\ \sigma_{33} \\ \tau_{23} \\ \tau_{13} \\ \tau_{12} \end{bmatrix} = \begin{bmatrix} c_{11} & c_{12} & c_{12} & & & \\ c_{12} & c_{11} & c_{12} & & & \\ c_{12} & c_{12} & c_{11} & & & \\ & & & 2c_{44} & & \\ & & & & 2c_{44} & \\ & & & & & 2c_{44} \end{bmatrix} \begin{bmatrix} \varepsilon_{11} \\ \varepsilon_{22} \\ \varepsilon_{33} \\ \varepsilon_{23} \\ \varepsilon_{13} \\ \varepsilon_{12} \end{bmatrix} \tag{1.13}$$

Short hand notation for the this tensor stress-strain relationship is :

$$[\sigma'] = [C_t][\varepsilon']$$

where the primed notation indicates the material coordinate system and $[C_t]$ is the tensor form of the stiffness matrix.

To arrive at the rotational coordinate transformation relationship for stress and strain, the rotational coordinate transformation tensor [Q] is specified for a transformation from the global to material system as shown in Figure 1.10. Coordinates transform as [e'] = [Q][e] going from the global to the material (primed) coordinate system. Orthogonal vectors **x**, **y** and **z** define the global coordinate system and vectors **1**, **2** and **3** define the material coordinate system. The direction cosines α_x, α_y and α_z define the material vector **1** in the global system. Likewise, β_x, β_y and β_z and η_x, η_y and η_z define the material vectors **2** and **3** orientations respectively.

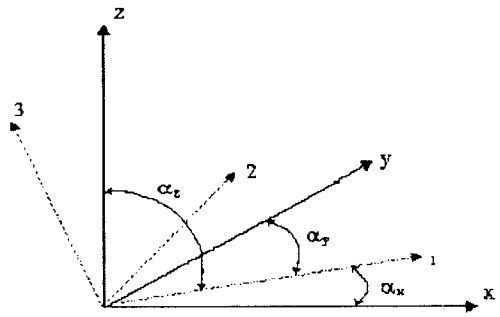

$$Q = \begin{bmatrix} \alpha_x & \alpha_y & \alpha_z \\ \beta_x & \beta_y & \beta_z \\ \eta_x & \eta_y & \eta_z \end{bmatrix}$$

Figure 1.10 Direction cosines for a rotational coordinate transformation from the global coordinate system (x,y,z) to the material coordinate system (1,2,3).

The second rank tensors of stress and strain may be transformed between the global and material coordinate system using transformation relationship [T]. The elements of [T] are obtained from the transformation tensor [Q]. Advanced texts on mechanics of materials have derived the transformation relationship [T] as [Boresi 1993]:

$$[T] = \begin{bmatrix} \alpha_x^2 & \alpha_y^2 & \alpha_z^2 & 2\alpha_y\alpha_z & 2\alpha_x\alpha_z & 2\alpha_x\alpha_y \\ \beta_x^2 & \beta_y^2 & \beta_z^2 & 2\beta_y\beta_z & 2\beta_x\beta_z & 2\beta_x\beta_y \\ \eta_x^2 & \eta_y^2 & \eta_z^2 & 2\eta_y\eta_z & 2\eta_x\eta_z & 2\eta_x\eta_y \\ \beta_x\eta_x & \beta_y\eta_y & \beta_z\eta_z & (\beta_y\eta_z + \eta_y\beta_z) & (\beta_x\eta_z + \eta_x\beta_z) & (\beta_x\eta_y + \eta_x\beta_y) \\ \alpha_x\eta_x & \alpha_y\eta_y & \alpha_z\eta_z & (\alpha_y\eta_z + \eta_y\alpha_z) & (\alpha_x\eta_z + \eta_x\alpha_z) & (\alpha_x\eta_y + \eta_x\alpha_y) \\ \alpha_x\beta_x & \alpha_y\beta_y & \alpha_z\beta_z & (\alpha_y\beta_z + \beta_y\alpha_z) & (\alpha_x\beta_z + \beta_x\alpha_z) & (\alpha_x\beta_y + \beta_x\alpha_y) \end{bmatrix} \quad (1.14)$$

Example uses of the transformation process include the conversion of stresses applied in the global coordinate system to equivalent stresses in the material coordinate system and the conversion of strains in the material coordinate system to strains in the global coordinate system. These respective stress and strain transformations are given as:

$[\sigma'] = [T][\sigma]$ and $[\varepsilon] = [T]^{-1}[\varepsilon']$ where $[T]^{-1}$ represents the inverse of [T].

The strain in the global coordinate system [ε] may now be determined from global stresses [σ] provided the crystallographic orientation of the material is known relative to the global reference system. Application of Eq. 1.12, 1.13 and 1.14 give:

$$[\varepsilon] = [T]^{-1}[\varepsilon'] = [T]^{-1}[C_t]^{-1}[\sigma'] = [T]^{-1}[C_t]^{-1}[T]\,[\sigma] \tag{1.15}$$

Rearrangement of Eq. 1.15 gives the global stress generated by global strains as $[\sigma] = [D_t]\,[\varepsilon]$ where the equivalent tensor stiffness matrix is:

$$[D_t] = [T]^{-1}[C_t]^{-1}[T] \tag{1.16}$$

1.5.2 Elastic characteristics from material properties

The elastic characteristics such as Young's modulus and Poisson's ratio of a specimen and their measurement are dependent on material properties and the material orientation relative to the observation (global) coordinate system. Utilizing the elasticity and transformation relationships of the previous section, elastic properties such as Young's modulus and Poisson's ratio may be stated in terms of c_{ij} for any direction [Mason 1958]. The Young's modulus $E_{[uvw]}$ is defined as the ratio of stress to strain for which a collinear stress application and strain measurement occur in the *[uvw]* direction. The Poisson's ratio $\nu_{[uvw]}$ is defined as the negative ratio of transverse strain to longitudinal strain that results from loading in the longitudinal direction where the *[uvw]* subscript indicates the direction of the transverse strain measurement.

For uniaxial loading conditions found in typical tensile test configurations, the anisotropy of a cubic material's elastic properties may be emphasized by using two high-symmetry crystal orientations and loading directions that generate minimum or maximum crystal lattice shear stress conditions. The effects of c_{11} and c_{12} may be expressed independently from c_{44} through uniaxial [100] loading of a (001)[100] single crystal. With this loading condition the directionally dependent relationships for E and ν arise as given in Equations 1.17 and 1.18 [Jain 1990].

Young's modulus: $$E_{[100]} = \frac{c_{11}R}{c_{11}+c_{12}} \tag{1.17}$$

Poisson's ratios: $$\nu_{[010]} = \nu_{[001]} = \frac{c_{12}}{c_{11}+c_{12}}, \tag{1.18}$$

where $$R = \frac{1}{c_{11}}(c_{11}-c_{12})(c_{11}+2c_{12}).$$

The effect of c_{44} on the elastic response becomes highly evident for the uniaxial [110] loading of a (001)[110] single crystal. If the values of c_{11} and c_{12} are known, c_{44} may be easily related to the directionally dependent values of E and ν given in Eqs. 1.19, 1.20, and 1.21 where R is the same as used above [Jain 1990].

Young's modulus: $$E_{[110]} = \frac{4c_{44}R}{R+2c_{44}} \tag{1.19}$$

The first Poisson's ratio: $$\nu_{[1\bar{1}0]} = \frac{R-2c_{44}}{R+2c_{44}}, \tag{1.20}$$

The second Poisson's ratio: $$\nu_{[001]} = \frac{4c_{12}c_{44}}{c_{11}(R+2c_{44})}, \tag{1.21}$$

Depending on the values of c_{11}, c_{12} and c_{44}, the Poisson's ratios $\nu_{[1\bar{1}0]}$ and $\nu_{[001]}$ may be dramatically different. Remarkably, many BCC and FCC systems exhibit negative values of $\nu_{[1\bar{1}0]}$ while $\nu_{[001]}$ is always positive [Jain 1990, Milstein 1979]. The negative Poisson's ratio described here is a two-dimensional effect as shown in the schematic of Figure 1.11 for an [110] axially loaded single crystal. When $\nu_{[1\bar{1}0]}$ is negative, as a consequence of approximate volume conservation, $\nu_{[001]}$ is correspondingly large and positive in the third dimension.

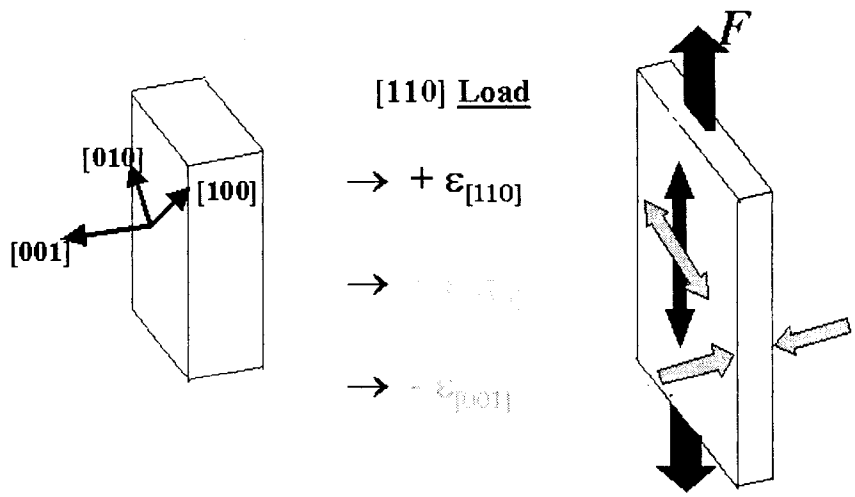

Figure 1.11 Schematic of in-plane negative Poisson's ratio response for a [110] axially loaded single crystal.

Negative Poisson's ratio materials are known to possess "auxetic" behavior (from the Greek term auxetik "increasing" [Random House 1980]) and for the case of the in-plane negative Poisson's ratio described by Eq. 1.20, the phenomena is termed "in-plane auxetic" behavior. Jain *et al.* has shown that the anisotropy parameter "*A*" (Eq. 1.22) is a convenient measure of a material's propensity for exhibiting in-plane auxetic behavior [Jain 1990].

$$A = \frac{2c_{44}}{c_{11} - c_{12}} \tag{1.22}$$

Metallic crystals generally have values of $A > 1$. It has been shown that $\nu_{[1\bar{1}0]}$ must be positive for $A < 2$, that $\nu_{[1\bar{1}0]}$ may be positive or negative when $2 < A < 3$, and that $\nu_{[1\bar{1}0]}$ must be negative if $A > 3$. In the limit of $c_{11} - c_{12} = 0$, A approaches infinity and $\nu_{[1\bar{1}0]}$ approaches its minimum value of -1.0 [Jain 1990]. These relationships are summarized in Table 1.2.

A	$\nu_{[1\bar{1}0]}$	in-plane auxetic
$A < 2$	> 0	No
$2 < A < 3$	> 0 or < 0	no/yes
$3 < A$	< 0	yes

Table 1.2 Permissible Poisson's ratios for metallic crystals on the (001) plane in the $[1\,\bar{1}\,0]$ direction as a function of elastic anisotropy A.

To provide a point of reference, the elastic constants of high purity α-Fe are c_{11} = 228 GPa, c_{12} = 132, c_{44} = 116.5 [Mclean 1972]. These values give the directionally dependent Young's moduli of $E_{[100]}$ = 131 and $E_{[110]}$ = 219 GPa. The Poisson's ratios associated with these moduli are also anisotropic where [100] loading gives $\nu_{[010]} = \nu_{[001]} = 0.37$ and [110] loading gives $\nu_{[1\bar{1}0]}$ = -0.06 and $\nu_{[001]} = 0.61$. Pure α-Fe exhibits a slight in-plane auxetic behavior which is consistent with the anisotropy parameter A = 2.4. A complete summary of Fe and Fe-Ga alloys elastic properties are provide in Table 4.5.

The in-plane auxetic behavior of Fe-Ga alloys are later quantified in the experimental work presented in Chapter 4 and potential applications utilizing the phenomena are explored in Chapter 6.

2. MATERIAL PROCESSING, TEXTURING AND PERFORMANCE

The objective of metallurgical processing of the Fe-Ga alloys is to produce a disordered solid solution of Ga in α-Fe accompanied by a high degree of preferred crystallographic orientation or "texture". Single crystal specimens exemplify perfect texture and were produced to possess the maximum elastic anisotropy and magnetostrictive potential for their stoichiometries. These single crystal specimens are used to establish a baseline for the alloy's mechanical and magnetostrictive and characteristics. Although the procedure used in the manufacture of single-crystals is well established, the best methods for producing textured polycrystalline Fe-Ga alloys are unknown and are the focus of investigation in this research. Polycrystalline texturing methods undertaken in this work include directional crystal growth, deformation texturing and powder metallurgy methods.

The saturation magnetostriction properties of single crystal and textured polycrystalline material may be determined with directionally applied magnetic fields using disk shaped specimens and with coaxially applied compressive stress and magnetic fields using rod shaped specimens. The testing method for disk samples is presented next as it is used to characterize many of the specimens. Thereafter, the corresponding production methods and saturation magnetostriction properties of single and textured polycrystalline specimens are reported. Saturation magnetostriction testing methods for rod-shaped specimens reported in this chapter utilize a thermally controlled transducer. This test method is elaborated upon in Chapter 3 in conjunction with a description of the non-saturation magnetization and magnetostriction characteristics of the rod-shaped specimens.

2.1 Saturation magnetostriction testing

The magnetostrictive properties of a specimen may be measured using a directionally applied magnetic field. If the applied field is strong enough, the specimen becomes magnetically saturated to form a single domain with the vector of M_s aligned in the applied magnetic field direction. Accompanying the change from a demagnetized state to one of magnetization saturation, the specimen experiences a net magnetostriction equivalent to the saturation magnetostriction λ_s. The values of $\lambda_{\parallel}$ and $\lambda_{\perp}$ represent the respective occurrence of

λ_s with the applied magnetic field oriented parallel and perpendicular to the material direction of interest. The schematic in Figure 2.1 depicts the face view of a strain gaged disk-shaped specimen with rotation orientations differing by 0° and 90° relative to a saturating magnetic field *H*. The depiction of the field-induced change in specimen geometry from round (dotted outline) is exaggerated for a strain response dominated by a positive magnetostriction constant.

From the saturation magnetostriction relationship of Equation 1.4 and with disk rotation orientations defined by the angle θ, it can be shown that λ_s varies as a function of $\cos^2(\theta)$. Additionally, the net saturation magnetostriction $\lambda_{\|\text{-}\perp}$ gives the specimen's maximum magnetostriction capability for the chosen direction of strain measurement. Appropriate to the determination of single crystal magnetostriction constants, if the strain gage orientation of a specimen is aligned with the [100] material direction, then $\lambda_{\|\text{-}\perp} = (3/2)\lambda_{100}$. Similarly, if the strain gage is aligned with the specimen's [111] material axis then $\lambda_{\|\text{-}\perp} = (3/2)\lambda_{111}$. To determine the magnetostrictive capability of textured polycrystalline specimens, where the direction and degree of texturing may be unknown, strain gage rosettes are appropriate for determining magnetostriction induced principle strains and ultimately the direction of maximum $\lambda_{\|\text{-}\perp}$.

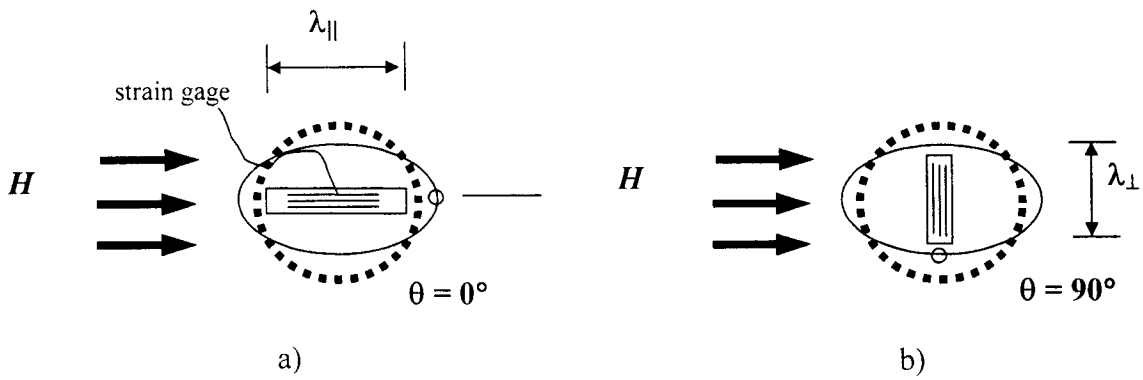

Figure 2.1 Schematic of saturation magnetostriction testing of a disk sample for orthogonal rotation orientations: a) Specimen and strain gage parallel to applied field *H* to give saturation magnetostriction $\lambda_{\|}$; b) Specimen and strain gage perpendicular to applied field *H* to give saturation magnetostriction $\lambda_{\perp}$. Note that the dotted outline represents an unstrained disk under zero applied field conditions.

Saturation magnetostriction measurements of Fe-Ga samples, depending on the particular specimen, utilized disk geometries with diameters from 6.4 to 7.9 mm and thickness values ranging from 0.1 to 0.38 mm. For these dimensions the geometric demagnetizing factors are no worse than ~ 1%, therefore internal fields are approximately equal to applied fields [Jiles 1998]. Disk specimens were subjected to a 9000 Oe applied field H which was generated in a 12.7-mm air gap between neodymium-boron magnets. Annealed low-carbon steel provided a closed magnetic flux return path between the permanent magnets. To measure magnetostrictive strains, each strain-gaged disk specimen was rotated through 360° in 1.8° increments by a computer controlled stepper motor. The strain data was collected under static conditions when the specimen rotation paused momentarily at each angular position.

2.2 Single Crystal

Single crystal disk and rod shaped test specimens were extracted from single crystal parent material. The production methods of the parent material are described first with the saturation magnetostriction results to follow.

2.2.1 Materials preparation

Single crystals of $Fe_{83.8}Ga_{16.2}$ and $Fe_{80.6}Ga_{19.4}$ were produced in two separate production runs. Each crystal was grown in an alumina crucible by the modified Bridgman technique. The starting ingot for single crystal growth was prepared by arc-melting appropriate quantities of Fe (99.99% purity) and Ga (99.999% purity) metal several times under an Ar atmosphere. The button was then remelted, and the alloy was drop cast into a Cu chill cast mold to ensure compositional homogeneity throughout the ingot.

The alloy was heated under a pressure of 1.3×10^{-4} Pa up to 1075 K to degas the crucible and the ingot. The chamber was then backfilled to a pressure of 275 kPa with high purity Ar. The ingot was then further heated to the growth temperature and held for 1 hour to allow thorough mixing before withdrawing the sample from the heat zone at a rate of 4 mm/h. Following growth, the ingot was annealed at 1000°C for 168 hours and furnace cooled. X-ray diffraction analysis confirmed the crystal's single-phase, fully disordered α structure.

Each single crystal's orientation was determined within 0.25° using Laue X-ray back reflection analysis and then cut into a disk shape by electro-discharge machining (EDM). Disk orientations matching a $(1\bar{1}0)$ plane were chosen to contain both <100> and <111> crystallographic directions simultaneously (see Figure 1.1b). After machining, the orientation of each specimen was again checked by Laue X-ray back reflection analysis. The disk faces were polished with progressively finer wetted silicon carbide paper to 600 grit to provide smooth parallel surfaces.

2.2.2 Saturation magnetostriction - single crystal results

The saturation magnetostriction of the $Fe_{83.8}Ga_{16.2}$ and $Fe_{80.6}Ga_{19.4}$ crystals were measured using the directionally applied magnetic field method described in Section 2.1. Two individual tests were run on each specimen using a Measurements Group EA 06-062AQ-350 strain gage attached in either the [100] or [111] direction to measure $(3/2)\lambda_{100}$ and $(3/2)\lambda_{111}$ respectively. Figure 2.2 shows the saturation magnetostriction along the [100] crystal direction for the Fe-19.4Ga at.% disk specimen. The strain response follows a cosine squared function with the peak to peak value for $(3/2)\lambda_{100} = 283 \times 10^{-6}$.

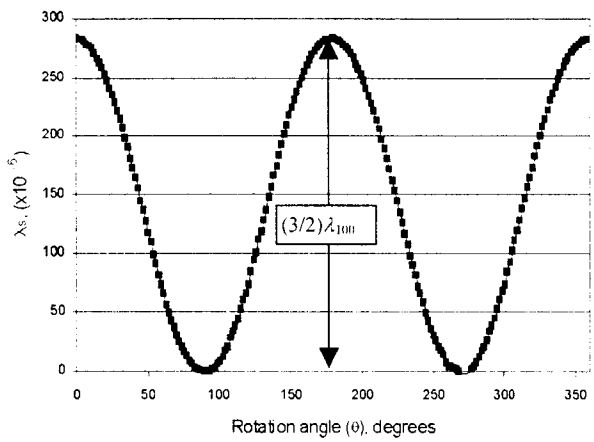

Figure 2.2 Saturation magnetostriction response along the [100] crystallographic direction of a $(1\bar{1}0)$ $Fe_{80.6}Ga_{19.4}$ disk with 7.9-mm in diameter and 1.0-mm thick. Disk rotation angle θ denotes the direction of the saturating applied magnetic field is relative to the disk's [100] direction.

Figure 2.3 depicts the saturation magnetostriction along the [111] crystal direction contained within the same Fe-19.4Ga at.% disk used for Figure 2.2. The strain response

roughly follows cosine squared function with the peak to peak value for $(3/2)\lambda_{111} \sim 18 \times 10^{-6}$. The strain amplitudes in this case are approximately 1/16 that of the [100] measurement, therefore noise is more evident in the plotted data.

The saturation magnetostriction of the $Fe_{83.8}Ga_{16.2}$ disk specimen was measured in a similar manner to give $(3/2)\lambda_{100} \sim 285 \times 10^{-6}$ and $(3/2)\lambda_{111} \sim -30 \times 10^{-6}$. It should be emphasized that none of these disk specimens were quenched. As a consequence, the $Fe_{82.6}Ga_{19.4}$ λ_{100} performance is not optimal due to the possible formation of an ordered $D0_3$ phase having lower magnetostriction capability. The values of $(3/2)\lambda_{100}$ and $(3/2)\lambda_{111}$ from Figure 1.5 of are reproduced below in Figure 2.4 with the addition of the new data points. The $(3/2)\lambda_{111}$ value for the Fe-16.2Ga disk appears to be approximately 10×10^{-6}, which is more negative than expected. Additional testing is needed to verify the source of this discrepancy. These results will find later use in the magnetostrictive micro mechanics model of Chapter 5.

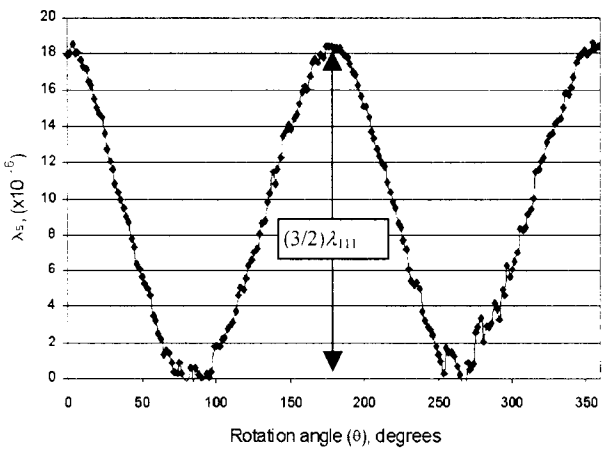

Figure 2.3 Saturation magnetostriction response along the [111] crystallographic direction of a $(1\bar{1}0)$ $Fe_{80.6}Ga_{19.4}$ disk with 7.9-mm diameter and 1.0-mm thick. Disk rotation angle θ denotes the direction of the saturating applied magnetic field is relative to the disk's [111] direction.

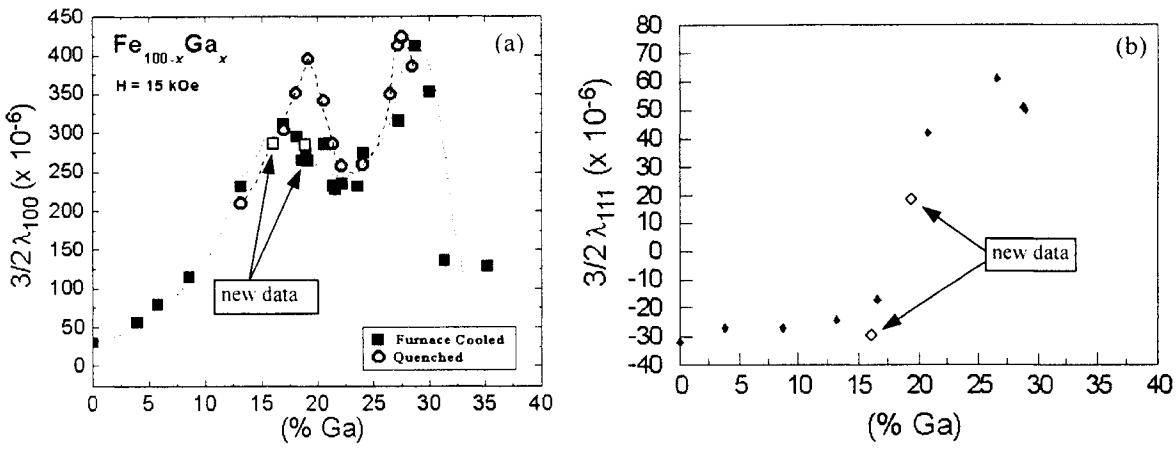

Figure 2.4 Magnetostrictive constants for Fe-Ga single crystal alloys as a function of at. % Ga concentration. New data for 15.3 and 19.4 Ga at.% is included. a) $(3/2)\lambda_{100}$ for quenched and furnace cooled heat treatments, b) $(3/2)\lambda_{111}$ for furnace cooled heat treatment. [Clark *et al.* 2003].

2.3 Polycrystalline preparation and performance

While single crystalline materials inherently provide the maximum crystallographic texture and hence magnetostriction, the cost of the processing for large volume production may preclude broad commercialization due to low yield and non-uniform properties. An alternative to single crystals is to process the material in polycrystalline form in such a manner that the structure possesses a high degree of crystallographic texture. Process approaches that appear promising include growth texturing in an as-cast structure and the preferential recrystallization of thin sheets. Deformation texturing methods of interest, based on success in texturing of Fe-Si and Fe-Al alloys, include extrusion, forging and rolling [Nachman 1954, Kad 1997, Novikov 1997]. A final potential texturing process includes the use of an aligning magnetic field in conjunction with powder metallurgy. An alloy stoichiometry of $Fe_{83}Ga_{17}$ was used for the texturing experiments to minimize the possible formation of intermetallics found with higher gallium compositions. The powder metallurgy work utilized $Fe_{80}Ga_{20}$ due to material availability.

2.3.1 Growth texturing – directional solidification

Fe-Ga alloys can be directionally solidified at rates sufficiently fast to yield dendritic solidification along the length of the ingot. Dendritic solidification occurs along specific

crystallographic directions, thereby aligning different crystals within the ingot with a common growth direction. A directionally solidified $Fe_{83}Ga_{17}$ specimen was grown in an alumina crucible by the modified Bridgman technique. Preparation of the starting ingot prior to the growth process was identical to that used for the single crystal (Section 2.2.1). The ingot was heated to the growth temperature and held for 1 hour to allow thorough mixing before withdrawing the sample from the heat zone at a rate of 100 mm/h. Following growth, the ingot was annealed at 1000°C for 168 hours then furnace cooled. A 50.8-mm long rod-shaped specimen having a 6.35-mm diameter was sectioned from the ingot using EDM. The rod's longitudinal axis was approximately parallel with that of the ingot's longitudinal axis.

Centerless grinding was next attempted to refine the rod geometry, however during grinding the specimen underwent brittle fracture to produce several pieces. Visual inspection of the fractured portion revealed that the rod was a multicrystal composed of approximately a dozen grains. These grains were 2 to 4 mm in diameter and generally elongated in the growth direction (along the rod axis) with up to 20-mm lengths. To discover the failure mode of the specimen, portions of the broken rod were impacted lightly with a hammer. Additional failure was observed to occur along grain boundaries thus releasing individual crystals. Attempts to fracture individual crystals with the hammer were fruitless as the material underwent extensive ductile deformation. The directionally solidified rod's brittle failure mode at the grain boundaries and ductile grains suggest that Ga-rich intermetallics may have formed along the grain boundaries and/or Ga may have precipitated at the grain boundaries.

Despite the machining difficulties, a rod specimen with a 28.1-mm length was recovered from the directionally solidified ingot for magnetostriction analysis. The saturation magnetostriction capability of the rod was tested in a thermally controlled transducer using a constant stress and quasi-static applied magnetic fields up to 74 kA/m. An optimized stress level of 28 MPa for this specimen (see Chapter 4) gave the result of $(3/2)\lambda_s \sim 170 \times 10^{-6}$. This saturation magnetostriction output is ~55% that of the [100] oriented $Fe_{83}Ga_{17}$ single crystal's performance (Figure 2.4a). Orientation imaging microscopy (OIM) analysis on the plane normal to the growth axis (Figure 2.5) shows that dendrite growth favored the [100] crystal orientation in the longitudinal direction. Additional analysis of the directionally solidified specimen's overall magnetic response is reviewed in Section 3.3. The figure's

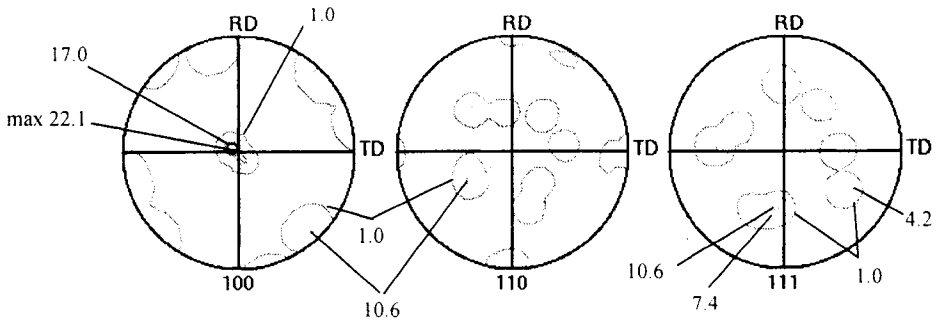

Figure 2.5 OIM crystallographic texture map for the plane normal to the growth axis of directionally solidified $Fe_{83}Ga_{17}$ rod.

stereographic projection labels "RD" and "TD" mark reference directions for the crystallographic analysis and correspond respectively to the rolling direction and transverse direction for a sheet texture. However, these reference directions are irrelevant in this case given the axial symmetry present for the end-view of the rod-shaped specimen.

The directionally solidified specimen's combination of modest magnetostrictive performance, and susceptibility to intergranular brittle failure indicates that this approach for producing a textured polycrystalline Fe-Ga alloy may not be ideal. Although adjustments might be made in the growth and annealing processes to improve results, other texturing methods were investigated for superior performance.

2.3.2 Deformation processing

Due to the only recent recognition of Fe-Ga alloys' potential value, no successful work has been published regarding the development of crystallographic texture in these alloys using deformation processing. However, the deformation properties and texturing of Fe, Fe-Al and Fe-Si alloys have long been studied due to their scientific and commercial value. Fortunately the substitutional elements Al and Si have a similar atomic radius to Ga (~ 110% that of Fe) for the coordination number of 8 (i.e. 8 atoms as nearest neighbors with which to interact) found in the BCC disordered α-Fe phase. Given these crystallographic similarities, deformation texturing methods for Fe, Fe-Al and Fe-Si are used as a starting point to investigate deformation texturing techniques in Fe-Ga alloys. Extrusion, forging and rolling experiments were carried out on as-cast starting material. The degree and type of

texture developed was measured by several means: saturation magnetostriction performance of disk or rod shaped specimens, back-reflection electron microscopy, X-ray crystallography and OIM.

2.3.2.1 Extrusion

Extrusion is often used as a production step in forming wire out of many metals including Fe and Fe alloys. The extrusion process entails pushing the as-cast starting material (usually heated to facilitate plastic flow) through an opening of reduced cross sectional area. This is much like squeezing a tube of toothpaste to force it out the opening. Further reduction in cross sectional diameter and increases in length of the extruded material are typically accomplished through swaging. Swaging involves somewhat similar plastic flow patterns as those found in extrusion. Swaging is typically a cold working process which involves symmetrically hammering the wire in the radial direction to reduce the diameter. During swaging, the material is moved longitudinally through successively smaller die to reach the final cross sectional dimension. Fe wire, produced by extrusion and swaging, has been shown to possess elongated grains having a {001}<110> cylindrical texture [Leber 1961]. In this cylindrical texture (or "wire" texture), grains' <110> crystallographic axes lie parallel to the long axis of the wire while the {001} planes of the crystals lie normal to the radial direction. (This orientation is 45° off the desired <100> longitudinal orientation for maximum magnetostriction in Fe-Ga alloys.) Studies have shown that the resulting wire texture in BCC Fe is independent of the starting texture and strongly stable to variations in processing conditions [Barrett 1939]. It has also been observed that the recrystallization texture is <110> in Fe [Barrett 1952].

To investigate whether the texture development in Fe-17Ga at.% alloy is similar to that of Fe, an extruded rod-shaped specimen was produced for saturation magnetostriction testing. To form the extruded rod, a 25.4-mm diameter ingot of $Fe_{83}Ga_{17}$ was produced by arc melting and chill casting. The ingot was encapsulated into a cooper can and extruded in a Loewy Hydropress. The cast ingot was extruded at elevated temperature and pressures with an area reduction ratio of $A_{initial}/A_{final} \sim 4$. The extruded rod's approximate final dimension was 12 mm in diameter and 200-mm long. Figure 2.6 shows the parameters of the extrusion

process, including pressure, temperature and ram travel as a function of time. Throughout the extrusion process the temperature was ramped from room temperature to a maximum of 800 °C. From the beginning of the process to about 1400 seconds, ram displacement caused the pressure on the ingot to increase from zero to the machine's operating limit of 60 ksi (414 MPa). Continued heating of the ingot finally resulted in extrusion and a corresponding drop in pressure beginning at 1800 sec and 710 °C. The specimen was allowed to air cool following extrusion.

The extruded rod exhibited good toughness as it withstood several throws onto a cement floor. The rough treatment produced minor bending but no discernable fractures. A 50.8-mm length of the extruded rod withstood centerless grinding without failure down to a final diameter of 6.35 mm. This machined rod was next used for testing in a thermally controlled transducer. Quasi-static magnetostriction testing at room temperature using a 28 MPa compressive stress revealed that $\lambda_{max} \sim 60 \times 10^{-6}$. Assuming that the compressive stress bias pre-aligns all moments perpendicular to the rod's axis and that the applied field next drives the sample to saturation magnetization, then $(3/2)\lambda_s = \lambda_{max} \sim 60 \times 10^{-6}$. (A demagnetized specimen without a stress bias would produce a magnetostriction of λ_s in response to a saturating applied field. The factor of 3/2 follows from Equation 1.4) This level of magnetostriction is roughly 20% that of a [100] single crystal, thus indicating that the desired <100> texturing has not been achieved. Consistent with this magnetostriction result, an OIM analysis of the specimen (Figure 2.7) indicated a high degree of <110> texture along

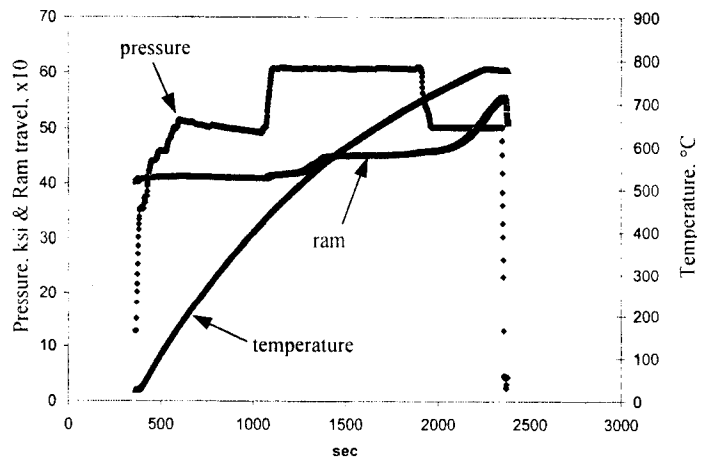

Figure 2.6 Extrusion parameters for the Loewy Hydropress acting on a 25-mm diameter drop-cast ingot of $Fe_{83}Ga_{17}$.

the rod axis. The <100> texture is widely distributed at approximately 45° and 90° from the longitudinal axis. Unfortunately, determining whether the extruded specimen possesses a fiber or wire texture, with their respective random or radial distribution of the <100> crystal axes, is not possible from this information.

In an attempt to ensure homogenization of the Ga distribution and ultimately improve the magnetostriction, the extruded rod was annealed at 800 °C for 4 hours then water quenched. Subsequent saturation magnetostriction testing, using conditions identical to those used before the specimen was annealed, gave $(3/2)\lambda_s$ = 30 x10^{-6} for a 50% loss in performance. An X-ray derived stereographic projection of the texture distribution of the annealed rod (Figure 2.8) shows that a strong <110> texture has been enhanced. The general

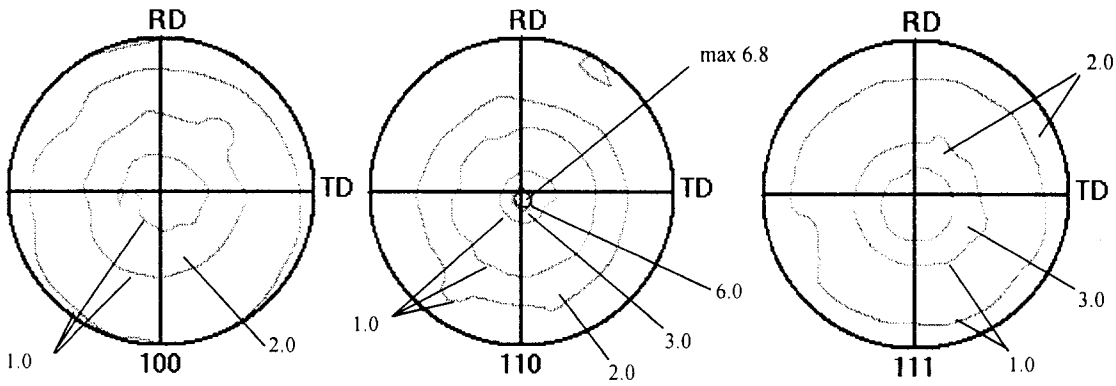

Figure 2.7 OIM derived stereographic projection of the crystallographic distribution for extruded $Fe_{83}Ga_{17}$. Data collected for the plane normal to the longitudinal axis of the extruded rod.

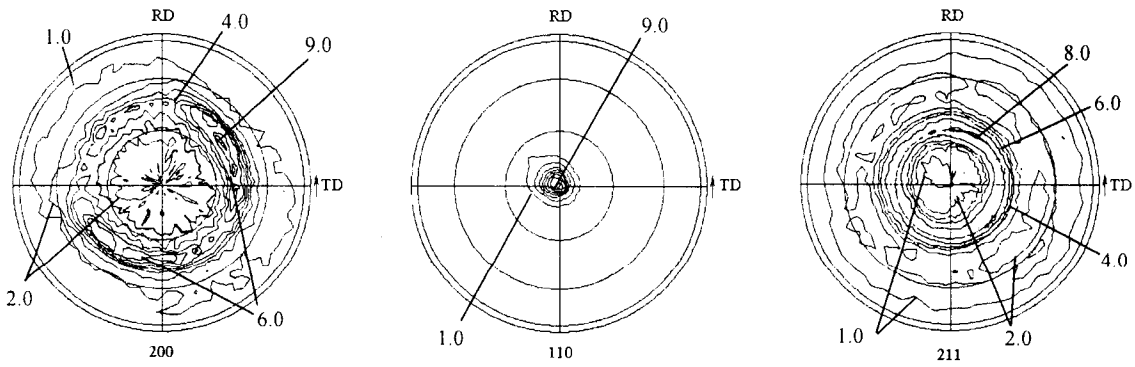

Figure 2.8 X-ray derived stereographic projection of the crystallographic distribution for extruded $Fe_{83}Ga_{17}$ subjected to a 4 hr anneal at 800°C and water quench. Data collected for the plane normal to the longitudinal axis of the extruded rod.

symmetry of the <200> and <211> pole figures, about the samples longitudinal axis, is consistent with either a <110> fiber or wire texture. Further analysis of the texture evolution, going from the non-heat treated to the annealed specimen, has questionable value given the different techniques (OIM and X-ray) used for each. The non-heat treated specimen was not available for further examination.

Although the anneal-induced loss in the extruded rod's magnetostrictive capability was not anticipated, it might be attributed to residual stress or a strengthening of the <110> texture component at the expense of <100> oriented grains. Another possible cause for the loss is that recrystallization events during annealing induced formation of additional yet weak <111> and/or <112> texture components (not obvious in Figure 2.8) in the direction of the rod's longitudinal axis. This second possibility is discussed next as it may dramatically affect the bulk magnetostriction of the rod and has a potentially intriguing source.

Considering the anisotropic magnetostriction relationship (Equation 1.4) and using the $Fe_{83}Ga_{17}$ material properties of $(3/2)\lambda_{100} = 310 \times 10^{-6}$ and $(3/2)\lambda_{111} = -16 \times 10^{-6}$ (from Figure 2.4), the reduction in the annealed extruded rod's saturation magnetostriction would be consistent with a decline in the specimen content of <110> grains and an increase in content of <111> and <112> grains. For longitudinally oriented single crystals with a magnetic moment rotation from a [001] direction nearest the rod's radial direction into a [110], [111] or [112] direction, $(3/2)\lambda_s$ declines from 147×10^{-6} for the [110] orientation to -11×10^{-6} and -61×10^{-6} for the [111] and [112] directions respectively.

Insight into the possible anneal-induced increase of <111> and <112> textures in Fe-Ga alloys might be gained by considering earlier research by Bhandary *et al.* In their work, the development of additional <111> and <112> texture components were observed in Fe wire specimens that were recrystallized at 600 - 650°C for 30 min in the presence of DC 10 - 90 Oe magnetic fields [Bhandary 1962]. The development of these magnetically induced <111> and <112> recrystallization textures were attributed to magnetostriction induced strain energy and/or magnetocrystalline anisotropy and their effect on the grain nuclei stability [Smoluchowski 1949, Sawyer 1957]. Although the extruded rod in this work was not intentionally subjected to magnetic fields during annealing, examination of the processing equipment revealed that the Ames Lab NRC furnace has heating elements that produced an

AC 140 Oe magnetic field. Supposing the longitudinal axis of the extruded specimen was oriented coaxially with this field, the effect may have contributed to the development of a particular recrystallization texture.

A more extensive investigation of the extruded specimen's crystallographic orientation distribution must be conducted to understand the anneal-induced loss in the specimen's magnetostrictive capability. Despite this deficiency, an analysis of the magnetic characteristics, before and after annealing, is presented in the magnetic characterization Section 3.3. Given the extruded specimen's low saturation magnetostriction capability, mechanical testing to determine the specimen's elastic and plastic properties was not conducted.

2.3.2.2 Hot forging

Deformation processing techniques in Fe-Al based alloys have been used in the past to develop crystallographic textured products having a high degree mechanical anisotropy. Particularly relevant to the present goal of <100> texturing in Fe-Ga alloys, studies by Kad *et al.* of iron aluminides ($Fe_{1-x}Al_x$, where $15 \leq x \leq 20$) indicate that hot axial forging (above 550°C) causes a significant crystallographic reorientation and produces a dominant <100> fiber texture parallel to the direction of forging [Kad 1997]. It was determined that achieving a high degree of <100> texturing required true strain ≤ -1 and that texturing success was independent of strain rate.

To discover if hot forging could generate a significant <100> fiber texture in Fe-Ga alloys, a $Fe_{83}Ga_{17}$ ingot with a 12.7-mm diameter and 100-mm length was produced in the usual manner by arc melting and chill casting. An initial attempt to centerless grind the cast ingot and remove surface casting defects resulted in intergranular brittle failure. The break occurred transverse to the ingot's longitudinal axis and was initiated at the root of a surface defect less than 1-mm deep. Centerless grinding was successfully used on a shorter portion of the ingot to produce an 11.8-mm diameter rod, 53.6-mm long. The rod ends were carefully ground normal to the rod axis to attain a geometry as close as possible that of a right cylinder.

To successfully forge the Fe-Ga rod buckling must be avoided while the longitudinal dimension undergoes true strain of -1.0 or more. The critical length to diameter ratio for buckling was estimated by assuming the least favorable boundary conditions for the rod ends as pin- pin. In this case, the critical load P_{cr} at which point buckling is imminent for a rod of length L, radius r, Young's modulus E and second moment of inertia I is

$$P_{cr} = \frac{\pi^3 EI}{L}, \qquad \text{where } I = \frac{\pi r^4}{4}.$$

Substituting the critical stress $\sigma_{cr} = P_{cr}/A$ where the cross sectional area $A = \pi r^2$ and rearranging produces the critical length to diameter ratio.

$$\left[\frac{L}{D}\right]_{cr} = \frac{\pi}{4}\sqrt{\frac{E}{\sigma_{cr}}} \tag{2.1}$$

Conservative room temperature values for the Fe-Ga alloy are $E \sim 56$ GPa and $\sigma_{cr} \sim 450$ MPa where the critical stress is simply equivalent to the expected yield stress [Lograsso 2000]. To make a rough estimate of $[L/D]_{cr}$ for buckling of the Fe-Ga rod at a forging temperature of 700°C, the values for E and σ_{cr} are reduced by factors of 2 and 3 respectively [Lyman 1948]. Using these numbers in Equation 2.1 gives $[L/D]_{cr} \sim 11$ for the hot forging process. Since the machined rod used for this experiment has a $L/D \sim 5$ buckling problems would likely be avoided.

Forging of the Fe-Ga rod specimen was conducted in a computer controlled 223 kN capable hydraulic MTS machine operated in constant velocity mode. The forging setup (Figure 2.9) utilized two cylindrical mild-steel mounting blocks (89-mm diameter and 54-mm long) to serve as an interface for the loading ram and cross arm of the MTS machine. The large thermal mass of these mounts was used to protect the MTS machine from the hot forging specimen. The specimen was enclosed in a soft firebrick and mounted in between two stainless steel platens (50.8 x 50.8 x 12.7 mm). The firebrick was used to limit cooling during the forging process as well as stabilize the specimen in between the platens during handling. The specimen, firebrick and platen assembly were secured into one unit using stainless steel wire and heated in a furnace prior to forging. The stainless steel platens were keyed to the mounting blocks and also contained 0.8-mm deep recesses to constrain lateral motion of the forging rod.

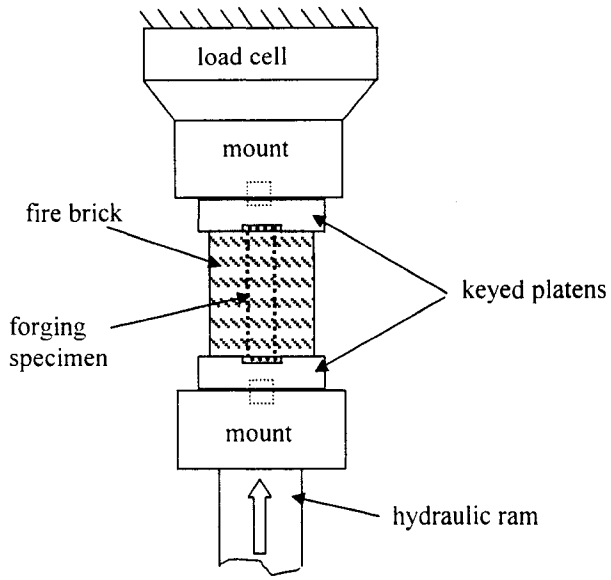

Figure 2.9 Schematic for the hot forging of a $Fe_{83}Ga_{17}$ cast rod (89-mm diameter, 54-mm long) using a hydraulic MTS machine.

To carry out the forging process, the specimen and platen assembly was heated to 700°C then placed between the mounts. The MTS machine was immediately activated to compress the sample over a 0.5 second period. A plot of the load vs. ram displacement (Figure 10a) shows that plastic flow began at ~ 16 kN (or 140 MPa based on the original cross sectional area) and that the specimen length was compressed by 33.7 mm (true strain = -1). The increase in load throughout the forging process is attributed to increasing cross sectional area and specimen cooling. After forging, the deformed specimen (Figure 2.10b) was retrieved from the crushed firebrick then water quenched.

The plastic flow arising during the forging process was complex and asymmetrical (Figure 2.10b). In regions enclosed by the white dashed lines, the grains are mostly equiaxed and undisturbed. The mid-length of the rod generally flowed to the right and away from a horizontal line bisecting the specimen as shown by the solid arrows. Grains were elongated in the direction of the flow. The cross section of disk specimens (7.9-mm diameter, 1.0-mm thick), which were later extracted for saturation magnetostriction testing, are indicated for orientations parallel and perpendicular to the material flow direction.

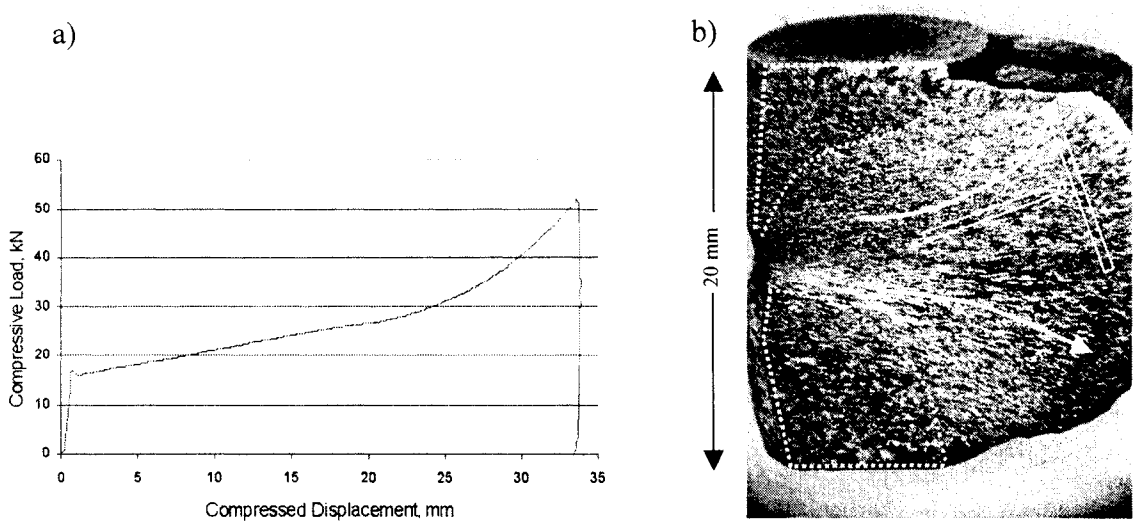

Figure 2.10 Forging response: a) Compressive load generated as a function of compressed displacement from original length; b) Cross section of forged $Fe_{83}Ga_{17}$ rod (forging direction is vertical). Regions of equiaxed grains are enclosed by the dotted lines. The plastic flow pattern is indicated by the white arrows. The cross section of extracted disk specimen orientations parallel and perpendicular to the flow are outlined.

Considering the forged material's complicated flow pattern, occurring over short distances relative to the diameter of the disk specimens, the saturation magnetostriction of each disk specimen was evaluated in multiple directions using a BLH type FABR-12-12-S6 strain gage rosette. The directional saturating applied magnetic field method, previously described in Section 2.1, revealed poor saturation magnetostriction values for both parallel and perpendicular disk specimens. These results were generally independent of measurement direction relative to the forging induced direction of material flow with the saturation magnetostriction values ranging from 18 $x10^{-6}$ to 35 $x10^{-6}$.

The low magnetostrictions observed in the hot forged specimens are likely due to a lack of favorable texture (or any texture) and possibly significant residual internal stress developed during quenching. Forging at lower temperatures and to higher strains as well as using starting rods with a significantly lower L/D ratio might improve results, however successfully producing monolithic Fe-Ga magnetostrictive components with adequate useful lengths in the direction needed for actuation becomes doubtful. Given the difficulty in producing a symmetric deformation and uniform directional material flow with this forging approach, further material characterization was not conducted.

2.3.2.2 Cold forging

The possible development of a strong <100> texture in Fe-Ga alloys through forging remains an interesting prospect despite the difficulties encountered with hot forging of large single-piece specimens. In this section, the deformation texture developed in Fe-Ga powder as a result of cold forging is examined. Should the cold forging process create flat disk-shape particles with a plane normal <100> texture, these forged particles might be sintered into wire possessing a <100> texture along the longitudinal axis.

Multicrystal $Fe_{80}Ga_{20}$ spherical powder with a nominal diameter of 50 μm was cold forged in an arbor press between highly polished tool-steel surfaces. The spherical particles were forged in a single compression step to form disk-shaped particles approximately 17-μm thick and 100-μm in diameter. A maximum true strain of -1.1 was imparted along the particle diameter in the forging direction. (Strain magnitudes larger than this resulted in cracking.) A flat face of each of the disk-shaped particles was next adhered to a glass slide one particle layer deep to cover a circular area having a 12-mm diameter at ~50% density. An X-ray derived pole plot (Figure 2.11) shows that cold forging induced the development of moderate <200> and <211> texture components. (The presence of a <200> texture translates directly the presence of a <100> texture provided that the signal strength is adequate, since these Miller indices are scalar multiples of one another. The use of a <200> notation is a result of the particular X-ray analysis setup and data processing.) Since only the diameter of each particle experienced a significant strain, substantial deformation was limited to a small

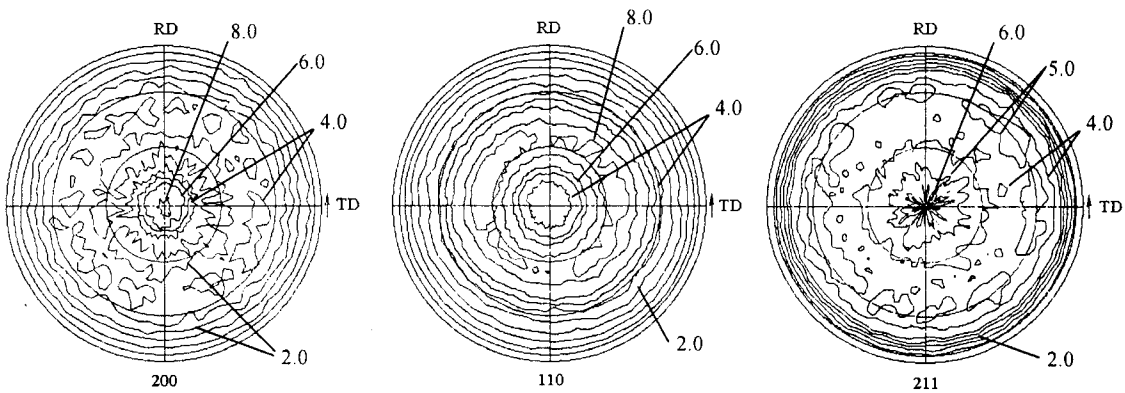

Figure 2.11 X-ray pole plot of cold forged 50-μm $Fe_{80}Ga_{20}$

portion of the particles' overall volume. Further forging deformation was attempted through the use of higher loads on the arbor press but particle cracking occurred. Strengthening of the <200> texture might be achieved through intermediate heat treatments and additional forging. Improved ductility of alloys having a lower Ga content than the 20% used here would likely facilitate larger deformations.

2.3.2.3 Rolling

Although little known work has been undertaken to develop crystallographic texture through the rolling process specifically in Fe-Ga alloys, a significant research effort toward understanding and perfecting crystallographic texturing in other Fe-based alloys occurred between the 1930's and 1960's. This research was largely driven by commercial interest in developing Fe-Si alloys as efficient electrical transformer cores and Fe-Al alloys for magnetic uses as well as corrosion resistant structural applications. A literature review this work has revealed a breadth of variation in the choice of material stoichiometries as well as specific rolling and heat treatment combinations. A study of prior work on texture development in polycrystalline materials by V. Novikov in 1997 lead to the conclusion that there still remains a fundamental lack of understanding of the grain growth processes considered essential to texture development [Novikov 1997]. In short, successful texture development through rolling is yet regarded an art just as much as it is a science.

Metals deformed by rolling primarily develop crystallographic texture through grain deformation, based on their active slip systems and work induced recrystallization events. To facilitate the formation of a desired texture, a number processing parameters may be varied. Typical processing parameters include: material stoichiometry and impurities, rolling temperature, rolling speed, percent reduction, and intermediate and final heat treatments. Environmental conditions such as a reducing or oxidizing atmosphere are also regarded as having an important influence on impurity content (such as carbon and sulfur) as well as the dominant surface recrystallization texture. Figure 2.12 shows a schematic of the flat rolling process used to reduce the original thickness (A) of metal stock to a final thickness (D). The rollers (B) pull the material through by friction generated in the deformation zone (C).

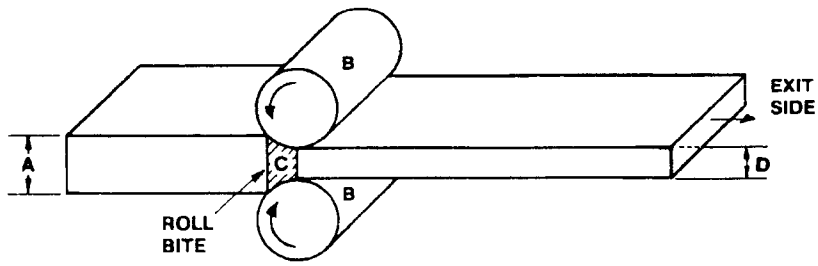

Figure 2.12 Schematic of the flat rolling process used to reduce the thickness of metal (After [Bowman 1980]).

Among the many rolling approaches available for developing <100> texture in the rolling direction in Fe-Al and Fe-Si alloys, the general scheme is to hot roll a cast ingot into a slab then proceed with one or more cold rolling and annealing iterations. The cold rolling steps typically employ thickness reduction exceeding 70% and facilitate the development of a refined crystalline structure generated through primary recrystallization during a subsequent anneal. The final cold rolling step is then followed by a final anneal under particular atmospheric conditions (inert, reducing or oxidizing) to cause secondary recrystallization. Ideally, a large number of grain nuclei are available with the proper crystallographic orientation, which are encouraged to grow at the expense misoriented grains. The simultaneous inhibition and promotion of growth of different grain orientations are influenced by small quantities of dispersed particles; examples include MnS, AlN and carbides among others [Novikov 1997]. With the proper adjustments to the general processing steps just described, two textures of interest may be produced. The well known "Goss" or "cube on edge" texture provides a {110}<100> oriented sheet having a single easy magnetic axis. A second and even more desirable texture is the "cube" texture, which consists of a {001}<100> oriented sheet and possesses two orthogonal magnetic easy axes. Either the Goss or cube texture could provide Fe-Ga sheet with the maximum magnetostrictive capability of $(3/2)\lambda_{100}$, however the cube sheet is most versatile and magnetically efficient with its two in-plane <100> axes and single plane-normal <100> axis.

Of the dozens of patents and research studies examined, several flat rolling approaches appeared most promising as a way to generate a favorable texture in the Fe-Ga

alloy. The following summary lists several approaches by their inventor's/researcher's names and includes the material used and texturing objective:

- Nishihara (1966 US patent #3,279,960) – Used as cast $Fe_{100-x}Al_x$ where $4 \leq x \leq 12$ alloy to yield cube textured sheet.
- Walter (1965, published in Journal of Applied Physics) - Used thin $Fe_{97}Si_3$ sheet and H_2S or O_2 annealing atmosphere to favor {001} sheet formation through surface energy control.
- Littmann (1948 US patent #2,599,340) – Used as cast $Fe_{100-x}Si_x$ $2.5 \leq x \leq 4$ to yield Goss texture sheet.
- Kohler (1964 US patent #3,130,192) – Used $Fe_{100-x}Si_x$ $1 \leq x \leq 6$ Goss textured sheet to yield cube texture sheet.
- Pavlovic (1962 US patent #3,058,857) – Used as cast $Fe_{100-x}Al_x$ where $2 \leq x \leq 19$ alloy to yield cube textured sheet.

Time constraints limited the number of texturing approaches to be investigated in the course of this study on Fe-Ga alloys. Consequently, only the Nishihara rolling approach was followed in an attempt to produce textured sheet. Details of the rolling procedure are listed in Appendix A. Additional texture modifications to this resulting sheet were then attempted through annealing under various atmospheric conditions as suggested by Walter's research. Alternative but untried rolling techniques include use of the Littmann process to produce Goss textured starting material for the Kohler method and use of the Pavlovoc process as a stand alone approach to texturing.

A version of the Nishihara rolling procedure, modified for the Fe-Ga alloy used in this work, is presented next. A detailed schematic of the rolling procedure is listed in Appendix B. Saturation magnetostriction values are reported for disk specimens selected at key steps throughout the process. Stereographic projections of texture distributions are also provided for several specimens.

An $Fe_{83}Ga_{17}$ cast ingot, measuring 9.5 x 51 x 51 mm, was produced by arc melting Fe (99.99% purity) and Ga (99.999% purity) metal several times under an Ar atmosphere. Several buttons of this material were placed into a mold and subjected to arc melting under an Ar atmosphere to ensure compositional homogeneity throughout the ingot.

The starting ingot was enclosed in a 321 stainless steel can, backfilled with Ar, evacuated and sealed by welding to prevent oxidation of the specimen. To minimize diffusion bonding of the Fe-Ga specimen with the can during rolling, the can was preoxidized at 900°C in air for 1 hr. Following hot soaking at 1000°C for 30 min, the canned specimen was hot rolled to give a 55% reduction to a thickness of 4.2 mm over 72 passes. Throughout the hot rolling procedure, the canned specimen was reheated at 1000°C after every three passes for 6 minutes. A small reduction/pass was used to control cracking and limit uneven specimen deformation, while the accumulation of reductions served to refine the original cast grain structure. The hot-rolled specimen was next removed from the can (Figure 2.13) and annealed at 700°C for 60 min. in dry Ar then aged at 300°C for 150 min. A disk specimen at this stage in the processing, labeled R1 ("R" for rolled) gave, a saturation magnetostriction in the rolling direction of $\lambda_{RD-\perp} = 95 \times 10^{-6}$ compared to the transverse saturation magnetostriction value of $\lambda_{TD-\perp} = 35 \times 10^{-6}$. Up to this point the rolling process has generated some anisotropy in the magnetostriction, but the value of $\lambda_{RD-\perp}$ falls well short of the $\lambda_{||-\perp} = 300 \times 10^{-6}$ capability found in the [100] direction of single crystal material.

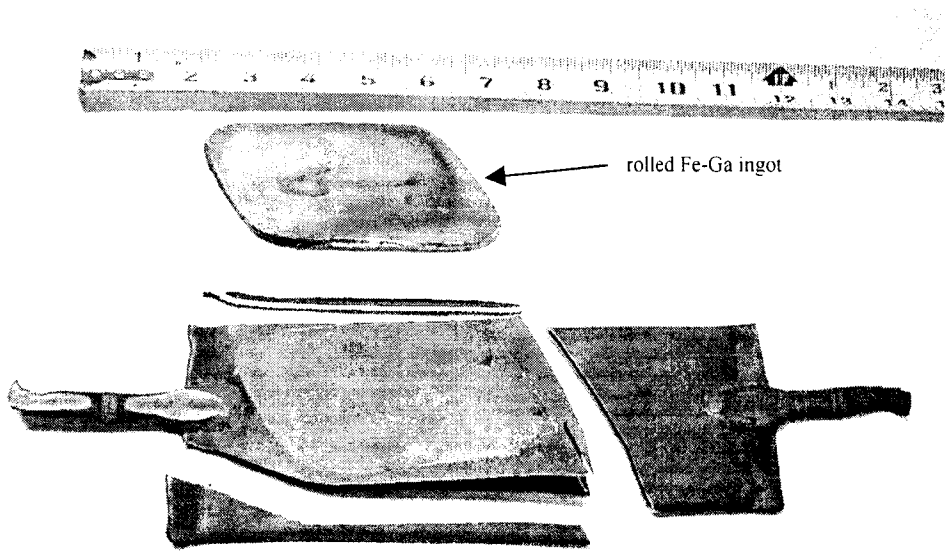

Figure 2.13 Fe-Ga cast ingot after hot rolling reduction of 55% at 1000°C and the sectioned 321 stainless steel can used to protect the FeGa alloy from oxidation at temperatures above 500°C. The rolling direction is indicated on the rolled ingot. The ruler is in inches.

After the previous annealing step, warm rolling at 300°C provided a 60% reduction over 36 passes to give a sheet 1.7-mm thick and 104-mm long. Cracks that had initiated at the edges of the sheet were ground out. These cracks, up to 3-mm long, had propagated inward and approximately perpendicular to the rolling direction. This sheet was next annealed at 700°C for 30 min. in dry Ar then aged at 300°C for 10 min. An additional 24% warm rolling reduction over 7 passes resulted in sheet 1.3-mm thick. A specimen labeled R2 was annealed in Ar at 475°C for 180 min. and then at 1100°C for 240 min. Testing of R2 showed $\lambda_{RD-\perp} = 100 \times 10^{-6}$ and $\lambda_{TD-\perp} = 70 \times 10^{-6}$. Modest magnetostriction at this point indicates that texture development, while improving, is still inadequate.

Following the warm rolling reduction to a 1.3-mm thickness, processing included the removal of cracks, a 700°C anneal and additional 42% reduction by warm rolling to give material with final length of 226 mm and thickness of 0.38 mm. The rolled alloy was then "pickled" or etched in an acid solution containing $20H_2O$:7HCl:$3H_2O_2$ by volume, to clean up the surface. At this stage three different annealing conditions were tested to evaluate their effect on recrystallization texture. These different annealing conditions include high-temperature anneals in Ar, H_2 and 20 ppm H_2S in H_2.

- Specimen R3 was produced by an anneal in flowing dry 99.99% Ar at 475°C for 180 min. then at 1100°C for 240 min. and finally allowed to furnace cool over 8 hours. As shown in the disk sample of Figure 2.14, the grains arising from the anneal-induced secondary recrystallization were up to 2 mm in diameter. Analysis confirmed that most grains were "through-thickness" grains (i.e. each grain spanned the disk thickness). Saturation magnetostriction testing for sample R3 showed that $\lambda_{RD-\perp} \sim 160 \times 10^{-6}$ and $\lambda_{TD-\perp} \sim 120 \times 10^{-6}$. Although these magnetostriction results in the RD are only half that of the single crystal capability, they are approximately 50% better than the values for the intermediate rolled specimens R1 and R2. To evaluate the Fe-Ga alloy's crystallography, an X-ray powder diffraction scan was used to check for the presence of a $D0_3$ intermetallic and an OIM derived stereographic projection was constructed.

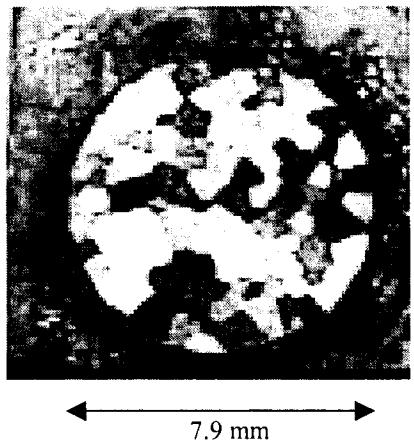

Figure 2.14 Optical micrograph of a 0.38-mm thick disk sample of polycrystalline $Fe_{83}Ga_{17}$, sample R3 produced by the modified Nishihara rolling procedure and recrystallized by Ar annealing. Note that the grain diameters are on the order of 1 mm and are through-thickness grains. Grain contrast was produced by etching in $20H_2O$:7HCl:$3H_2O_2$.

An X-ray powder diffraction scan (Figure 2.15) was collected for the range of $20° \leq 2\theta \leq 35°$. (The angle 2θ is the sum of the angle of incidence and reflection of the X-ray by the specimen surface and is governed by the atomic lattice spacing of the crystallographic structure.) A significant increase in the X-ray reflectivity over the baseline at 26.6° and 30.8° would confirm the presence of the $D0_3$ intermetallic [JCPDS 1997]. Although there are no peaks in this specimen at 26.6° and 30.8° one can only safely conclude that $D0_3$ was not detected.

A stereographic projection (Figure 2.16) of a portion of the R3 disk specimen's crystallographic orientation was collected for the <100>, <110> and <111> directions. The <100> pole figure shows a somewhat dispersed cube texture with <100> orientations 5.9 times more frequent than that of random within 5° of the RD and within 20° of the sheet normal. The <110> and <111> textures are more dispersed. Keeping in mind the mm-sized grains and the fact that only one hundred or so grains are present in this disk sample, other specimens heat treated in this fashion may show some deviation from these texture results. The crystallographic texture of this specimen is examined more rigorously in Section 5.3 where it is used for validation of the magnetostrictive micromechanics model.

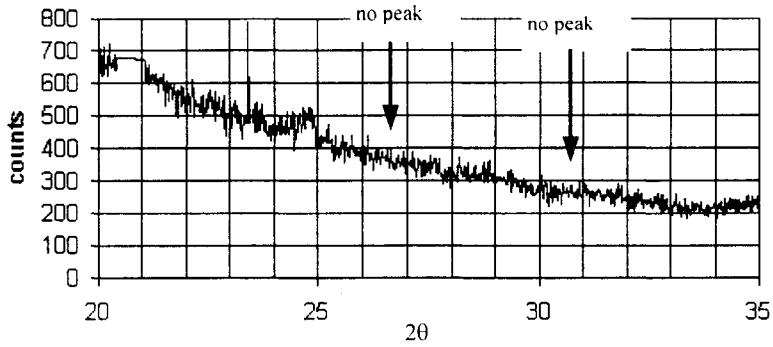

Figure 2.15 X-ray powder diffraction scan of polycrystalline $Fe_{83}Ga_{17}$, sample R3 produced by the modified Nishihara rolling procedure and Ar annealing. Lack of peaks at 26.6° and 30.8° indicates that the presence of a $D0_3$ structure was not detected.

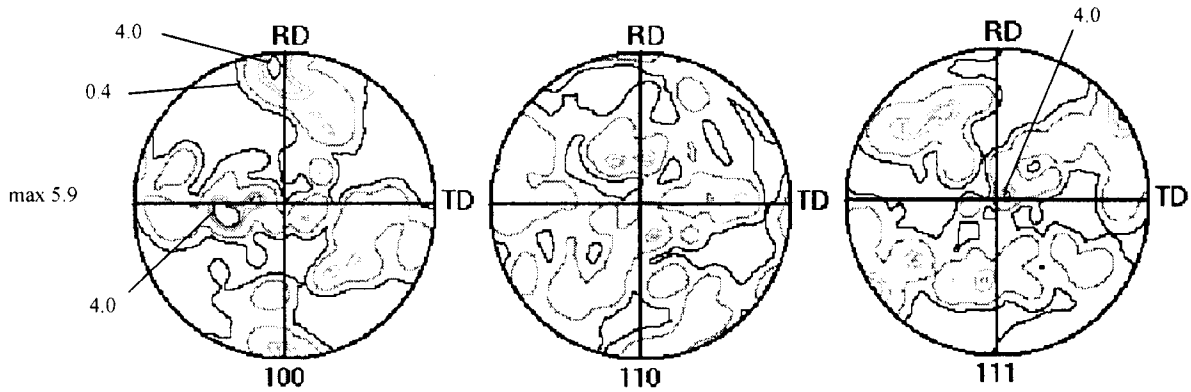

Figure 2.16 OIM derived stereographic projection of crystallographic orientation for polycrystalline $Fe_{83}Ga_{17}$, sample R3 produced by the modified Nishihara rolling procedure and Ar annealing.

- Specimen R4 was produced by annealing at a maximum temperature of 1170°C in an atmosphere containing 20 ppm H_2S and balance of H_2. The annealing gas mixture was controlled by metering 50 ppm H_2S premixed in H_2 with 99.999% pure H_2 using two FL300 Omega flow meters. The gas was pressure fed into a tubular quartz reaction chamber within the annealing furnace and flowed over the specimen at 16 cc/min. The annealing schedule (Figure 2.17) was designed to favor the growth of grains having a {001} sheet orientation and through-sheet thickness through the control of surface energy. The final phase of annealing in H_2 is intended to remove entrained sulfides and improve the alloy's magnetic and mechanical characteristics. A number of insightful studies detail how surface energy can be used to control grain growth, and given the right

starting texture, ultimately produce cube textured Fe and Fe-Si alloys [Walter 1965], [Dunn 1962], [Waeckerle 1993] and [Kramer 1992].

The grain morphology resulting from this annealing process was similar to that observed in sample R3 of Figure 2.14. Saturation magnetostriction testing of disk samples gave the results of $\lambda_{RD-\perp}$ ~120 x 10^{-6} and $\lambda_{TD-\perp}$ ~82 x 10^{-6}. These modest magnetostriction results suggest that some degree of <100> texturing is present, however it is not strong. As collected for the previous sample, an X-ray powder diffraction scan over a $20° \leq 2\theta \leq 35°$ range failed to confirm the presence of DO_3 structure. A stereographic projection of the crystallographic orientation collected with OIM is presented in Figure 2.18. Consistent with a somewhat lower RD magnetostriction, the <100> texture is more dispersed, as are the <110> and <111> components.

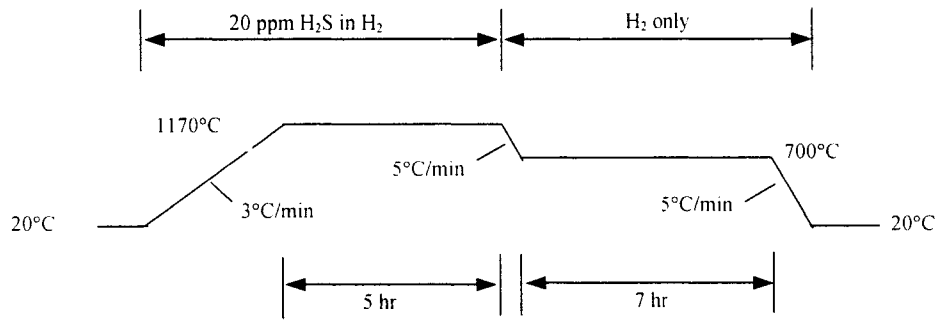

Figure 2.17 Annealing schedule to promote {001} sheet grain growth through surface energy control of secondary recrystallization for specimen R4. A flow rate of 16 cc/min of H_2 atmosphere containing 20 ppm H_2S was used.

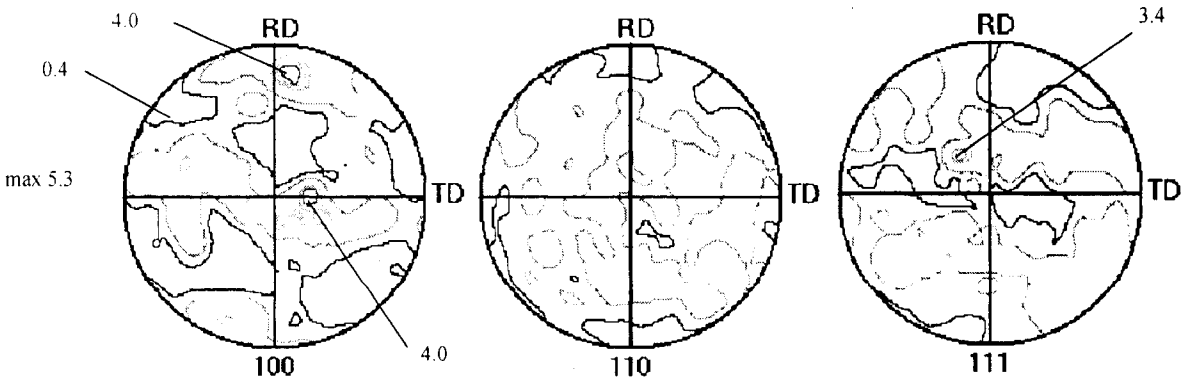

Figure 2.18 OIM derived stereographic projection of crystallographic orientation for polycrystalline $Fe_{83}Ga_{17}$, sample R4 produced by the modified Nishihara rolling procedure and H_2S annealing.

- Specimen R5 was annealed in flowing dry 99.999% H_2 at 475°C for 180 min. then at 1100°C for 240 min. and finally allowed to furnace cool. Testing showed $\lambda_{RD-\perp}$ ~109 x 10^{-6} and $\lambda_{TD-\perp}$ ~82 x 10^{-6}. As in the previous two samples, the recrystallized structure resulting from this high temperature anneal possessed mm-sized through-thickness grains. The modest magnetostriction again indicates that texture development remains weak under these annealing conditions. Crystallographic orientation distributions were not collected for this sample.

The grain morphology of the three high-temperature annealed specimens (R3, R4 and R5) all possessed a coarse grain structure and exhibited poor mechanical properties due to brittleness. Assessed qualitatively in each case using hand-held pliers, intergranular failure occurred after a one-time bending load induced less than a 20° deflection.

Returning to the 0.38-mm warm rolled material as the parent stock, two additional cold rolling and heat treatment procedures were undertaken in an effort to develop stronger <100> texture in the RD and more favorable mechanical properties. In the first cold rolling process, sample R6 was formed from the rolled parent material by a 55% reduction from 0.38 mm to 0.17 mm using 100 passes through a 2-high Stanat rolling mill. The rollers on this mill were approximately 460-mm long and 250 mm in diameter. The specimen was small in comparison having a width of only 15 mm. Work hardening of the material required an intermediate 500°C, 5 min. anneal (in air) after the first 28% reduction (30 passes) when the 890 kN roller load limit was reached. Thereafter, the specimen was annealed at 500°C for 10 min after every 10 passes. The cold rolling process was terminated after continued rolling at the 890 kN roller load limit could no longer produce any appreciable reduction in thickness despite further annealing. Roller deflection was significant in comparison to the specimen's small thickness and limited further reduction of the final specimen thickness. Saturation magnetostriction testing of disk samples cut from this material gave $\lambda_{RD-\perp}$ = 30 x10^{-6}. An additional 590°C anneal for 1 hr in H_2, to ensure stress relief, had little effect on the magnetostrictive performance. The sample was etched in $20H_2O$:7HCl:$3H_2O_2$ for 10 seconds to remove any residual strained surface material. Afterward an X-ray diffraction scan using a Cu k-α source (1.542Å) provided an averaged orientation distribution function to a depth of

~ 2μm. The stereographic projection (Figure 2.19) of these results indicates the presence of dispersed {100}<110> and {211}<110> textures, where the former is somewhat stronger.

To confirm whether other factors besides texture are affecting the rolled material's magnetostrictive capability, the alloy's stoichiometry and crystallographic structure were verified. Energy dispersive spectrometry (EDS) was conducted at several locations on the R6 specimen surface and results verified that the original $Fe_{83}Ga_{17}$ composition had been retained. An X-ray diffraction scan of the sheet surface (Figure 2.20) indicated a good match of the specimen with BCC Fe for {110}, {200}, {211}, {220} and {310} texture components. A small peak at $2\theta = 24.9°$ might be due to the presence of the {111} component of a $D0_3$ intermetallic (i.e. Fe_3Ga) whose peak would be expected near 26.6°. However, the probability of the $D0_3$ structure's presence is low as an additional peak near 30.8°, which corresponds to the diffraction of a {100} $D0_3$ plane, was not detected.

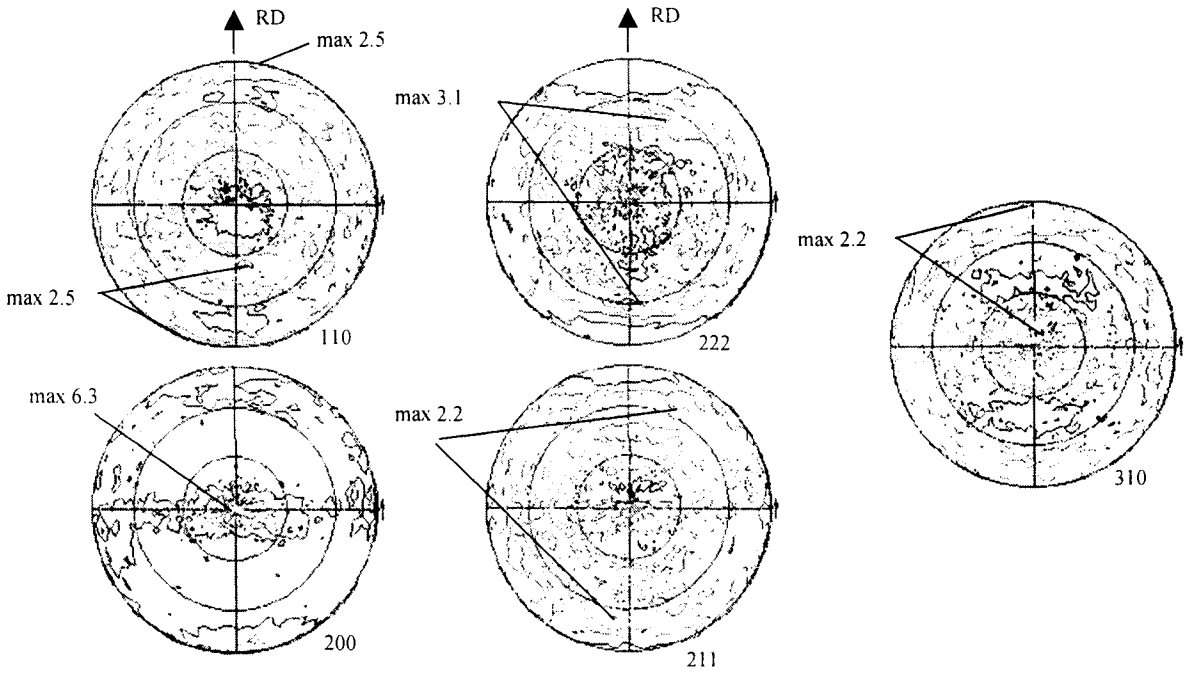

Figure 2.19 X-ray reflection derived stereographic projection of crystallographic orientation for polycrystalline $Fe_{83}Ga_{17}$ sample R6 produced by the modified Nishihara rolling procedure and additional cold rolling to a 0.17-mm thickness.

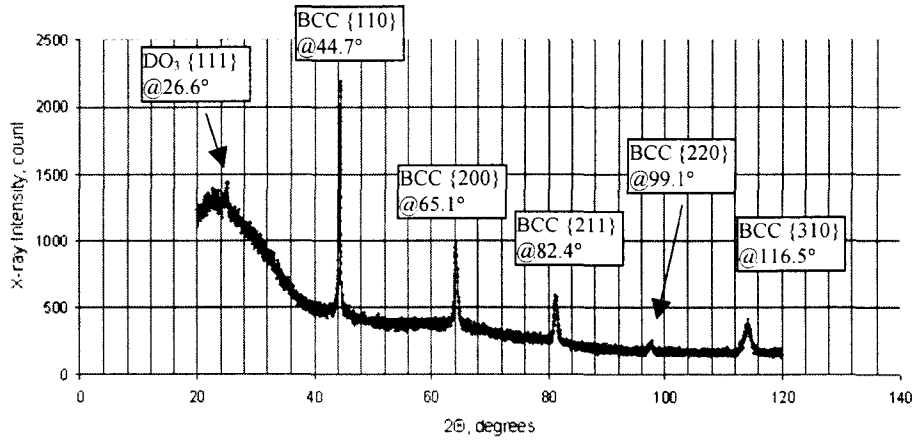

Figure 2.20 X-ray powder diffraction scan of polycrystalline $Fe_{83}Ga_{17}$, sample R6 produced by the modified Nishihara rolling procedure plus cold rolling to 0.17-mm thickness with 500°C intermediate anneals. The expected 2θ values for intensity peaks corresponding to BCC Fe are indicated. The lack of a peak at 30.8° indicates that the presence of a DO_3 {100} plane was not detected.

In the second cold rolling process, sample R7 was formed from the rolled parent material by a 73% reduction from 0.38 mm to 0.10 mm using 32 passes through a jeweler's rolling mill. The rollers on this mill were approximately 75-mm long and 50 mm in diameter and driven by a 0.5-hp electric motor. Work hardening of the material required three intermediate 500°C anneals in air, each with a duration of 5 min. The load imposed on the rollers was unknown and rolling was terminated when no further reduction in specimen thickness could be achieved. Following cold rolling, the specimen was given a 590°C anneal for 1 hr in Ar to ensure stress relief. A disk sample was extracted from the rolled sheet and then strain gaged with a 0/60/120 rosette. Saturation magnetostriction testing gave $\lambda_{RD\text{-}\perp}$ ~30 $x10^{-6}$ while the other two gage directions produced magnetostrictions of $\lambda_{\|\text{-}\perp}$ ~35 $x10^{-6}$. To evaluate the rolled texture, an X-ray diffraction scan was performed on the sample after etching in $20H_2O$:7HCl:$3H_2O_2$ for 10 seconds. The stereographic projection (Figure 2.21) indicates the presence of a major {100}<110> and minor {211}<111> texture components. Although these textures are somewhat dispersed they are more well defined than the texture of specimen R6 (Figure 2.19) which is less heavily rolled. The saturation magnetostriction for this specimen is later compared with the results of the magnetostrictive micromechanical model in Section 5.5.3.

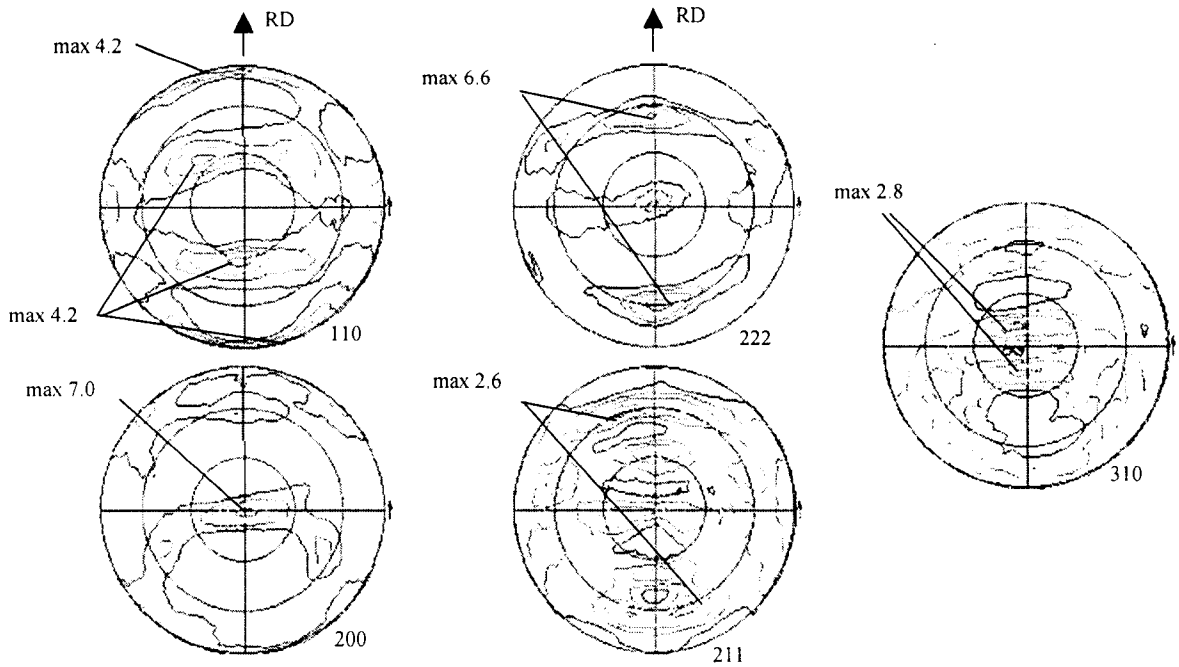

Figure 2.21 X-ray reflection derived stereographic projection of crystallographic orientation for polycrystalline $Fe_{83}Ga_{17}$, sample R7 produced by the modified Nishihara rolling procedure and cold rolled to 0.10-mm thickness.

The mechanical properties of these cold rolled specimens (R6 and R7) both exhibited good ductility. A qualitative hand-bending test (Figure 2.22) demonstrated that the material could be sharply bent with a radius less than 0.4 mm through 90° multiple times without failure. The superior ductility of this cold rolled material, subjected to only modest annealing temperatures, is due to the fine-elongated grain structure. A tension test quantifying the mechanical properties of sample R6 is presented in Section 4.3.

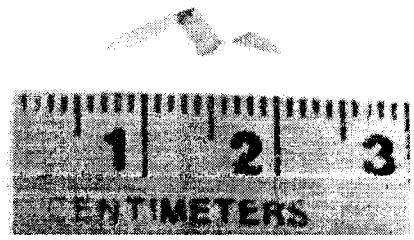

Figure 2.22 Oblique view of hand-bent polycrystalline $Fe_{83}Ga_{17}$ strip, sample R6 produced by the modified Nishihara rolling procedure and additional cold rolling to a 0.17-mm thickness. The 90° bends were cycled several times without failure indicating favorable ductility.

2.3.3 Powder metallurgy

A high degree of <100> crystallographic texture might be developed in polycrystalline specimens utilizing powder metallurgy techniques. The powder metallurgy process includes the consolidation of a particulate parent material followed by sintering to diffusion bond the particles. It was hypothesized that crystallographic texturing would be achieved through the directional application of a saturating applied magnetic field prior to and during the consolidation process. The degree of texturing realized will depend on magnetocrystalline anisotropy, shape induced magnetic anisotropy and contact forces. Provided that spherical single crystal parent material is used, shape anisotropy will be negligible and the torque induced by magnetocrystalline anisotropy should induce the alignment of each particle's [100] easy axis in the applied magnetic field direction. This assumes that contact forces such as friction and cohesion between particles can be overcome to allow particle rotation.

To explore the efficacy of this texturing process, spherical $Fe_{80}Ga_{20}$ powder, with diameters up to 63 μm, was obtained from HJE Co. in Cohoes, NY, who manufactured it by injecting molten alloy into liquid Ar. The powder was sorted into <20, 25-32, 38-45 and 53-63 μm size fractions. Figure 2.23a shows an optical micrograph of the <20-μm size fraction spheres. To evaluate the grain structure of the particles, the various size fractions were separately mounted in epoxy and polished to produce a cross section for optical analysis. Finish polishing with a 1 μm diamond slurry provided a smooth surface in which grains boundaries could be observed after etching with 30% nitric acid in methanol for 15 sec. All size fractions of the powdered Fe-Ga alloy contained a significant number of particles having a dendritic and polycrystalline structure. Since effective magnetic orientation of polycrystalline particles is not possible, the different powder fractions were annealed at 800°C for 4 hr in a furnace backfilled with ultra-high purity Ar. Although the dendritic structure was eliminated, powder fractions above 20 μm were mostly multicrystals. Figure 2.23b shows two 50-μm diameter particles containing several grains each. This annealing process was successful however in converting a significant portion of the <20-μm particles to single crystals as shown in Figure 2.23c.

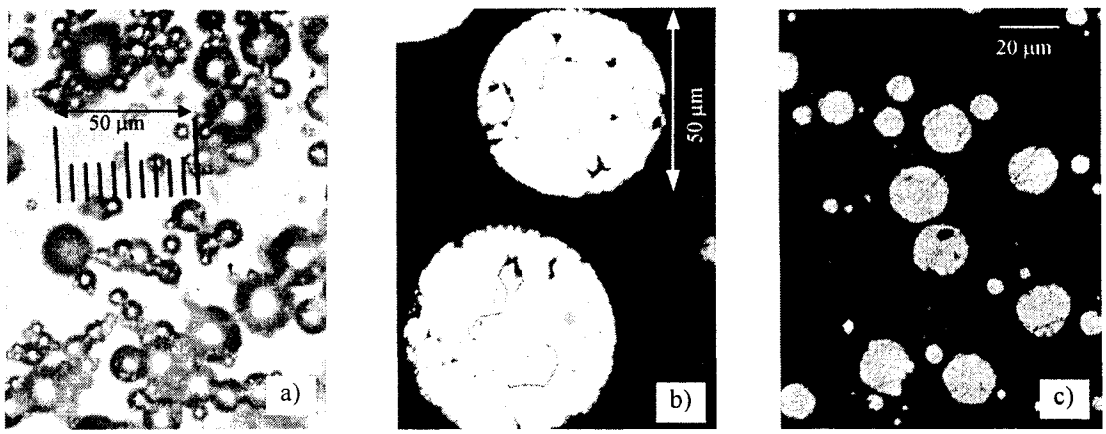

Figure 2.23 Optical micrographs of $Fe_{80}Ga_{20}$ powder. a) Spherical shape of the <20-µm size fraction; b) Cross section of 50-µm particles after 800°C anneal and etch revealing a multicrystal nature; c) Cross section of <20-µm particles after 800°C anneal and etch showing mostly single crystals with polishing artifacts.

After the annealing process was completed, the <20-µm single crystal powder particles were tested for their anisotropic magnetization characteristics. A 50-mg quantity of the powder was suspended in LOCTITE® then subjected to 22 kOe (equivalently 2.2 tesla in air) magnetic field and solidified to form a composite plug. Providing that a single crystal dominates each particle and that the magnetocrystalline anisotropy is adequate, this process should tend to align the [100] easy magnetic axis of each particle in the field alignment direction. A SQUID magnetometer was used to record the room temperature magnetization of the composite plug as a function of applied field intensity for parallel and perpendicular orientations. A plot of the magnetization responses (Figure 2.24) shows that magnetization occurs more rapidly for the parallel specimen, which implies that the previous alignment step had an effect on the particles' orientation. Although not yet confirmed, one expects this magnetic alignment process to form a <100> fiber texture in the powder aggregate, which possesses a random crystallographic orientation about the <100> axis. An additional feature of the plot is that saturation magnetization was not achieved even at 5000 Oe. This is due to the high demagnetization factor for the spherical particles.

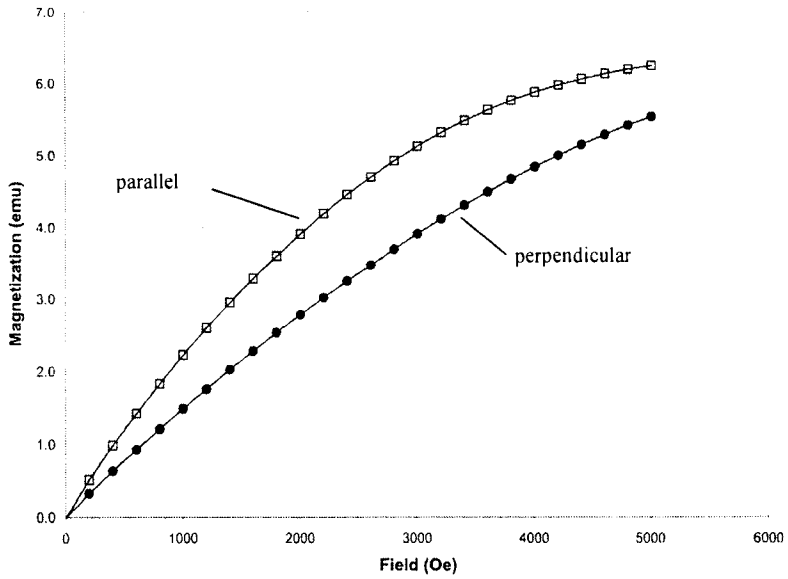

Figure 2.24 Magnetization curves for parallel and perpendicular sample orientations of <20 μm $Fe_{80}Ga_{20}$ powder in a LOCTITE composite plug prepared by magnetic alignment and polymer hardening.

The magnetic anisotropy observed in the magnetization curves of Figure 2.24 suggests that a disk-shaped specimen having some degree of <100> fiber texture (in the plane of the disk) might be formed using the annealed <20-μm powder. To this end, an apparatus was constructed for consolidating the powder, suspended in ethanol, while being vibrated in the directionally applied 22-kOe field of an electromagnet. It was assumed that the ethanol would allow the powder to flow while transmitting vibrational forces that facilitate the spherical powder's free rotation and alignment. The room temperature viscosity of ethanol (1.203 mPa·s) is reasonably low and it does not promote the oxidation of the Fe-Ga alloy as would water. An exploded view of the device from top to bottom (Figure 2.25a) shows a polycarbonate loading cap, alumina plunger with o'ring, polycarbonate cylinder, fritted glass filter, polycarbonate antirotation ring and polycarbonate plug with o'ring and vacuum line nipple. ("Fritted" is a processing term in which glass fibers or particles are bonded to produce an open cell structure with controlled porosity.) To use the device, a 4-μm paper filter was fitted on top of the fritted glass (not shown) then placed in the cylinder with the antirotation ring and the threaded plug to follow. Approximately 2 grams of wetted Fe-Ga powder was loaded into the cylinder from the top followed by a full charge of ethanol. The

plunger was installed in a manner that allowed trapped air to escape from the top. The assembled device (Figure 2.25b) was held in place by a fixture inserted in the 50.8-mm gap of an electromagnet. During the powder alignment process, the plunger was slowly depressed to expel excess ethanol through the filter into the vacuum line while an aluminum stinger transmitted vibrational loads to the cylinder. Note that an excessive vacuum was avoided as it would cause the ethanol to volatilize in the cylinder. After alignment, the entire assembly was inverted and the plug and fritted glass filter were removed. Next the plunger with an "aligned" consolidated powder disk on its end was pushed through the plug end of the cylinder. Upon removal of the paper filter and plunger's o'ring, the alumina plunger and consolidated powder, as a unit, were subjected to the sintering heat treatment. Prior to heating, the furnace was evacuated and backfilled with Ar to prevent oxidation of the powder and loss of Ga. The sintering schedule included ramping up the temperature at 800°C/hr to 1000°C and holding for 2.0 hrs, followed by a power off cooling to room temperature. A typical sintered disk was 12.7 mm in diameter and 1.5-mm thick with a density of 5.9 g/cm^3 or equivalently 74% of fully dense.

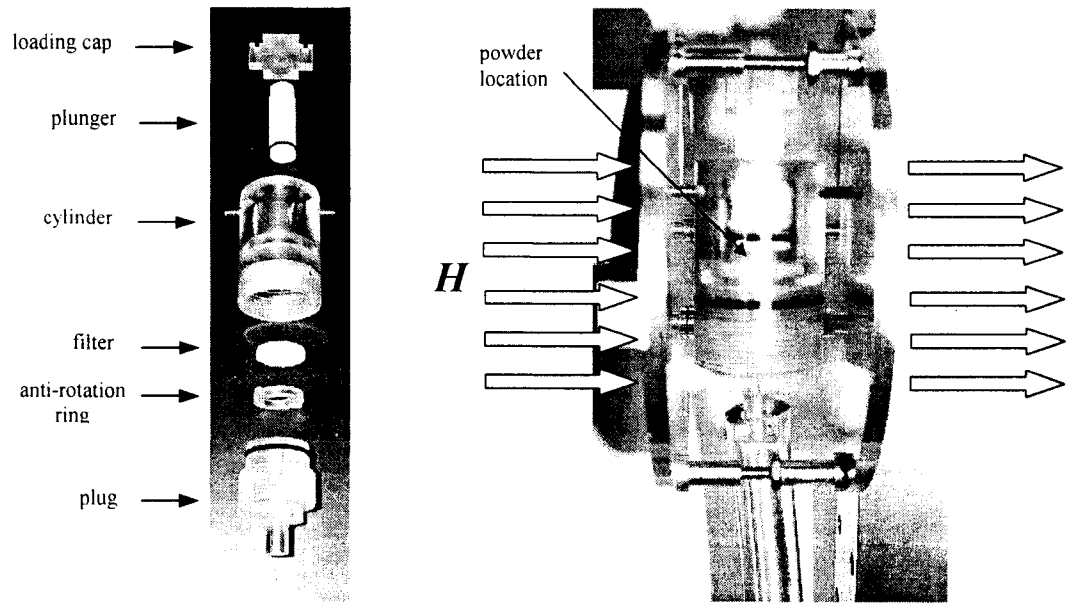

Figure 2.25 Powder alignment device: a) Exploded view; b) Device assembled and installed in mounting fixture between the pole faces of an electromagnet. The direction of the applied field *H* is indicated.

Saturation magnetostriction tests were conducted on three sintered $Fe_{80}Ga_{20}$ powder specimens with finished dimensions of 11.1 mm in diameter and 0.76-mm thick. Two specimens, produced by the magnetic alignment and sintering method just described, yielded variable results. The first of these "aligned" specimens gave $\lambda_{\parallel-\perp} = 60 \times 10^{-6}$ for the three different directions of a 0/45/90° strain gage rosette. The second of these samples gave $\lambda_{\parallel-\perp} = 70 \times 10^{-6}$ for the 0° gage and $\lambda_{\parallel-\perp} = 66 \times 10^{-6}$ for the 45° and 90° gage. The 45° gage corresponded to the field direction during powder alignment in both cases. An additional powder disk specimen having random orientation was produced for comparison. It was neither magnetically aligned nor immersed in ethanol. The sintering process of the random sample was carried out in an alumina crucible and Ar backfilled furnace using a 1.5 hr heat treatment at 900°C followed by furnace cooling. Saturation magnetostriction readings for this specimen gave $\lambda_{\parallel-\perp} \sim 76 \times 10^{-6}$ in each of the directions for a 0/45/90° strain gage rosette. The lack of superior saturation magnetostriction capability of the disks subjected to magnetic alignment over that of the nonaligned (or randomly oriented) sample suggests that either the <100> fiber texture was never developed or that the sintering process disrupted the <100> fiber texture that had formed.

To investigate whether a 2.2 T directional field and the alignment device could develop a significant <100> fiber texture in the Fe-Ga powder prior to sintering, disk specimens were formed using a polyvinylpyrrolidone binder dissolved in the ethanol/powder Fe-Ga mixture. As ethanol was removed during the powder consolidation and alignment process, enough binder remained to produce a stabilized disk. Stereographic projections of the X-ray derived crystal orientation distributions (Figure 2.26) illustrate the textures of three processing conditions which include: a) non-aligned and sintered, b) aligned in polymer binder and c) aligned and sintered. The RD label on the figures indicates the applied field direction (if any) during the alignment process. The ineffectiveness of the magnetic alignment process was substantiated by the fact that no significant development of <200> (and equivalently the <100>) texture in the RD occurred for any of the three processing conditions. Although no conclusions can be made on the effects of sintering on a <100> texture in the RD, the sintering process did have a slight effect on the texture normal to the disk surface. Panels (a) and (c) of Figure 2.26 show a somewhat stronger <200> orientation at the plot's center while

a) Non-aligned and sintered

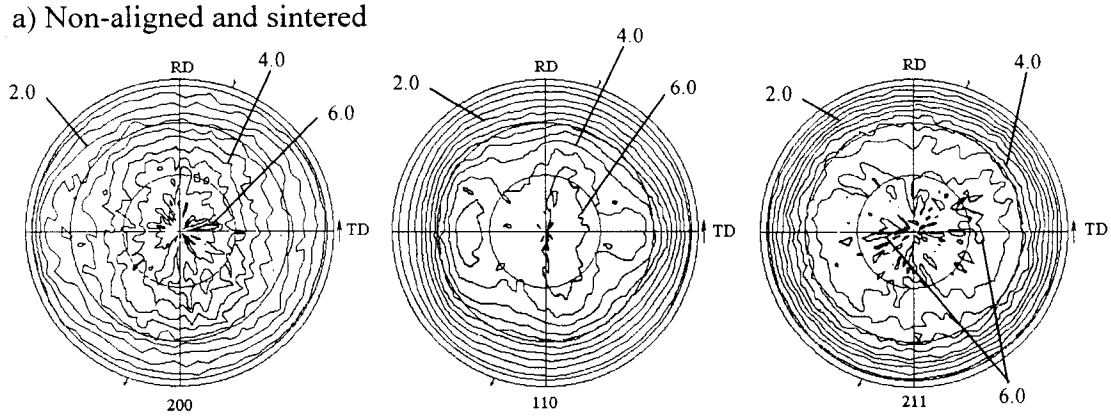

b) Subjected to a 2.2 T magnetic field and consolidated with polymer binder

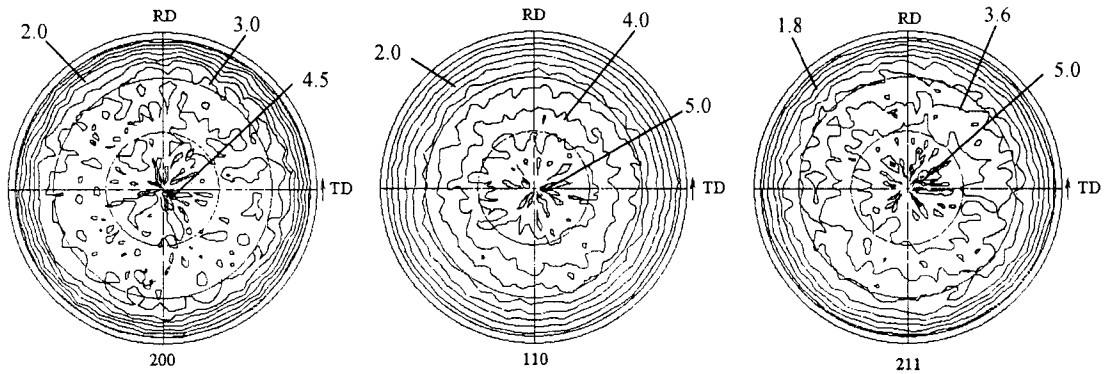

c) Subjected to a 2.2 T magnetic field and sintered

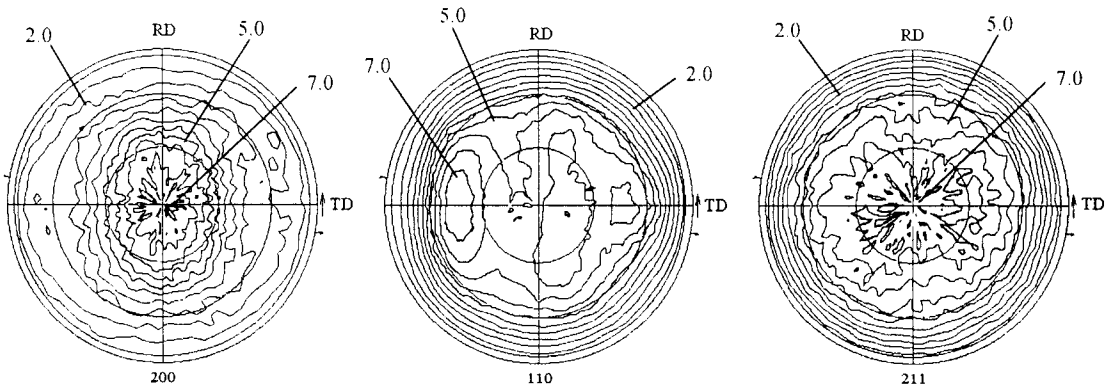

Figure 2.26 X-ray derived stereographic projection of crystallographic orientation for polycrystalline <20 μm $Fe_{80}Ga_{20}$ powder: a) Non-aligned and sintered at 900°C then furnace cooled; b) Magnetically "aligned" in polyvinylpyrrolidone binder; c) Magnetically "aligned" and sintered at 1000°C then furnace cooled.

while a weaker signal occurs for larger angles from the plane normal. Additionally, the <110> projections for the sintered cases show a slight increase in signal return intensity at approximately 45° off of the plane normal. The cause for this weak texturing remains unknown, but it might be related to surface energy effects with the Ar annealing atmosphere similar to that discussed in Section 2.3.2.3 for the rolled material.

Summarizing the magnetically aligned powder Fe-Ga approach, the magnetic anisotropy of each particle did not generate enough torque to rotate the particles into alignment under the processing conditions described, however sintering in Ar has a weak yet measurable texturing effect on a previously random crystallographic orientation distribution.

2.4 Texturing and magnetostriction performance summary

A summary of the saturation magnetostrictive performance for the texturing direction is included in Table 2.1 along with brief comments characterizing processing, texture, grain morphology and mechanical characteristics. Observations made throughout the various texturing processes as well as texture and saturation magnetostriction results lead to the following conclusions:

- Single crystal - Possesses maximum magnetostriction, however Bridgman growth process limits specimen size and yield.
- Directionally solidified - Produces elongated multicrystals with moderate magnetostrictions, but finer grain size is needed to remedy susceptibility intergranular brittle failure.
- Extrusion - Produces material with magnetostrictions comparable to Ni but only $1/5^{th}$ that of a single crystal. A strong <110> wire texture develops along with good ductility.
- Hot forging - Generated low magnetostrictions due to irregular flow patterns and texture. Use of lower aspect ratio forging blanks with larger deformations may improve this situation.
- Cold forging - Weak texture development indicates that larger deformations are needed. A stoichiometric reduction from the 20 at.% Ga content might permit larger deformations without specimen cracking.

- Rolled and recrystallized - Offers the most promise for large-scale production of material having modest magnetostrictions. Much work needs to be done to develop the proper processing technique. Consider additives to affect grain nucleation and possibly refine the grain structure after recrystallization to improve ductility. Note that surface textures are likely to differ from that of the sheet interior due to surface energy effects, roller forces and temperature gradients.
- Cold rolled finish - Resulting texture did not favor good magnetostrictive performance, however the process generates a fine- elongated grain structure with good ductility.
- Magnetically aligned powder - Produced 74% dense material with mediocre magnetostrictive capability. Contact forces appear to be overwhelming the torque generated by magnetic anisotropy to prevent crystallographic alignment. Alignment might be improved by increasing the particle size since larger particles have a larger volume to surface area ratio. However, the particles single-crystal character must be maintained to retain their magnetic anisotropy.

The originally stated objective to produce a textured polycrystalline Fe-Ga alloy that possess a high degree of magnetostrictive capability and good mechanical properties has clearly been difficult to achieve. Although this work has not uncovered an exemplary processing technique it provides some guidance for future work.

Specimen	at.% Ga	Room temperature λ x10^{-6}	Geom-etry	Comments
Single crystal	16.2	(3/2) λ_{100} ~ 285	disk	furnace cooled
Single crystal	19.4	(3/2) λ_{100} ~ 283	disk	furnace cooled
Single crystal	19.0	(3/2) λ_{100} ~ 320	rod	quenched
Directionally solidified	17	(3/2) λ_s ~ 170	rod	multi-crystal with brittle intergranular failure
Extruded	17	(3/2) λ_s ~ 60	rod	stable wire texture, good ductility
Extruded + anneal	17	(3/2) λ_s ~ 30	rod	strengthening of unfavorable texture
Hot forged	17	$\lambda_{\parallel-\perp}$ ~ 18 - 35	disk	complicated flow patterns
Cold forged	17	not tested	particles	incomplete texture development
Rolled - R1	17	$\lambda_{\parallel-\perp}$ ~ 95	disk	Hot rolled only
Rolled - R2	17	$\lambda_{\parallel-\perp}$ ~ 70	disk	warm rolling + high temp. Ar anneal, through thickness grains, brittle
Rolled - R3	17	$\lambda_{RD-\perp}$ ~ 160	disk	warm rolling + high temp. Ar anneal, through thickness grains, brittle
Rolled - R4	17	$\lambda_{RD-\perp}$ ~ 120	disk	warm rolling + high temp. H_2S anneal, through thickness grains, brittle
Rolled - R5	17	$\lambda_{RD-\perp}$ ~ 109	disk	warm rolling + high temp. H_2 anneal, through thickness grains, brittle
Rolled - R6	17	$\lambda_{RD-\perp}$ ~ 30	disk	cold rolling + stress relief anneal, ductile, high strength
Rolled - R7	17	$\lambda_{RD-\perp}$ ~ 30 - 35	disk	cold rolling + stress relief anneal, ductile
Powder	20	$\lambda_{\parallel-\perp}$ ~ 60 -70	disk	aligned and sintered
Powder	20	$\lambda_{\parallel-\perp}$ ~ 76	disk	not aligned and sintered
Powder	20	not tested	disk	aligned with polymer binder

Table 2.1 Summary of Fe-Ga alloy texturing processes with corresponding room temperature saturation magnetostriction and mechanical characteristics. Disk shaped specimens' magnetostriction measured using directional saturating magnetic fields. Rod specimens' magnetostriction measured using a coaxial compressive stress bias and saturating magnetic field.

3. QUASI-STATIC MAGNETIC CHARACTERIZATION

The objective of the work presented in this chapter is characterization of the magnetoelastic properties of single crystal and textured polycrystalline Fe-Ga alloys under controlled mechanical, magnetic and thermal conditions. Single crystal test results will later be used for model development and validation in Chapter 5 as well as providing a baseline data set with which to compare the magnetoelastic response of textured polycrystalline Fe-Ga alloys. These characterization results will also be useful for quantifying the material's strain and force output for transducer applications as well as stress induced magnetization changes for sensing applications. Polycrystalline samples of interest, identified in Chapter 2, include the directionally solidified specimen, which possesses a favorable saturation magnetostriction output, and the extruded specimen, whose magnetostriction properties were significantly reduced by annealing. A brief discussion of the thermally controlled transducer used for the magnetic testing is presented first in Section 3.1. Thereafter, the single crystal response to major loop cyclic magnetic fields under different temperature and stress conditions, as well as its response to minor loop cyclic magnetic fields and major loop cyclic stress is examined in Section 3.2. Next, in Section 3.3 the magnetic and magnetostrictive responses to major-loop cyclic magnetic field conditions are compared for the directionally solidified, extruded and single crystal specimens. The chapter concludes with a magnetic characterization summary of the different Fe-Ga alloys examined.

3.1 Thermally controlled transducer

With the goal of testing rod-shaped Fe-Ga alloys under controlled quasi-static conditions, thermal, magnetic and mechanical operating regimes were considered in the design and operation of the thermally controlled transducer. A schematic (Figure 3.1) highlights the transducer components and their magnetic and mechanical configurations, which are essential to effective specimen characterization. The Fe-Ga rod under study resides at transducer's center. Immediately surrounding the rod is a sense coil (not shown) for detecting the sample's magnetic induction. A Hall Effect chip, which detects the local magnetic field, is located at the midpoint of the rod length and adjacent to the rod's surface.

Exterior to the sense coil and Hall chip is a cooling tube encased solenoid. For this study, the design constraint for thermal control was steady state operation ± 1 °C over range of -21 to + 80 °C while generating magnetic fields up to 258 kA/m (3240 oersted). Thermally regulated fluid was used in the heat exchange tubes to mitigate the effects of ohmic heating produced by the drive solenoid. Minimizing demagnetizing effects of the low aspect ratio sample, annealed low carbon steel end pieces served as interfaces between the sample and the steel transducer housing to form a complete magnetic circuit. The end pieces and output shaft functioned as the load path through which compressive forces up to 3600 N were transmitted to the system through a load cell. A free-hanging weight assembly imposed constant longitudinal compressive loads for the major and minor-loop cyclic magnetic tests, while a hydraulic MTS machine generated variable loads for the major-loop cyclic stress tests. For further design, construction and operational details of the thermally controlled transducer see [Kellogg 2000].

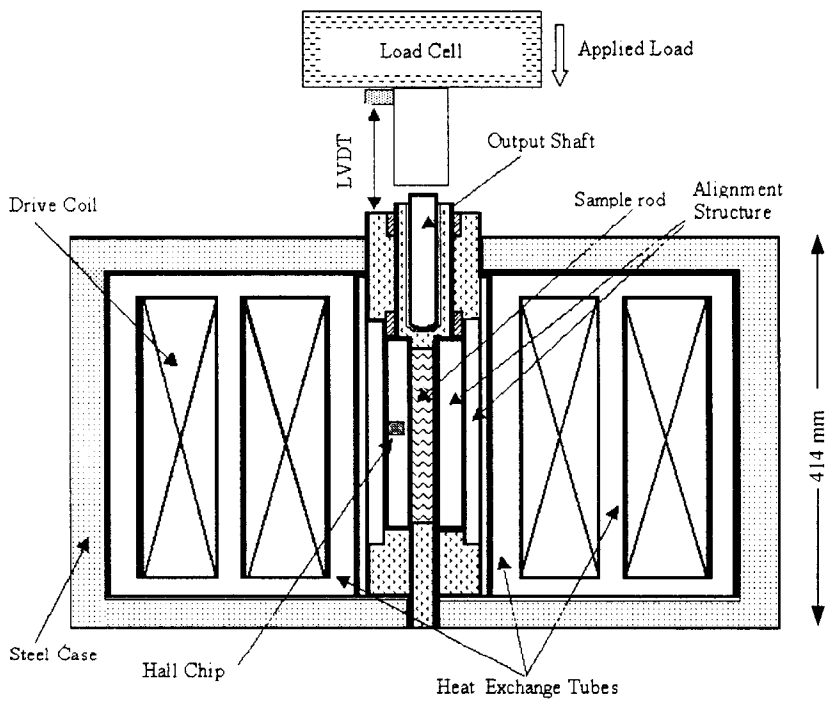

Figure 3.1 Thermally controlled transducer used for measuring the response of Fe-Ga rod-shaped specimens to the quasi-static application of coaxial magnetic fields and compressive stress. The closed magnetic circuit provides a flux return path.

For all test procedures, each specimen's magnetization was recorded using a sense coil and flux meter while the magnetostriction was measured with strain gauges. Two strain gauges were used, each with an active area of 6.1 x 1.9 mm, and were positioned on opposing sides of the rod at mid-length. Throughout specimen testing, data was collected by a computer-controlled system at 50 scans per second. The data recorded includes the magnetic induction, local magnetic field, solenoid current, load and longitudinal strain.

3.2 Single crystal

The single crystal $Fe_{81.0}Ga_{19.0}$ rod (6.35-mm diameter by 23.7-mm long) used for this study was extracted from a single-crystal ingot grown at 2 mm/hour using the modified Bridgman technique. The ingot was annealed at 1000°C for 168 hours and afterward water quenched from 800°C to obtain a nearly random Ga distribution throughout the crystal lattice. Using back reflection Laue diffraction, the rod was oriented and sectioned from the ingot with a [100] crystal axis aligned within 0.5° of the rod's longitudinal axis.

3.2.1 Major-loop cyclic magnetic field

The magnetization and magnetostrictive response of the single crystal was measured under quasi-static 0.05-Hz 800-Oe amplitude sinusoidal applied magnetic field conditions. Testing was conducted for constant compressive stress conditions including 14.4, 45.3 and 87.1 MPa and constant temperatures ranging from -21°C to +80°C. For each combination of stress and temperature examined, the sample was stabilized at the desired temperature and stress level then demagnetized over 240 cycles using a 1.0 Hz sinusoidal field, which underwent a 5% geometric decay every 1.5 cycles from an initial amplitude of 1600 Oe. The acquired data provided characterization of the material's permeability, magnetization and magnetostriction as a function of applied magnetic field, compressive stress and temperature.

3.2.1.1 Stress effects

Figure 3.2 shows the magnetostriction and magnetization developed due to an applied magnetic field for temperatures of 22°C and 80°C. This figure highlights the effect of stress on the Fe-Ga alloy's magnetomechanical response. As the magnitude of compressive stress is

increased, attaining equivalent levels of magnetostriction requires larger applied magnetic fields. The 14.4 MPa stress condition exhibits less strain for applied fields above 300 Oe as this stress is too low to provide complete pre-alignment of magnetic moments along <100> easy axes perpendicular to the rod's longitudinal axis. The maximum magnetostriction obtained at 22°C (near maximum magnetization with an applied field of 800 Oe) was 306 $x10^{-6}$ for the 14.4 MPa stress condition and 322 $x10^{-6}$ for both the 45.3 MPa and 87.1 MPa stress conditions. The maximum magnetostriction obtained at 80°C was 273 $x10^{-6}$ for the 14.4 MPa stress condition and 298 $x10^{-6}$ for both the 45.3 MPa and 87.1 MPa stress conditions. Notably, 95% or more of the maximum strain for each stress level was developed with applied fields of 400 Oe or less. Figure 3.2 also demonstrates that for all load cases with fields of less than 300 Oe the magnetization reaches 95% or more of the maximum magnetization of 1295 and 1265 kA/m at 800 Oe respectively for 22°C and 80°C. Below 200 Oe the decreasing slope of the magnetization versus applied field curve indicates that

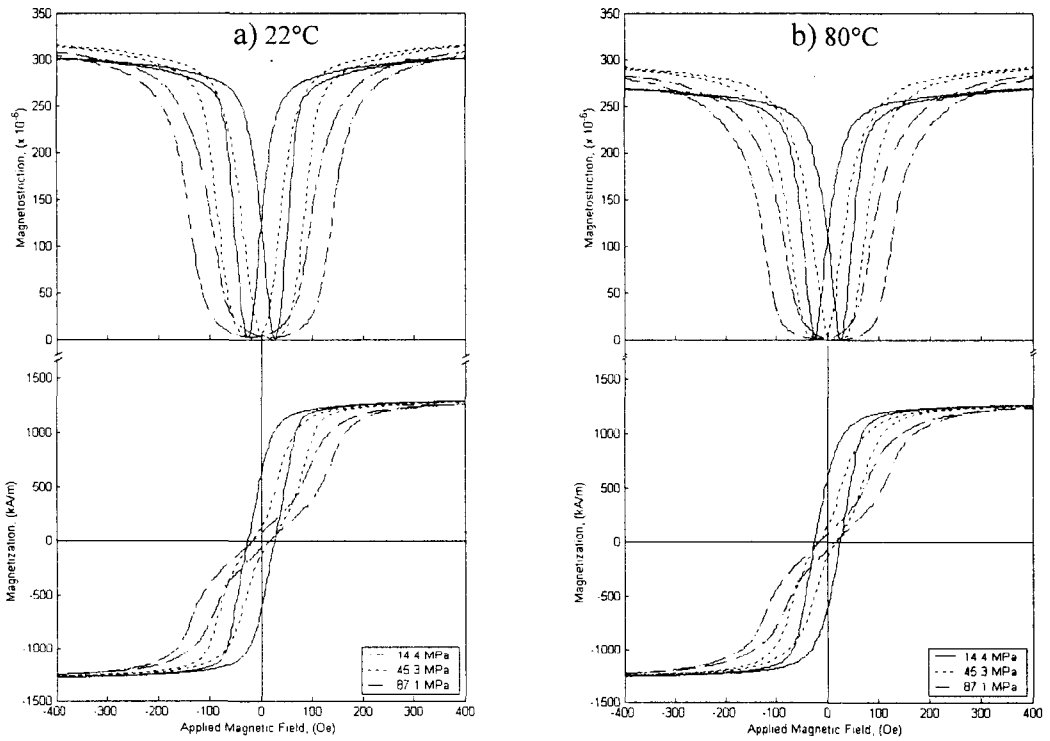

Figure 3.2 Applied magnetic field dependencies of the magnetostriction and magnetization of $Fe_{81.0}Ga_{19.0}$ for various compressive stresses: a) at 22°C; b) at 80°C. All measurements were made at 0.05 Hz.

increasing stress levels reduce the permeability. Measured near the coercive field for both temperature conditions, the relative permeability decreases 6-fold from μ_r ~360 to μ_r ~60 for the 14.4 MPa and 87.1 MPa stress conditions respectively. At higher applied field levels, near the burst region of the response that is typically used in AC actuation applications, the permeability also decreases with increasing bias stress but to a lesser extent than that observed near H_c. The hysteresis in the magnetostriction and magnetization plots of Figure 3.2 occurs for two primary reasons. The sample experiences domain wall pinning due to crystal defects and the transducer itself generates a 12 Oe hysteresis in the applied magnetic field due to remanence of the steel flux-return path.

Figure 3.3 provides some insight into the sample's magnetization process. Here, the magnetostriction is shown as a function of the magnetization squared for three compressive stress levels at 22°C. Assuming sufficient stress to dominate the magnetostriction process and to align all the magnetic moments with the <100> easy axes perpendicular to the rod's longitudinal axis at zero field, one would expect the theoretical linear plot indicated. This follows from the relationship $\lambda = (3/2)\lambda_s(M/M_s)^2$, which describes the magnetostriction λ generated by the magnetization M where λ_s and M_s are the conventional saturation magnetostriction and magnetization values respectively [Cullity 1972]. This relationship assumes that the magnetization proceeds by moment rotation from the perpendicular <100> easy axes into the [100] easy axis parallel to the rod's longitudinal axis. The slope of the

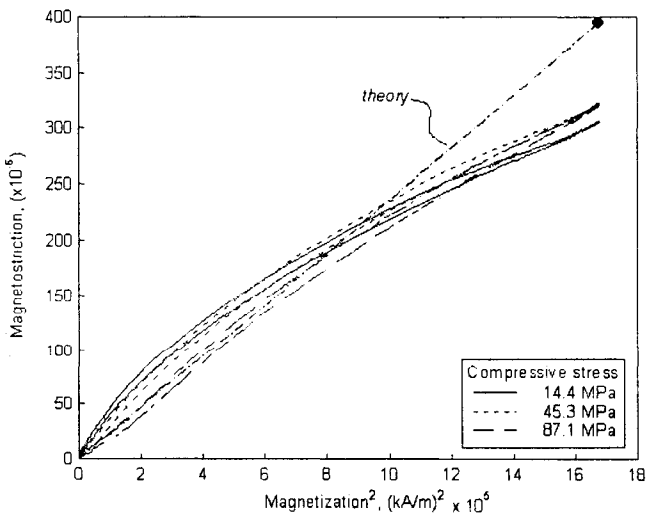

Figure 3.3 Magnetization squared dependencies of the magnetostriction of $Fe_{81.0}Ga_{19.0}$ at 22°C for three compressive stresses.

theoretical trace is based on values of $(3/2)\lambda_s$ = 395 ppm (determined at room temperature by orthogonal saturating applied fields) and M_s = 1313 kA/m that were previously measured by Clark *et al.* using a (010) disk cut from the same Fe-Ga alloy ingot used in this study [Clark 2001b]. The fact that the experimental traces of Figure 3.3 are nonlinear indicates that the stress anisotropy generated by these compressive stresses were insufficient to cause the magnetization processes to occur solely by 90° moment rotation even at 87.1 MPa. Additionally, the maximum λ values for both the 45.3 MPa and 87.1 MPa stress conditions at this temperature were identically 320 $x10^{-6}$, which suggests that the $(3/2)\lambda_s$ value of 395 $x10^{-6}$ may be unattainable even with further increases in compressive stress. Lower values of maximum λ have been observed in other rod-shaped specimens (tested under compressive stress) compared to disk shaped-specimens of identical stoichiometry (measured with orthogonal saturating fields). This may be due in part to complex domain structures in the stressed rod-shaped specimens.

It is anticipated that the maximum magnetostrictive capability of the Fe-Ga alloys, observed at modest compressive stresses (45.3 MPa for example), will be retained to higher stress levels (perhaps 400 MPa or more) and will be limited only by the material's yield stress. However, achieving the maximum magnetostriction at high stress will require applied fields significantly higher than the 1000 Oe field levels used for this study. Should an Fe-Ga alloy undergo stresses large enough to produce yield deformation, its post-yield magnetostrictive capability should reflect the degree of alteration in its crystallographic texture. Residual internal stresses, retained after a yielding event, may also influence the material's maximum magnetostrictive capability.

3.2.1.2 Temperature effects

The effects of temperature on the relationship of magnetostriction and magnetization versus applied magnetic field were measured for the 45.3 MPa compressive stress condition. Figure 3.4a illustrates that the magnetization exhibits only a small reduction with increasing temperature. Likewise, the magnetostriction experiences only a small reduction with increasing temperature for applied fields above 100 Oe. The small and consistent nature of the temperature dependencies suggests that no anomalous changes in the anisotropy

constants K_1 or K_2 or the magnetostriction constants λ_{100} or λ_{111} are occurring. Figure 3.4b shows the maximum magnetostriction and magnetization values at an 800 Oe applied field and 45.3 MPa stress as a function of temperature. The maximum magnetostriction declines 12% from 340 $x10^{-6}$ at -21°C to 298 $x10^{-6}$ at 80°C. Similarly the maximum magnetization declines 3% from 1313 kA/m to 1265 kA/m. These temperature dependencies of maximum magnetostriction and magnetization are consistent with the trends observed up to 27°C for $Fe_{83}Ga_{17}$ [Clark 2000c] and $Fe_{82}Ga_{18}$ [Kawamiya 1972]. Magnetization and magnetostriction responses to applied field (similar to Figure 3.4a) for other compressive stress conditions up to 87.1 MPa and temperatures between -21 and 80 °C are given in Appendix B.

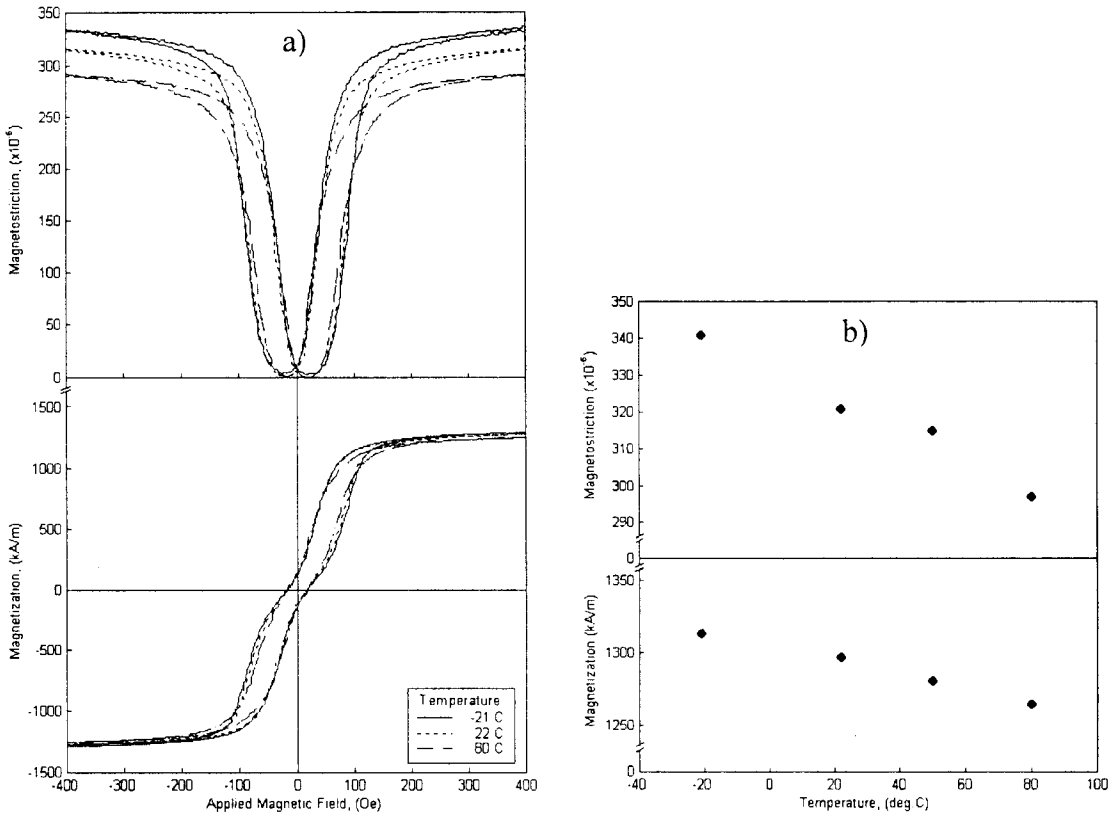

Figure 3.4 Temperature dependencies of the magnetostriction and magnetization of $Fe_{81.0}Ga_{19.0}$ for a 45.3 MPa compressive stress: a) Applied magnetic field response for three temperatures; b) Maximum magnetostriction and magnetization values for an 800-Oe applied field. All measurements were made at 0.05 Hz.

To supplement the knowledge of the magnetic and magnetostrictive properties of Fe-Ga alloys, the value of Young's modulus of a $Fe_{81.0}Ga_{19.0}$ single crystal rod was measured. The sample's strain (in a demagnetized state at each stress level) was obtained over a 7.2 to 87.1 MPa compressive stress range for temperatures of -21, 22 and 80 ° (Figure 3.5). Note that the initial strain levels at -7.2 MPa were similar, so an arbitrary offset was used to allow viewing of the trend without overlaying the data. Calculations of the slope for the 21 to 87.1 MPa compressive stress range (region of best linearity) reveal that the modulus is nearly temperature independent with a value of 56.6 ± 0.3 GPa. This modulus is lower than the high stress low field value of ~77 GPa reported for single crystal $Fe_{85}Ga_{15}$ [Clark 2000c].

Kawamiya *et al.* has measured the coefficient of thermal expansion for BCC Fe_3Ga (Fe- 27 to 29 at.% Ga from Figure 1.4) over a 300-800 K temperature range and found that $\alpha = 12.4 \times 10^{-6}$. In addition, the room temperature lattice parameter (i.e. atomic spacing along a crystallographic axis) was experimentally determined to be 2.095×10^{-10}m [Kawamiya 1972].

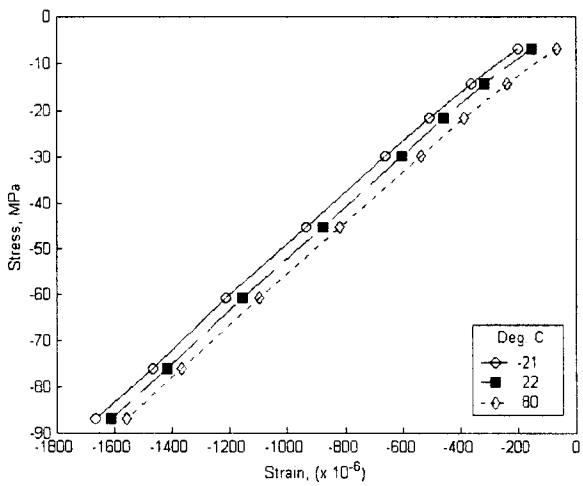

Figure 3.5 $Fe_{81.0}Ga_{19.0}$ single crystal static stress-strain relationship for three different temperatures. Each data point was collected after the specimen was demagnetized under the static load. Initial strain levels are arbitrary.

3.2.2 Minor loop cyclic magnetic field

The magnetostrictive response of the $Fe_{81.0}Ga_{19.0}$ single crystal rod was measured under quasi-static (0.05 Hz) minor-loop sinusoidal applied magnetic field conditions at room temperature using the thermally controlled transducer. Prior to each test, the sample was

demagnetized using a 1.0-Hz, 5% geometrically decaying sinusoidal field to generate a consistent initial magnetic state. The initial magnetic field application included a sinusoidal increase to a DC bias field followed by sinusoidal field oscillation about that DC bias level. To provide the maximum range of an approximate linear magnetostrictive response, the magnetic DC bias level and minor loop amplitude were optimized for each compressive stress level. Tests were conducted at 14.4, 29.8 and 60.7 MPa compressive stress conditions with loads produced by a free-hanging weight assembly. The magnetostriction as a function of internal magnetic field (i.e. the Hall chip reading, which is equivalent to the applied field - demagnetizing fields) is shown in Figure 3.6 for the three stress levels. As compressive stress increases, the DC magnetic field bias must also be increased to maintain the best linear response. Considering the 60.7 MPa stress condition as an example, a 30 Oe AC field superimposed on a DC 150 Oe field yields approximately a peak to peak 200 $x10^{-6}$ strain capability. In this case the piezomagnetic parameter d_{33}, which was previously addressed in Equation 1.5a, is approximately 36 $x10^{-9}$. The piezomagnetic parameter improves for the lower-magnitude bias-stress conditions where d_{33} is 50 $x10^{-9}$ and 60 $x10^{-9}$ for the 29.8 MPa and 14.4 MPa conditions respectively. For all stress levels examined, the hysteresis is low (~2 Oe). This indicates that the energy loss/cycle is low for this quasi-static excitation field.

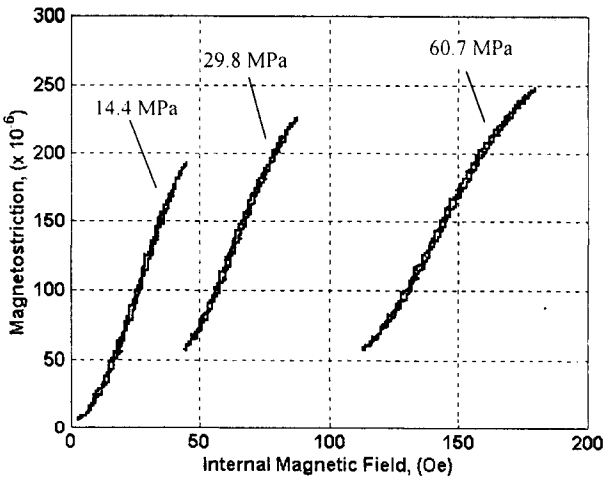

Figure 3.6 Quasi-static minor-loop cyclic magnetostrictive response of $Fe_{81.0}Ga_{19.0}$ single crystal rod for three constant compressive stress levels collected at room temperature.

However, it should be noted that eddy current losses will likely become a significant loss mechanism as the operating frequency is increased, because of the finite resistivity of the material. The resistivity of disordered $Fe_{1-x}Ga_x$ where $13 \leq x \leq 19$ has not been measured, however Kawamiya *et al.* have reported the room temperature resistivity of $Fe_{72}Ga_{28}$, which has an ordered Fe_3Ga structure, to be ~70 μΩ·cm [Kawamiya 1972]. The resistivity of the disordered Fe-Ga alloys will likely vary from this result, but the value for $Fe_{72}Ga_{28}$ is anticipated to provide a reference point at least within an order of magnitude.

3.2.3 Major-loop cyclic stress

Major-loop cyclic compressive stress testing of the $Fe_{81.0}Ga_{19.0}$ single crystal rod was conducted at room temperature using the thermally controlled transducer and a hydraulic MTS machine. Strain, magnetic induction and applied magnetic field data were recorded while the sample was linearly stress cycled in compression from 0 to 115 MPa and back. The test procedure consisted of three processes. First, the specimen was demagnetized under zero load over 240 cycles using a 1.0-Hz, sinusoidal field undergoing a 5% geometric decay every 1.5 cycles from an initial amplitude of 1600 Oe. This demagnetization process was used to bring the Fe-Ga alloy sample to a reproducible demagnetized state prior to the start of each cyclic compression test. Second, a DC magnetic field, up to 891 Oe, was applied by linearly increasing the applied field from zero to the final value at a rate of 40 Oe/second. Finally, while recording data, the specimen was compressed and uncompressed at 2 MPa/second using the MTS machine in feedback load-control mode.

Repetition of the demagnetization, magnetic field application and cyclic compression steps for various levels of DC applied magnetic field produced a thorough characterization of the crystal's strain and magnetization response. The combined test results for various applied field levels are shown in Figures 3.7a and 3.7b where magnetization or equivalently material induction J (where $J = B\text{-}\mu_o H = \mu_o M$) and strain are plotted against stress. At the beginning of each test, near zero stress, the initial magnetization and magnetostrictive strain levels are those arising from field-induced changes from the demagnetized state. With increasing levels of the applied field, the magnetization and magnetostriction values increase and approach their saturation values. These initial magnetization and strain values could be plotted against

the applied field to give the initial responses (for a zero load condition) similar to that of Figure 3.2. Tracking each curve's response to cyclic stress, the magnetization and strain loops are hysteretic, thus indicating an energy loss occurring over the compression and decompression cycle. Compared to conventional metals, the overall hysteresis is larger due to the coupling of mechanical and magnetic energy states. Energy losses arise during the magnetization changes are due to irreversible processes such as domain wall pinning. The stress induced hysteretic losses of this Fe-Ga alloy are significantly smaller than those observed for giant magnetostrictive materials such as Terfenol-D [Kellogg 2000]. Notably, the hysteresis is lowest for the curves where mechanical processes dominate the response to stress. This occurs for the extreme applied field conditions of zero and 891 Oe where magnetic moment rotations are limited. In the former case, compressive stress quickly pins the magnetic moment to the <100> easy axes perpendicular to the longitudinal axis. In the latter case, the magnetic moments are held in rigid alignment parallel to the rod's longitudinal axis by the applied field. In both situations limited changes in magnetization with stress minimize the hysteresis.

The slopes of the magnetic induction curves reflect the rate of change of magnetization with respect to stress. For constant levels of applied magnetic field, the differential $\Delta J/\Delta\sigma$ approximates this slope to yield the piezomagnetic parameter d^*_{33}, which was previously addressed in Equation 1.5b. The values of d^*_{33} are plotted against stress (Figure 3.7c) for the compression portion of the cyclic stress test. As the level of DC applied field increases, for values above 22.3 Oe, the peak values of d^*_{33} decrease while the peak locations occur at increasing magnitudes of compressive stress. The lower d^*_{33} peak values reflect a wider distribution in stress of moment rotation while the various peak locations reflect a changing balance between the material's magnetic and mechanical energy states. Sensor applications that detect stress changes using magnetomechanical coupling could maximize sensitivity (i.e. maximize d^*_{33}) by using an optimal DC magnetic field for an anticipated level of bias stress.

An additional feature of interest in Figure 3.7b is how the slope of the strain curves with respect to stress vary with the different levels of applied magnetic field. In this case, the slope gives the material's compliance S^H with the inverse ratio providing the material's

Young's modulus of elasticity E_Y^H, which is plotted in Figure 3.7c. As used in Equation 1.7, the superscript "H" implies compliance and modulus values evaluated at a constant applied magnetic field. Larger slope values correspond to an increase in compliance and likewise a decrease in the modulus of elasticity. The elastic modulus for a given applied magnetic field and stress state is a result of the interplay between the mechanical and magnetic energy regimes. Considering the strain curves for the extreme applied field conditions, the response of the zero-field case is dominated by mechanical effects for stresses more negative than -40 MPa, and the response of the 891 Oe case is dominated by mechanical effects at least up to the -115 MPa stress level tested. As was mentioned when discussing hysteresis, magnetic moment rotation is constrained under both of these extreme conditions. For intermediate levels of applied field, the traces transition through a region of low elastic modulus then asymptotically approach the strain-stress line for the zero applied field case (bottom left). Increasing applied field levels delay the onset of lower modulus values to larger magnitude

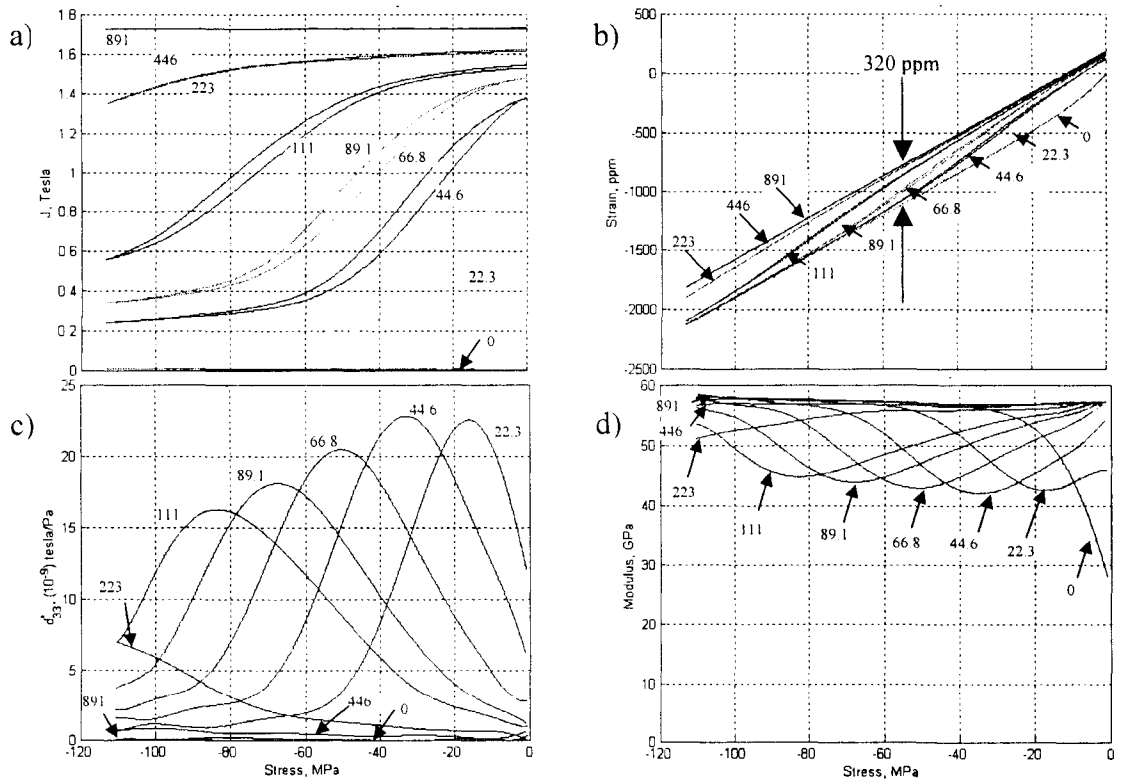

Figure 3.7 $Fe_{81.0}Ga_{19.0}$ quenched single-crystal major loop cyclic stress response for DC applied magnetic fields (based on solenoid current) of 0, 22.3, 44.6, 66.8, 89.1, 111, 223, 446 and 891 Oe: a) Material induction; b) Strain; c) Piezomagnetic parameter d^*_{33}; d) Young's modulus.

compressive stress values. An evaluation of the strain-stress curve slopes shows that high fields and hence constant induction conditions, gave a magnetically saturated elastic modulus of E_s = 57 GPa, which was observed at all stress levels. For the zero field case, in the initial or demagnetized state, the elastic modulus at low stress was E_o = 28 GPa and the modulus at high stress was E_o = 57 GPa. The measured delta-E effect at low stress is $(E_s\text{-}E_o)/E_o$ = 104%.

A final point of interest for the strain-stress response is the difference in strain values for the zero and 891 Oe applied fields at constant stress levels less than -40 MPa. Under these conditions of maximal magnetic moment rotation the strain difference is ~320 $x10^{-6}$, which is approximately equivalent to the room temperature saturation magnetostriction capability of the specimen given in Figure 3.4b.

3.3 Polycrystalline magnetic response

The quasi-static magnetization and magnetostriction responses of several polycrystalline $Fe_{81}Ga_{17}$ alloy rod-shaped specimens were investigated to better understand their magnetic processes and determine their suitability as actuation elements. These specimens include the directionally solidified, extruded and extruded plus annealed textured materials produced by the methods described in Chapter 2. The room temperature response to a 0.05-Hz sinusoidal applied magnetic field, having an amplitude of 900 Oe, was recorded for the 28.1 MPa constant compressive stress conditions using the thermally controlled transducer and free-hanging weight assembly.

Figure 3.8 shows the results for these three polycrystalline specimens along with the $Fe_{81.0}Ga_{19.0}$ single crystal response for comparison. The first column of the figure illustrates each sample's magnetization characteristics as a function of applied magnetic field. The Fe-19Ga single crystal saturates at ~1300 kA/m compared to a ~1400 kA/m value for the Fe-17Ga polycrystalline samples. This increase in saturation magnetization is consistent with a reduction in the content of non-magnetic Ga [Kawamiya 1972]. The magnetization curves of the single crystal and directionally solidified specimens are nearly identical, however, the extruded and extruded plus annealed specimens are increasingly difficult to magnetize. This magnetization difficulty is indicated by the increasingly rounded approach to the final saturation magnetization level. Recalling the magnetization curves for cubic Fe in Figure 1.3,

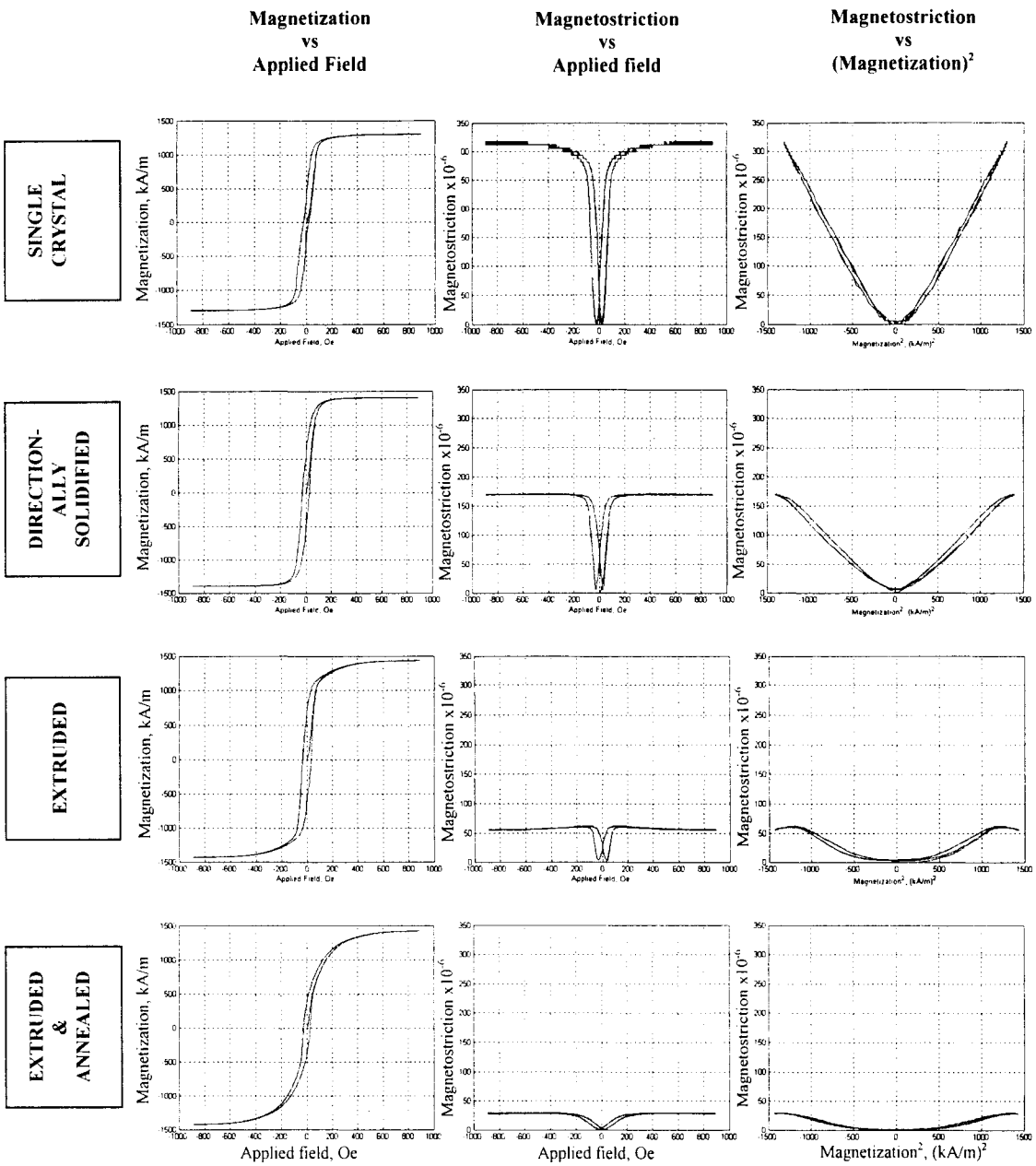

Figure 3.8 Comparison of magnetostriction and magnetization responses to applied magnetic field under a 28.1 MPa compressive stress for $Fe_{81.0}Ga_{19.0}$ quenched single crystal, $Fe_{81}Ga_{17}$ directionally solidified, $Fe_{81}Ga_{17}$ extruded, and $Fe_{81}Ga_{17}$ extruded plus annealed specimens.

the material becomes increasingly difficult to magnetize going from <100> to <110> and finally <111> crystallographic textures due to magnetocrystalline anisotropy. Comparing the extruded and extruded plus annealed specimens, the magnetization response suggests that annealing may have induced an increase in the <111> texture component.

The second column of Figure 3.8 presents the magnetostriction as a function of applied magnetic field. The quenched Fe-19Ga single crystal generates the maximum output at 320 $x10^{-6}$, with its near perfect <100> texture, compared to values of 170 $x10^{-6}$, 60 $x10^{-6}$ and 30 $x10^{-6}$ for the polycrystalline Fe-17Ga directionally solidified, extruded and extruded plus annealed specimens respectively. This trend in decreasing magnetostrictive output reflects an increasing deviation from the ideal <100> texture. The magnetostrictive micromechanics model of Chapter 5 will address these magnetostriction texture dependencies in more detail.

The final column of Figure 3.8 reveals that the magnetostriction and magnetization relationship varies depending upon the method of processing and ultimately the degree and type of crystallographic texture. As presented for the single crystal in Section 3.2.1.1, theory suggests that the magnetostriction will be proportional to the magnetization squared. Therefore, if the goal of a high degree of <100> texturing had been achieved, the plots should increase linearly with variation of the ordinate value of M^2. Although the single crystal is fairly linear beyond the initial magnetization phase at 400 $(kA/m)^2$, the extruded and polycrystalline specimens' responses deviate substantially from linearity. Given the presence of the crystallographic grain misorientations revealed in the texture analysis of Figures 2.5, 2.7 and 2.8, such deviations were not altogether unanticipated.

3.4 Magnetic characterization summary

The $Fe_{81.0}Ga_{19.0}$ single crystal's magnetic response under broad temperature and stress conditions is well behaved. The applied magnetic fields required to develop most of the measured maximum magnetization and magnetostriction at each constant-temperature level are low; only 400 Oe is needed for compressive stresses up to 87.1 MPa. Surprisingly, the stress of 87.1 MPa proved insufficient to cause magnetization processes to occur exclusively by 90° moment rotations. Constant temperature tests showed that compressive stresses

greater than 14.4 MPa were needed to achieve the maximum magnetostriction. Over the -21°C to 80°C temperature range examined, the maximum magnetostriction and magnetization results decreased monotonically by 12% and 3% with increasing temperature from their respective maximum values of 340 $x10^{-6}$ and 1313 kA/m at -21°C. This small magnetostrictive decrease is consistent with a correspondingly small 3.6 % decrease in magnetization over the same temperature range (recall that magnetostriction is proportional to magnetization squared). No anomalous responses were found. The Young's modulus of the demagnetized sample was nearly temperature insensitive over the -21°C to 80°C range with a value of ~ 55 ± 1 GPa.

The room temperature quasi-static minor-loop cyclic magnetic field tests established that the $Fe_{81.0}Ga_{19.0}$ single crystal can generate magnetostrictions of ~ 200 $x10^{-6}$ with good linearity for compressive stresses up to 87.1 MPa. The applied magnetic field inputs required for this performance were a 30 Oe amplitude AC field superimposed on a bias field of 150 Oe. Transduction efficiencies should be favorable for this material as the observed hysteresis was small, with only a 2 Oe loop width detected using the Hall chip. Operating losses in activation applications may vary from this result however, due to differences in transducer efficiencies arising from hysteresis in the transducer solenoid and flux-return path itself.

Major-loop cyclic stress testing demonstrated that the $Fe_{81.0}Ga_{19.0}$ single crystal's maximum delta-E effect is 104% with a stiff modulus of 57 GPa coinciding with limited magnetic moment rotation and a soft modulus of 28 GPa coinciding with maximum magnetic moment rotation. In addition, the hysteresis developed over a stress cycle was dependent on the stress and applied magnetic field. Maximum hysteresis is produced when magnetic moment rotation is abundant and energy is dissipated through domain wall motion and through pinning sites. Stress induced magnetization changes gave a maximum sensitivity of d^*_{33} = 22.5 $x10^{-9}$ tesla/Pa over a 20 MPa stress range. Optimizing this sensitivity for sensing applications will require the proper choice of combined DC applied magnetic field and stress. Finally, the difference between the strain values for the saturating and zero applied magnetic fields (at any stress level less that -20 MPa) reflects the maximum magnetostriction capability of the material. In this case that was ~ 320 $x10^{-6}$.

The room temperature quasi-static major-loop cyclic magnetic field tests of the polycrystalline samples showed that the directionally solidified magnetization response was very similar to that of the single crystal. However, the extruded and extruded plus annealed specimens exhibited greater magnetic anisotropy due to the presence of misoriented grains having magnetically hard axes in the direction of the applied magnetic field. These unfavorable grain orientations likely include <110> and <111> texture components. Magnetization trends were corroborated by the magnetostriction measurements whose values were 170 $x10^{-6}$, 60 $x10^{-6}$ and 30 $x10^{-6}$ for the polycrystalline Fe-17Ga directionally solidified, extruded and extruded plus annealed specimens respectively. Unfortunately, the polycrystalline materials' magnetostriction capability falls far short of the 320 $x10^{-6}$ value observed for a <100> oriented single crystal.

Despite the limited magnetostriction of the polycrystalline specimens developed to date, the large magnetostriction of single crystals, high permeability and temperature insensitivity combined with previously observed robust mechanical properties make Fe-Ga alloys an attractive material for sensing applications as well as transducer, active vibration control and damping applications where the material is employed as an active structural material.

4. QUASI-STATIC MECHANICAL CHARACTERIZATION

Quasi-static characterization of the Fe-Ga alloys was undertaken to advance the understanding of their mechanical characteristics and aid in their development as robust actuator/sensing materials. There are several specific motivations for studying the alloy's mechanical properties. First, knowledge of its deformation mechanisms would be useful in modeling the evolution of crystallographic texture throughout deformation processing. This information in turn could be used to impart a specific desired crystallographic texture in polycrystalline forms of the alloy in order to optimize their magnetostrictive performance. The marginal magnetostriction performance achieved so far in the extruded, rolled and forged specimens, described in Chapter 2, clearly indicates the need for additional information. Second, the possible challenges in using this material to form novel engineering components with favorable structural characteristics in addition to the magnetically active capability requires knowledge of its elastic properties and strength. Lastly, knowledge of the alloy's elastic properties will provide fundamental information for understanding and predicting the magnetostriction capability of polycrystalline alloy forms through the implementation of a magnetostrictive micromechanics model to be developed in Chapter 5.

To determine the alloy's active slip systems, critical resolved shear stresses, elastic moduli, and Poisson's ratios, the responses to uniaxial tensile loading were studied in $Fe_{83}Ga_{17}$ single crystal and polycrystalline rolled materials. In section 4.1, single-crystal specimen preparation, crystallographic orientations and the tensile testing methodology are reviewed. The plastic regime of the tensile testing results are utilized to analyze the plastic deformation responses including slip line angles, stress levels and elongations. Subsequent analysis of the tensile test results focus on the linear portion of the stress-strain response to quantify the specimens' elastic properties. Next in Section 4.2, comparisons of the Fe-Ga plastic and elastic characteristics are made to other alloy systems. The well established deformation processing methods for transformer steels (Fe-Si) to realize cube {100}<001> and the Goss {110}<100> textures and the similarity of Fe-Al alloys system to Fe-Ga alloys makes comparisons of their active slip systems and critically resolved shear stresses instructive. Thereafter, the elasticity results from this study are compared to those of other

Fe-Ga alloy stoichiometries to provide an overview of the materials' elastic anisotropy and auxetic behavior. Section 4.3 presents additional information, where the tensile properties of a cold rolled $Fe_{83}Ga_{17}$ polycrystalline specimen are examined to provide an indication of the alloy's structural potential. Closing out the chapter, section 4.4 summarizes the mechanical properties of single and polycrystal specimens.

4.1 Tension testing of Fe-17Ga single crystal

BCC metals exhibit a high degree of anisotropy in their mechanical characteristics due to the directional dependence in the atomic packing density. Recalling the directionally dependent properties of high purity α-Fe single crystal (discussed in section 1.4.2 and 1.4.3), Young's modulus can vary by a factor of more than two and certain slip systems such as the {110}<111> are highly favored. With these types of mechanical anisotropic effects in mind, tension tests of a Fe-17Ga alloy were designed to utilize single crystals having specific crystallographic orientations. The choice of these orientations was dictated by the need for clear simple results, which was ultimately guided by the elastic analysis of section 1.5.2. Preparation of these oriented single crystals is discussed first, followed by the testing process and analysis of the ensuing plastic and elastic responses.

4.1.1 Materials preparation

A single crystal of $Fe_{83}Ga_{17}$ was grown using the modified Bridgman technique, annealed and furnace cooled using the same techniques as described in section 2.2.1. The resulting crystal was confirmed to possess a single-phase, fully disordered α-Fe structure with a random Ga distribution.

The single crystal's orientation was next determined within 0.25° using Laue X-ray back reflection analysis and then cut into tensile specimens by electro-discharge machining. After machining, the orientation of each specimen was again checked by Laue X-ray back reflection analysis. The major and minor faces of the specimens' gauge length were polished with progressively finer wetted silicon carbide paper to 800 grit and finished with 1-μm diamond paste in an oil suspension to provide a smooth surface for slip line observation.

4.1.2 Tensile testing procedures

Four single crystal tensile specimens of $Fe_{83}Ga_{17}$ were tested. Two were cut with the [110] direction parallel to the tensile axis. The major faces of these specimens were (001) planes, and the minor faces were $(1\bar{1}0)$ planes. The other two specimens were cut with the [100] direction parallel to the tensile axis. The major and minor faces of those specimens were {100} planes. Schematics of the two crystal orientations and their dimensioned geometries are shown in Figure 4.1. The wedge-shaped ends facilitated gripping the specimen during tensile loading. Strain gages were attached on opposing major faces near the specimen midpoint to measure the longitudinal and transverse strains. The specimen surface under each strain gage was abraded prior to gage installation to improve bonding.

Tensile tests were conducted at room temperature in air of normal humidity. Specimens were pulled using a hydraulic MTS machine with the cross arm operating in constant velocity mode at ~0.5 μm/s. During the course of each tensile test, the loading changes on the MTS load frame and related fixturing led to slight changes in dimension of the overall test system. As a result, the specimens were subjected to a minor variation in strain rate. Over each specimen's elastic-response regime the strain rate was ~3 x 10^{-6} s^{-1}. Over each specimen's plastic-deformation regime the system load remained more constant and the constant cross arm velocity generated a strain rate of ~18 x 10^{-6} s^{-1}. The tensile test of each specimen took roughly 30 minutes from start to finish. The cross arm displacement, load, and longitudinal and transverse strain gage outputs were digitally recorded at 10 Hz. Specimens were pulled up to 2% strain to develop distinct slip lines without excessive rotation of the original crystal lattice orientation. Slip lines were digitally photographed using both optical and scanning electron microscopy, and their orientation with respect to the tensile axis was determined by computer aided image analysis.

A total of four Fe-Ga specimens were prepared and subjected to tensile testing. However the test results for the first set of [100] and [110] specimens used slightly different test procedures and were inconclusive and are not reported. Insights gained from the first set of tests are reflected in the test procedures just described.

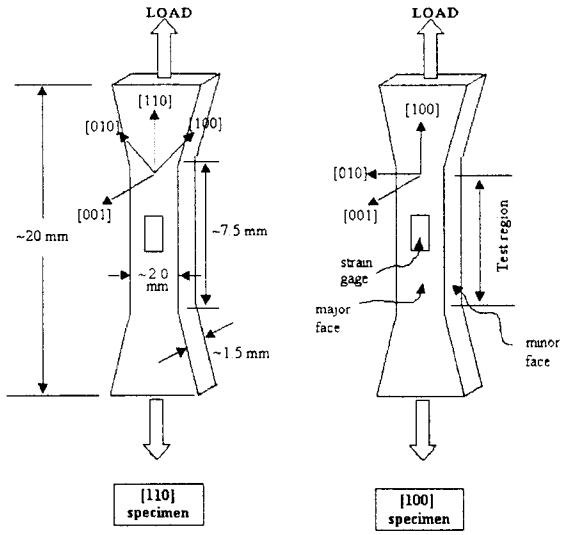

Figure 4.1 Schematic of [110] and [100] oriented single-crystal tensile specimen geometry with loading direction and strain gage locations indicated. Dimensions are approximately the same for all specimens.

4.1.3 Plastic behavior

The plastic responses of the Fe-Ga single crystal, including slip line formation and the non-linear portion of the stress-strain curves, allowed for the determination of the active slip systems and stress levels required to activate them. An analysis of the slip line angles and the corresponding yield stress is carried out first for the [110] specimens and then the [100] specimens to characterize the alloy's plastic properties.

4.1.3.1 Tensile tests with [110] parallel to the tensile axis

The two single-crystal tensile specimens of $Fe_{83}Ga_{17}$ oriented with the tensile axis parallel to the [110] direction displayed sufficient ductility to allow determination of the active slip system and the probable critical resolved shear stress τ_{CRSS}. The strain gage data for one of these specimens was collected to provide a stress-strain plot (Figure 4.2). Analysis of the response gave $E_{[110]} = 160$ GPa in the loading direction and $\nu_{[1\bar{1}0]} = -0.37$ on the (001) major face. Yielding began at 450 MPa and 0.3% elongation leading to a projected 0.2% yield stress of 530 MPa. An ultimate tensile strength of 580 MPa was observed with no fracture occurring through 1.6% elongation. The test was terminated at 1.6% strain with the onset of decreasing tensile load.

As viewed in the optical microscope, the (001) major faces of the specimen displayed two sets of slip lines at a 47.3° angle with the tensile axis (Figure 4.3a). The $(1\bar{1}0)$ planes of the minor faces showed two sets of slip lines, each of which forms a 35.0° angle with the tensile axis (Figure 4.3b).

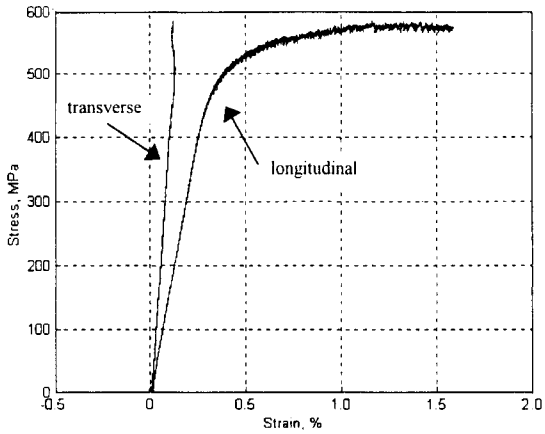

Figure 4.2 Stress vs. strain plot for $Fe_{83}Ga_{17}$ single-crystal tensile test with the tensile axis parallel to the [110] direction. Note that the positive readings of the transverse strain give a negative Poisson's ratio.

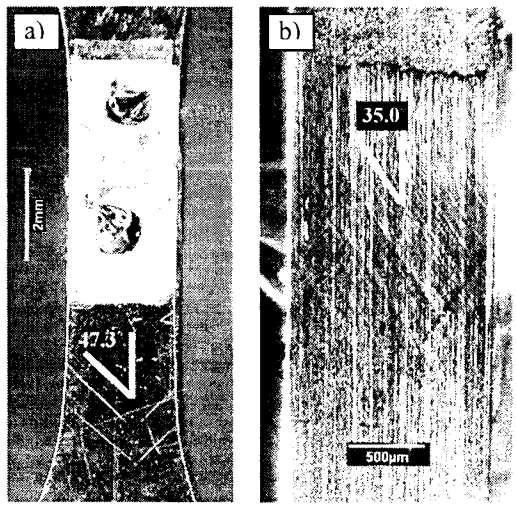

Figure 4.3 Optical micrographs of $Fe_{83}Ga_{17}$ single-crystal slip lines with the tensile axis parallel to the [110] direction. The angle of the slip lines with respect to the tensile axis are indicated: a) The (100) major face of a tensile test specimen; b) The $(1\bar{1}0)$ minor face of a tensile test specimen.

Four slip planes were considered as candidates for slip in this alloy: {100}, {110}, {211}, and {321}. These four planes are the only planes in the BCC structure with a reasonably high planar atomic packing density, so they are usually considered to be the only

plausible slip plane candidates in the BCC structure [Cox 1957]. Figure 1.1b shows a (101) plane as an example of the {110} group. The angles of slip lines for each of these candidate slip planes were calculated for both the major and minor faces of these specimens, and the results of these calculated angles were compared to the observed slip line angles from the tensile test specimens. The results of this comparison are shown in Table 4.1.

Slip Plane	Calculated Slip Line Angles with the Tensile Axis on the Major Face	Calculated Slip Line Angles with the Tensile Axis on the Minor Face
{100}	45°, 90°	0°, 90°
{110}	0°, 45°, 90°	35.3°, 90°
{211}	0°, 18.4°, 71.6°, 90°	0°, 35.3°, 64.8°
{321}	11.3°, 18.4°, 26.6°, 63.4°, 71.6°, 78.7°	13.3°, 35.3°, 54.7° 74.2°

Observed Slip Line Angles with the Tensile Axis on the Major Face	Observed Slip Line Angles with the Tensile Axis on the Minor Face
47.3°	35.0°

Table 4.1 Calculated angles of slip lines for four candidate slip planes for a specimen with the tensile axis parallel to the crystallographic direction. The observed slip line angles are shown in the lower portion of the table for comparison. Note that only the {110} calculated slip plane angles are consistent with the observed slip line angles.

Slip on the {110}, {211}, and {321} planes are all capable of producing slip lines on the minor face with an angle of 35.3° to the [110] direction of the tensile axis. However, only the {110} slip plane shows a reasonable match between the calculated and observed slip line angles on both the major and minor faces simultaneously. The 0.3° discrepancy between the observed angle of 35.0° and the calculated angle of 35.3° may be attributed to errors in measurement (principally small deviations from a perpendicular viewing line of sight while photographing slip lines in the microscope) and to slip plane rotation during the 1.6% strain of the samples. The disparity between the calculated 45° angle and the observed 47.3° angle is thought to have similar causes. From this analysis one can conclude that the active slip plane in these specimens was the {110}.

There are three slip directions lying on the {110} planes that have a reasonably high linear atomic density in the α structure; these are <111>, <100>, and <110> (Table 4.2). Of

these, the <111> is the most likely slip direction since it has substantially higher linear packing density than the others, and it is the dominant slip direction in BCC metals. Figure 1.1b shows the $[11\bar{1}]$ direction as an example. However, to test the feasibility of slip in the <100> and <110> directions, a Schmid factor analysis was performed.

Recalling Schmid's Law (Equation 4.1) for resolved shear stress [Dieter 1988]:

$$\tau = \sigma(\cos\phi)(\cos\gamma) \tag{4.1}$$

where τ is the shear stress on a given slip plane, σ is the tensile stress on the sample, ϕ is the angle between the slip plane's normal vector and the tensile axis, and γ is the angle between the slip direction and the tensile axis. The $(\cos\phi)(\cos\gamma)$ product is often referred to as the Schmid factor. Orientations with a large Schmid factor (0.5 is the maximum value possible) are favored for slip since the shear stress (τ) needed to move dislocations is directly proportional to the Schmid factor for a given tensile stress (σ) on the crystal.

The <111> slip direction has a large Schmid factor in this test orientation (Table 4.2); the <100> and <110> directions have smaller, but non-zero Schmid factors. Thus, one can conclude that it is probable that the slip direction was <111> in this specimen, but the possibility of slip in the <100> and <110> directions cannot be ruled out. If <111> is assumed to be the slip direction, the τ_{CRSS} = 220 MPa for slip on the {110}<111>.

Slip Direction	Schmid Factor for {110} Slip Plane with a [110] Tensile Axis	Critical Resolved Shear Stress for {110} Slip Plane with a [110] Tensile Axis
<111>	0.41	220 MPa
<100>	0.35	190 MPa
<110>	0.25	130 MPa

Table 4.2 Schmid factors, $(\cos\phi)(\cos\gamma)$, and critical resolved shear stress for three possible slip directions on the {110} plane in a specimen with the tensile axis parallel to the [110] crystallographic direction. Note that all three directions have non-zero Schmid factors, so each direction is a possible slip direction on the {110} planes. As discussed in Section 4.1.3.1, the <111> direction is believed to be the most probable slip direction.

4.1.3.2 Tensile tests with [100] parallel to the tensile axis

The single crystal tensile specimens of $Fe_{83}Ga_{17}$ oriented with the tensile axis parallel to the <100> direction also displayed sufficient ductility to allow determination of the active slip system and the probable τ_{CRSS}. The strain gage data for this specimen is presented in a stress-strain plot in Figure 4.4. Analysis of the response gave $E_{[100]}$ = 65 GPa in the loading direction and $\nu_{[010]}$ = 0.45 on the (001) major face. Discontinuous yielding began at 0.8% elongation, which was thought to result from twinning, kink band formation, or stress-induced phase transformation. A clearly audible sound similar to that of twinning accompanied the discontinuous yielding event between 0.8 and 1.5% strain. Several more acoustic events occurred beyond 2% strain at progressively lower stress levels. A maximum tensile strength of 515 MPa was observed with fracture occurring shortly after 2% elongation. Strain gage data collection was terminated at -0.3% strain in the transverse direction and 2.0% strain in the axial direction.

As viewed in the optical microscope and the SEM, the {100} major faces and {100} minor faces of the specimens displayed slip lines at a ±63.2° angle with the tensile axis (Figure 4.5a and b).

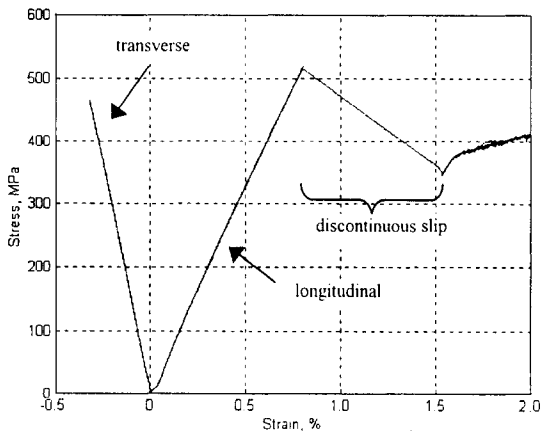

Figure 4.4 Stress vs. strain plot for $Fe_{83}Ga_{17}$ single-crystal tensile test with the tensile axis parallel to the [100] direction. Strain gage data collection was terminated at -0.3% strain in the transverse direction and 2.0% strain in the axial direction.

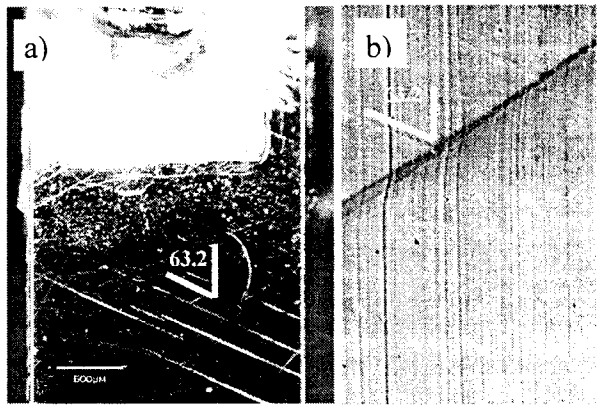

Figure 4.5 Micrographs of slip lines of a $Fe_{83}Ga_{17}$ single-crystal tensile test specimen with its tensile axis parallel to the [100] direction. The angles of the slip lines with respect to the tensile axis are indicated. a) Optical micrograph of the (001) major face b) SEM of the (010) minor face. The prominent slip line from middle left to upper right is a possible twinned or kink band region. The vertical lines are polishing artifacts.

As Table 4.3 indicates, both the {211} and {321} slip planes are consistent with the 63.2° angle observed on the major and minor specimen faces. It is possible, however, to discriminate which of these two planes is slipping by calculating the Schmid factors of all 24 {211} slip planes and all 48 {321} slip planes (assuming <111> slip directions). If the particular planes that form 63.4° slip lines are the same ones that have the largest Schmid factors for this tensile axis orientation, then slip may be occurring on that plane; however, if the particular planes that form 63.4° slip lines do not have the largest Schmid factors for this tensile axis orientation, then that slip plane cannot be the one that is active in these specimens. In the {321} family of planes, the specific planes that would form a 63.4° slip line on the major and minor faces are the eight possible sign permutations of the (312) planes. Those eight planes all have a Schmid factor of 0.31. However, other {321} planes have a Schmid factor of 0.46, and those planes did not form slip lines on the specimen faces. This indicates that {321} slip did not occur in these specimens. In the case of the {211} planes, the planes that have the largest Schmid factor (0.47) are the eight sign permutations of the (211). All other {211} planes have smaller Schmid factors, which indicates that {211} slip is possible. Since no other candidate slip plane satisfies the slip criteria and the <111> direction lies in the slip plane with the largest Schmid factor, as shown in Table 4.4, one concludes that the slip observed in these specimens was {211}<111>.

Slip Plane	Calculated Slip Line Angles with the Tensile Axis on the Major and Minor Faces
{100}	90°
{110}	45°, 90°
{211}	26.6°, 45°, 63.4°
{321}	18.4°, 26.6°, 33.7°, 56.3°, 63.4°, 71.6°

Observed Slip Line Angle with the Tensile Axis on the Major and Minor Face
63.2°

Table 4.3 Calculated angles of slip lines for four candidate slip planes for a specimen with the tensile axis parallel to the [100] crystallographic direction. The observed slip line angles are shown in the lower portion of the table for comparison. Note that both the {211} and {321} calculated slip plane angles are consistent with the observed slip line angles.

Slip Direction	Schmid factor for {211} Slip Plane with a [100] Tensile Axis	Critical Resolved Shear Stress for {211} Slip Plane with a [100] Tensile Axis
<111>	0.47	240 MPa
<110>	0.29	148 MPa
<100>	No <100> directions in the {211}plane	--------

Table 4.4 Schmid factors, $(\cos \phi)(\cos \gamma)$, and critical resolved shear stress for three slip directions on the {211} plane in a specimen with the tensile axis parallel to the [100] crystallographic direction.

Determination of the yield stress in this specimen is problematic since, as Figure 4.4 shows, a discontinuous yield event occurred before 0.2% offset strain was reached. For this reason, the 515 MPa stress value at the onset of the discontinuous yielding was used as the yield-stress value. For the <111> slip direction (Table 4.4), a 515 MPa yield-stress value can be used in Schmid's Law to estimate that $\tau_{CRSS} \approx 240$ MPa for slip on the {211}<111>. This τ_{CRSS} is only slightly higher than the 220 MPa value determined for {110}<111> slip (Section 4.1.3.1). The highest Schmid factor for {110}<111> slip in the specimens with the [100] direction as the tensile axis is 0.41, which is lower than the 0.47 Schmid factor calculated for {211}<111> slip in these specimens. Even though the τ_{CRSS} values were nearly

equal for these two slip systems, one would expect {211}<111> slip to occur in preference to {110}<111> slip due to the higher Schmid factor, and indeed that was observed in these specimens.

4.1.4 Elastic behavior

Utilizing the linear portions of the stress-strain curves in Figures 4.2 and 4.4, the elastic responses of the respective [110] and [100] oriented single-crystal specimens were ascertained. The three elastic constants c_{11}, c_{12}, and c_{44} may then be determined using the Young's moduli and Poisson's ratios from each of the [100] and [110] oriented crystals in combination. The simultaneous solution of Equations 1.17 and 1.18 allow constants c_{11} and c_{12} to be represented in terms of $E_{[100]}$ and $\nu_{[010]}$ as given in Equations 4.2 and 4.3.

$$c_{11} = \frac{(1-\nu_{[010]})E_{[100]}}{(1+\nu_{[010]})(1-2\nu_{[010]})} \tag{4.2}$$

$$c_{12} = \frac{\nu_{[100]}E_{[100]}}{(1+\nu_{[010]})(1-2\nu_{[010]})} \tag{4.3}$$

Accounting for the maximum error in stress and strain, the variable $E_{[100]}$ is known to within 3% for this sample. The error in the Poisson's ratio is estimated at less than 1% by considering the combined error in longitudinal and transverse strain measurements. Using values of $E_{[100]} = 64.5 \pm 1.8$ GPa and $\nu_{[010]} = 0.445 \pm 0.004$ (from Figure 4.2) then $c_{11} = 225 \pm 20$ GPa and $c_{12} = 181 \pm 20$ GPa. Notice that the difference in these elastic constants, c_{11}-$c_{12} = E_{[100]}/(1 + \nu_{[010]}) = 44.6 \pm 1.3$ GPa, has a relatively small error bar compared to either c_{11} or c_{12} alone. This fact suggests that the values of c_{44} and the anisotropy parameter A (Equation 1.22) may be known with higher accuracy.

To estimate the value of c_{44}, either Equations 1.19, 1.20 or 1.21 may be used in conjunction with the previously determined values of c_{11} and c_{12}. Since both $E_{[110]}$ and $\nu_{[1\bar{1}0]}$ were measured in this study, comparisons of c_{44} calculated using Equations 1.19 and 1.20 are possible. The values of $E_{[110]} = 160.4 \pm 1.8$ GPa and $\nu_{[1\bar{1}0]} = -0.374 \pm 0.004$ were determined from the [110] specimen's stress-strain curves (Figure 4.4) where the same range of error conditions were present as in the testing of the [100] oriented specimen. A sensitivity

analysis shows that admissible solutions satisfying both Equations 1.19 and 1.20 give c_{44} = 128 ± 2 GPa.

4.2 Discussion of Fe-17Ga single-crystal mechanical properties

At room temperature, the slip system of the $Fe_{83}Ga_{17}$ single crystals observed in this study are consistent with those of Fe, Fe-Si and Fe-Al alloy systems. $Fe_{83}Ga_{17}$ single crystals exhibited primary slip on the {110}<111> with τ_{CRSS} = 220 MPa (measured in the [110] crystal) and secondary slip on the {211}<111> with τ_{CRSS} = 240 MPa (measured in the [100] crystal). The primary slip system in high purity (99.96%) α-Fe is {110}<111> with τ_{CRSS} = 27.5 MPa and secondary slip occurring on the {211}<111> and {321}<111>. The primary slip system of $Fe_{97}Si_3$ alloy is mixed with {100}<111> and {211}<111> both active at τ_{CRSS} ~ 150 MPa [Orlans-Joliet 1990]. The aluminides such as $Fe_{60}Al_{40}$ and $Fe_{57}Al_{43}$ single crystals both exhibit primary slip on the {110}<111> with τ_{CRSS} values between 82 and 94 MPa [Baker 2001]. Notably, τ_{CRSS} is significantly larger for the Fe-Ga and Fe-Al alloys compared to pure α-Fe. According to the Friedel relationships, the increase in τ_{CRSS} with the presence substitutional atoms is due to crystal lattice strain, which provides a larger energy barrier to dislocation movement [Nabarro 1982]. The atomic radii of Si, Al and Ga are all roughly 10% greater than that of Fe (all with a coordination number of 8 in the BCC lattice), hence justifying that the lattice interactions are similar. The stress-strain curves of Figure 4.2 and Figure 4.4 demonstrate that strain hardening is limited in both of the [100] or [110] samples. Limited strain hardening indicates a lack of dislocation tie-up and is consistent with the predominance of one active slip system [McLean 1962].

Environmental embrittlement may be a factor in the limited elongations of the $Fe_{83}Ga_{17}$ single crystals. The crystal with a tensile axis orientation of [110] began to experience a stress decline beyond 1.3% elongation (Figure 4.2), indicating that elongation greater than 1.6% was limited. The crystal with a tensile axis orientation of [100] was pulled to failure with fracture occurring shortly after 2% elongation (Figure 4.4). Previous work at room temperature has shown that $Fe_{60}Al_{40}$ and $Fe_{57}Al_{43}$ single crystals both had higher elongations of ~40% before fracture in a dry oxygen atmosphere compared to 20 to 30% in a vacuum and only 10% in air [Baker 2001]. This embrittlement effect in aluminides is

attributed to the catalyzed decomposition of atmospheric water vapor at the metal surface to form hydrogen, which penetrates the material and facilitates crack propagation. Strain rate is also known to be a factor where the elongation of $Fe_{60}Al_{40}$ single crystals in air have been shown to have 6% and 24% elongations respectively for 10^{-6} s^{-1} and 1 s^{-1} strain rates [Wu 2001]. It is possible that the plastic properties of the FeGa alloys are affected in a similar fashion.

Observations revealed that the elastic response of α-Fe single crystal was dramatically affected by the addition of Ga. Significant property changes include Young's modulus, Poisson's ratio and the elastic anisotropy. Although the described Fe-17Ga elastic results are the first data being reported for Fe-Ga alloys as a result of tensile testing, acoustic measurements by Clark *et al.* also provided data for the determination of the c_{11}, c_{12} and c_{44} elastic constants. Table 4.5 summarizes the elastic response for single-crystal high-purity (99.96%) α-Fe and Fe with substitutions up to 27.2 at.% Ga. Comparing $Fe_{72.8}Ga_{27.2}$ to pure Fe, the Ga addition caused a large 57% increase in c_{12} while c_{44} increased only 15% and c_{11} declined by 3%. The combined effect of these changes was to reduce $E_{[100]}$ to less than one-sixth of its original value (from 131 to 20 GPa) and raise the elastic anisotropy over eight-fold from 2.4 to 19.9. Accompanying the large increase in elastic anisotropy, the Poisson's ratio for [110] crystal loading became significantly more negative in the $[1\bar{1}0]$ direction with $\nu_{[1\bar{1}0]}$ changing from -0.06 to an extreme value of -0.75. Volume conservation dictates that to a first approximation $\nu_{[1\bar{1}0]} + \nu_{[001]} = 1$. From the last two columns of Table 4.5 one

at. % Ga in Fe	in GPa							[100] loading	[110] loading	
	c_{11}	c_{12}	c_{44}	$E_{[100]}$	$E_{[110]}$	$E_{[111]}$	A	$\nu_{[010]}$	$\nu_{[1\bar{1}0]}$	$\nu_{[001]}$
0[A]	228	132	117	131	219	283	2.4	0.37	-0.06	0.61
17.0[B]	225	181	128	65	160	315	5.7	0.45	-0.37	1.11
18.7[C]	196	156	123	57	145	297	6.2	0.44	-0.41	1.13
24.1[C]	186	168	120	27	86	293	12.9	0.47	-0.64	1.48
27.2[C]	221	207	135	20	68	334	19.9	0.48	-0.75	1.64

Table 4.5 Elastic properties of single crystal $Fe_{100-x}Ga_x$, where $0 \leq x \leq 27.2$. Subscripts indicate the directionality of the property. [A]Data from Mclean *et al.* [Mclean 1972]. [B]Data from quasi-static measurements in this study. [C]Data from acoustic measurements by Clark *et al.* [Clark 2003].

observes that adherence to this relationship significantly improves with increasing Ga content. In the case of Fe $\nu_{[1\bar{1}0]} + \nu_{[001]} = 0.55$, while for Fe-27.2Ga $\nu_{[1\bar{1}0]} + \nu_{[001]} = 0.89$.

The elastic constants of single crystal $Fe_{100-x}Ga_x$, where $0 \leq x \leq 27.2$ from Table 4.5 are used in Equations 1.20 and 1.21 to examine changes in $\nu_{[1\bar{1}0]}$ and $\nu_{[001]}$ for a [110] loading condition. A plot of these results (Figure 4.6) shows trends of increasingly negative $\nu_{[1\bar{1}0]}$ (from -0.06 to -0.75) and increasingly positive $\nu_{[001]}$ (from 0.61 to 1.64) occurring as quadratic functions of Ga content. The elastic anisotropy reflects this trend where A increases from 2.4 to 19.9. The value of A = 19.9 calculated for the $Fe_{83}Ga_{27.2}$ alloy is presently the largest anisotropy value known to us.

The Fe-Al alloy system bears similarity to the Fe-Ga alloy studied in this work and suggests that a peak in the elastic anisotropy may occur. For $Fe_{100-x}Al_x$, where $0 \leq x \leq 40.1$, calculations show an increase from A = 2.4 in pure Fe to a maximum A = 6.5 occurring for

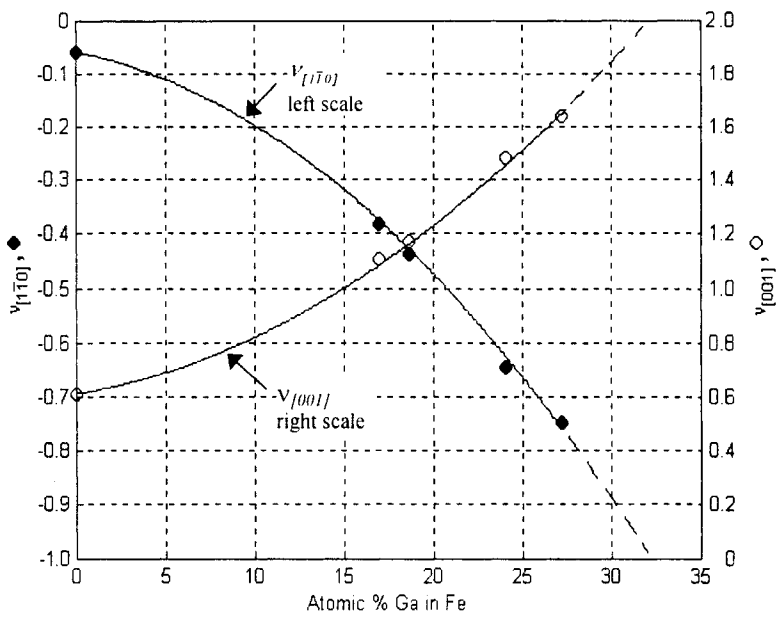

Figure 4.6 Calculated Poisson's ratios for [110] loading of $Fe_{100-x}Ga_x$, where x = 0, 17.0, 18.7, 24.1 and 27.2. $\nu_{[1\bar{1}0]}$ and $\nu_{[001]}$ are orthogonal directions which lie respectively in the (001) and $(1\bar{1}0)$ planes. The 17.0% Ga data point was measured in this study while the remaining values are calculated from Equations 1.20 and 1.21 using data in Table 4.5. Lines represent quadratic fits of the data, which are given as: $\nu_{[1\bar{1}0]} = -0.000693x^2 - 0.00683x - 0.0583$ and $\nu_{[001]} = 0.00101x^2 + 0.0108x + 0.6130$ where x = at.% Ga.

25.1% Al. The associated Poisson's ratios at this peak anisotropy are $\nu_{[1\bar{1}0]}$ = -0.44 and $\nu_{[001]}$ = 1.10. Thereafter, A decreases to 3.8 for the 40.1% Al substitution level. See Appendix C for a detailed plot of the Poisson's ratio dependencies with respect to Al substitution.

Although the level of Ga substitution giving a maximum A remains to be determined, the corresponding minimum $\nu_{[1\bar{1}0]}$ and maximum $\nu_{[001]}$ must be greater than -1 and less than 2, respectively. These theoretical bounds are presented in the electron-gas model proposed by Baughman *et al.* for the thermodynamically admissible Poisson's ratios [Baughman 1998]. If the quadratic fits of the data in Figure 4.6 continue to hold beyond 27.2% Ga, the minimum $\nu_{[1\bar{1}0]}$ and maximum $\nu_{[001]}$ should occur near 32% Ga. Considering that the Fe-24.1Ga and Fe-27.2Ga specimens were quenched from above 700°C, the presence of an ordered B2′ phase (Figure 1.4) may influence the elastic anisotropy and Poisson's ratios. It is possible that a phase change from B2′ to B2 near 32% Ga gives rise to the projected extreme values in A, $\nu_{[1\bar{1}0]}$ and $\nu_{[001]}$.

Previous surveys of cubic metals by Baughman *et al.* showed that 21 of 32 elemental metals possess negative Poison's ratios [Baughman 1998]. Second in magnitude to the Fe-27.2Ga alloy, the elastic properties for Li are A = 9.2, $\nu_{[1\bar{1}0]}$ = -0.55 and $\nu_{[001]}$ = 1.30. The elastic properties of several elements and alloys, compiled by Jain *et al.*, are included in Table 4.6 for reference.

Element	Crystal structure	Elastic constants in GPa			A	$\nu_{[1\bar{1}0]}$	$\nu_{[001]}$
		c_{11}	c_{12}	c_{44}			
Fe-27.2Ga	bcc	221	207	135	19.9	-0.75	1.64
Li	bcc	14.8	12.5	10.8	9.2	-0.55	1.31
CuZn	NaCl	129	110	82.4	8.5	-0.52	1.29
Na	bcc	8.08	6.64	5.86	8.1	-0.51	1.24
K	bcc	4.10	3.41	2.6	7.5	-0.48	1.23
Fe-25.1Al	bcc	171	131	132	6.5	-0.44	1.10
Cu	fcc	168	121	75.4	3.2	-0.14	0.84
Ag	fcc	124	93.7	46.1	3.0	-0.10	0.83

Table 4.6 Elastic properties and computed elastic anisotropy A and Poisson's ratios $\nu_{[1\bar{1}0]}$ and $\nu_{[001]}$ for the respective [1 $\bar{1}$ 0] and [001] directions on the (001) plane (after [Jain 1990]).

4.3 Tension testing of Fe-17Ga cold-rolled polycrystal

The tensile properties of a cold rolled polycrystalline $Fe_{83}Ga_{17}$ specimen (see sample R6 produced using the methods of section 2.3.2.3) were measured to ascertain its elastic and plastic properties. Considering the specimen's cold working history and combination of dispersed {001}<110> and {111}<211> texture components (Figure 2.19), its properties are expected to deviate from those of either the [100] and [110] single crystal specimens measured in Section 4.1 and 4.2. The evaluation of this rolled material's Young's modulus, Poisson's ratio, yield strength and percent elongation will provide a new point of reference for the design of magnetically active structural components.

The rolled tensile specimen was extracted from the R6 sample parent material using EDM, where the longitudinal axis (tensile loading direction) was oriented parallel to the specimen's rolling direction. The same dimensions were used as for the single crystal specimens to give the "dog bone" shape of Figure 4.1, however the thickness was 0.16 mm. To minimize surface defects and hence stress concentrations, the specimen's major faces and edges were polished with wetted 600-grit silicon carbide paper. The same strain gage configuration and tensile testing parameters were used as in the case of the single-crystal tests described in section 4.1.2.

The stress-strain plot (Figure 4.7) shows that both the transverse and longitudinal curves exhibited an elastic response to 650 MPa to be followed by plastic behavior up to a maximum stress of 840 MPa. The tension test was terminated at a 1.5% longitudinal strain when specimen failure occurred in a non strain-gaged region. The initial portion of the longitudinal response demonstrated some non-linearity through 100 MPa (or 36 N for this cross sectional area) possibly due to residual bending stresses induced in this thin sample during strain gage installation. The longitudinal response also demonstrated a proportional limit of 0.4% strain at 600 MPa and a 0.2% yield stress of 790 MPa. An analysis of the linear stress-strain regime, over the 300 to 500 MPa range, gave a Young's modulus in the rolling direction of E_{RD} = 154 GPa and Poisson' ratio ν = 0.25. Although E_{RD} is comparable to the single crystal value of $E_{[110]}$ = 160 GPa (see Table 4.5 for Fe-17Ga), the positive ν suggests that a <110> fiber texture dominates any {001}<110> sheet texture content. If the

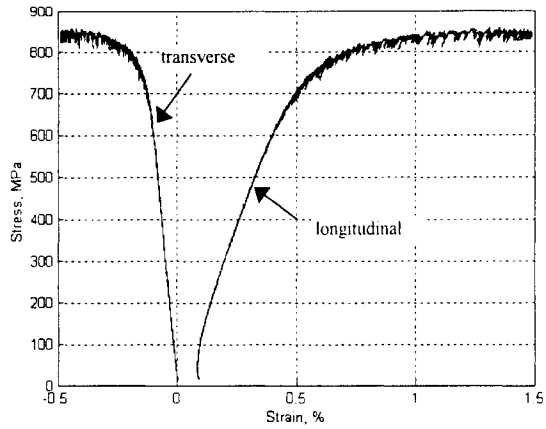

Figure 4.7 Stress vs. strain plot for a tensile test of cold-rolled polycrystalline $Fe_{83}Ga_{17}$ tensile test with the tensile axis parallel to the rolling direction. Tensile testing was terminated at -0.5% transverse strain and 1.5% longitudinal strain simultaneously due to specimen failure in a non strain-gaged region.

{001}<110> sheet texture were indeed present in any significant quantity, the observed ν would be negative to more closely match that of $\nu_{[1\bar{1}0]} = -0.37$.

4.4 Fe-Ga mechanical properties summary

Specimens of Fe-17Ga at.% were tested in tension at room temperature. These tests indicated:

- The single-crystal tensile specimens with a [110] tensile axis orientation elongated at least 1.6%, and slip lines on the specimen surfaces indicated that the active slip plane is the {110}. If the slip direction is assumed to be the <111>, the critical resolved shear stress for {110}<111> slip is 220 MPa. Yielding began at 0.3% elongation and 450 MPa. The ultimate tensile strength was 580 MPa.
- The single-crystal tensile specimens with a [100] tensile axis orientation elongated at least 2%, and slip lines on the specimen surfaces indicated that the active slip plane is the {211}. If the slip direction is assumed to be the <111>, the critical resolved shear stress for {211}<111> slip is 240 MPa. Discontinuous yielding began at 0.8% elongation and 515 MPa and may be due to twinning, kink band formation, or stress-induced transformation to another phase.

- The single-crystal Young's modulus was 160 GPa for loading in the [110] crystal direction with Poisson's ratio of -0.37 on the (001) major face.
- The single-crystal Young's modulus was 65 GPa for loading in the [100] crystal direction with Poisson's ratio of 0.45 on the (001) major face.
- The corresponding elastic constants are c_{11} = 225 ± 20 GPa, c_{12} = 181 ± 20 GPa and c_{44} = 128 ± 2 GPa with an elastic anisotropy of 5.7.

Analysis of other Fe-Ga single crystal and polycrystalline alloys revealed that:

- An Elastic anisotropy value of 19.9 was identified for single crystal $Fe_{72.8}Ga_{27.2}$ leading to a calculated in-plane negative Poisson's ratio of -0.75.
- Both Poisson's ratios $\nu_{[1\bar{1}0]}$ and $\nu_{[001]}$ are highly-correlated quadratically to the substitution levels of Ga and Al in the Fe-Ga and Fe-Al alloy systems.
- The cold rolled Fe-17Ga at.% polycrystalline specimen underwent an elongation of at least 1.5% before failure. Yielding began at 0.4% elongation and 600 MPa while the ultimate tensile strength was 840 MPa. The Young's modulus was 154 GPa for loading in the rolling direction with a corresponding Poisson's ratio of 0.25.

These results identifying the active slip systems and shear stresses provide insight to the possible development of texture or preferred crystallographic orientation in polycrystalline forms of Fe-Ga alloys. The common slip mechanisms recognized for the Fe-Ga, Fe-Si and Fe-Al alloy systems suggest that successful texturing methods used for Fe-Si and Fe-Al might be mimicked to optimize polycrystalline Fe-Ga texture for magnetostriction and structural applications. Environmental embrittlement and strain-rate dependencies have been observed in Fe-Al and could also be a significant factor for the Fe-Ga alloys. These effects warrant investigation as they affect the strength and formability of the material. The elastic properties of the Fe-Ga alloy were observed to be increasingly anisotropic with rising Ga content for the stoichiometries examined (0 to 27.2 at.%). The large elastic anisotropies generate a remarkably large-magnitude negative Poisson's ratio. This negative Poisson's ratio creates a significant in-plane auxetic behavior that could be exploited in applications that capitalize on unique area effects produced under uniaxial loading.

5. MODELING SATURATION MAGNETOSTRCTION IN POLYCRSTALS

Successfully merging Fe-Ga alloy's optimal single-crystal magnetostrictive performance with desirable polycrystalline mechanical characteristics will depend on our knowledge of the material's combined magnetic and micromechanical behavior. It is hypothesized that the influences of microstructural features play a significant role affecting the overall material response provided the material properties are sufficiently anisotropic. To gain an understanding of how saturation magnetostriction and the elastic response of polycrystalline Fe-Ga alloys depend on crystallographic texture and grain morphology, this work utilizes a Magnetostrictive Micromechanics Finite–Element Model (MMFEM) that was developed and used to examine the stress and strain changes within the material due to changes in magnetization. The ultimate objective in developing this model is to determine whether, for a given texture distribution, misalignments between the grains' crystallographic orientations result in significant internal stresses that impede the desired bulk magnetostrictive response.

This chapter first reviews existing analytic methods for estimating the magnetostrictive response of a limited class of polycrystals (Section 5.1) and motivates the development of the MMFEM approach. An explanation of the model is presented (Section 5.2) along with its validation through comparison to experimental results for a large-grained rolled specimen (Section 5.3). Next, the methodology for simulating an equiaxed grain structure and assigning a crystallographic orientation distribution is presented (Section 5.4). Various crystallographic textures are then simulated and compared to experimental saturation magnetostriction results (Section 5.5) for several of the specimens whose method of manufacture was described in Chapter 2. The specimens examined include those derived from material textured by extrusion and cold rolling as well as the non-aligned sintered powder. A texture sensitivity analysis next reveals just how precise a texture distribution must be to achieve stated magnetostriction objectives. The chapter concludes with a summary of the MMFEM results.

5.1 Modeling approaches

Several modeling approaches have been used in the past to estimate the saturation magnetostriction λ_s, arising from an ideal demagnetized state, for polycrystalline materials composed of randomly oriented grains. As given in Equation 5.1, in each of these models λ_s is represented as a linear combination of the cubic magnetostriction constants and the variable α, which depends on assumptions made regarding grain interactions.

$$\lambda_s = \alpha\lambda_{100} + (1-\alpha)\lambda_{111} \tag{5.1}$$

The simplest modeling approach assumes a condition of constant stress throughout the polycrystalline aggregate and yields the Akulov approximation where $\alpha = 2/5$. This analytical result assumes no grain interaction and is equivalent to an average magnetostriction that is derived from the volume integration of the saturation magnetostriction relationship of Equation 1.4 [Cullity 1972]. Although the simplicity of this model is attractive, it is generally in poor agreement with experimental results for Fe and Ni among other materials [Callen 1965]. In other work, a modeling approach was developed utilizing the other extreme of mechanical constraints, i.e. constant strain conditions throughout the polycrystalline aggregate (similar to the Voigt approximations). In this case $\alpha = 2/(2+3A)$ where $A = 2c_{44}/(c_{11}-c_{12})$. The material constant A is equivalent to the elastic anisotropy parameter previously given in Equation 1.22. The results of this method were asserted by Callen *et al.* to be in better agreement with the experimental results, however a more realistic representation was still desired. As neither the assumption of constant stress or constant strain is physically reasonable, an intermediate method was developed by Vladimirsky. In this approach the local stress for each grain approximates that of a spherical crystal surrounded by a homogeneous and isotropic material that is representative of the properties of the polycrystalline aggregate as a whole. An empirical fit of Vladimirsky's result by Callen *et al.* gives the result of $\alpha = [(2/5) - (\ln A)/8]$, where A is again the elastic anisotropy. Results of the Vladimirsky approximation are regarded as a better match to the saturation magnetostriction observed in Fe and other cubic alloys [Callen 1965].

A comparison of the saturation magnetostriction estimates using the Akulov, Vladimirsky and Voigt approximations are given in Table 5.1 for polycrystalline $Fe_{83}Ga_{17}$, $Fe_{80}Ga_{20}$ and $Fe_{72.8}Ga_{27.2}$ alloys having random texture distributions. The single crystal magnetostriction constants and elastic anisotropy for each stoichiometry are also given for reference. The material properties were gathered from Figure 2.4 and Table 4.5 using interpolation as needed. The variability in the results for the different approximation methods illustrates the sensitivity to the underlying assumptions for stress and strain. Recalling the $Fe_{80}Ga_{20}$ powder metallurgy outcome (Section 2.3.3) with $\lambda_{\parallel-\perp}$ ranging from 60 $x10^{-6}$ to 76 $x10^{-6}$, the Vladimirsky approximation with $(3/2)\lambda_s = (3/2)\cdot(43)\ x10^{-6} = 65\ x10^{-6}$ appears most reasonable. Somewhat of a surprise, from the Vladimirsky approximation the furnace cooled $Fe_{80}Ga_{20}$ alloy is projected to have twice as large a λ_s value compared to the $Fe_{83}Ga_{17}$ polycrystal despite a 15% smaller λ_{100} constant. This assumed gain in magnetostriction is due to the large increase in the λ_{111} constant, which more than compensates for the adverse effect of increasing elastic anisotropy.

Material Properties				Random Polycrystal, $\lambda_s\ x10^{-6}$		
Furnace cooled	λ_{100} $x10^{-6}$	λ_{111} $x10^{-6}$	A	Akulov (constant stress)	Vladi-mirsky	Voigt (constant strain)
$Fe_{83}Ga_{17}$	200	-16	5.8	70	23	6
$Fe_{80}Ga_{20}$	170	19	7.0	79	43	21
$Fe_{72.8}Ga_{27.2}$	267	40	19.9	131	46	47

Table 5.1 Comparisons of approximated saturation magnetostriction for polycrystalline Fe-Ga alloys having random crystallographic texture. Estimates are based on material properties measured in furnace cooled single crystals and assumptions of constant stress (Akulov), varied stress (Vladimirsky) or constant strain (Voigt) conditions throughout the polycrystalline aggregate.

Modeling approaches utilizing the linear combination of the cubic magnetostriction constants, and in particular the Vladimirsky approximation with its more realistic underlying stress assumptions, appear helpful in estimating the magnetostriction capability of randomly textured polycrystalline Fe-Ga alloys. However, a modeling method is needed which has the versatility to address materials with crystallographic textures other than those of randomly oriented polycrystalline aggregates. Successful development of Fe-Ga alloys requires the

flexibility to explore the effect of various texture distributions that can arise with different material processing methods, since distributions are strongly influenced by material properties including magnetostriction constants and elastic anisotropy. The MMFEM approach provides this flexibility through inputs that specify grain morphology, crystallographic orientation and material properties. The equilibrium stress and strain state for each grain within the polycrystalline aggregate is computed to evaluate the material's bulk magnetostrictive strain response due to a change from a demagnetized state to one of saturation magnetization. The MMFEM, its application and comparisons of its results to experimental measurements are discussed throughout the remainder of this chapter.

5.2 Overview of the magnetostrictive micromechanics finite-element model

A magnetostrictive material's total or "bulk" strain response ε_{tot} to mechanical loads and saturating magnetic fields may be represented by the linear superposition of elastic strains ε_{elas} and saturation magnetostriction λ_s in the relationship $\varepsilon_{tot} = \varepsilon_{elas} + \lambda_s$. This superposition relationship is fundamental to the three-dimensional finite-element model used in this work to model a polycrystal's total strain response to changes in magnetization from an ideal demagnetized state to one of full saturation in a specified direction. Although a polycrystal may or may not be loaded by external mechanical forces, elastic strains can be developed within each grain due to strains imposed from the anisotropic magnetostriction of neighboring grains having different crystallographic orientations. Aside from forces generated by the product of magnetostriction-induced strain and material stiffness, body forces arising from the existence of internal and external magnetic field gradients are considered to be negligible. The MMFEM formulation is non-dimensional and does not take into account absolute grain size. This is appropriate considering that only small-elastic strains are induced by magnetostriction in the material.

The MMFEM uses constant-strain four-node tetrahedrons to subdivide the material volume, where multiple tetrahedrons compose each grain and are assigned rotationally transformed magnetostrictive and elastic proprieties based on the grain orientation within a global reference frame. Equations 1.4 and 1.12 respectively define the cubic single-crystal anisotropic magnetostrictive and elastic relationships used throughout the model. Tensor

equivalents of these relationships are employed for rotational transformations between local and global coordinate systems. Throughout the polycrystalline aggregate, continuity of displacement is enforced at nodal points comprising the vertexes of adjacent tetrahedral elements. The MMFEM simulates the magnetostrictive strain λ_s by introducing appropriate nodal loading conditions for each element according to the grain's crystallographic orientation and the overall direction of saturation magnetization. Boundary conditions are enforced using the penalty method in which boundary terms of the stiffness matrix and terms of the force vector (related to the degree of freedom being constrained) are modified by a fourfold increase in their order of magnitude. (This scaling factor or larger is commonly used in finite-element methods [Chandrupatla 1991].) Accounting for the elastic response of adjoining grains, the overall system is then solved for the lowest energy state using an isoparametric formulation accommodating the Rayleigh-Ritz potential energy method. This gives the equilibrium nodal displacement condition for the system of elements. The elemental displacements are then converted to elemental strains. Finally, elemental stresses are calculated using the net strain (total minus the initial magnetostrictive strains) and elemental stiffness coefficients. The overall strain of the bulk material ε_{tot} may be found by noting changes in nodal displacements at the boundaries of interest. Introductory texts provide additional details on the finite-element modeling method [Chandrupatla 1991].

5.3 Model validation using through-thickness grains

To validate the MMFEM and gain a sense of the grain interaction developed in a polycrystalline magnetostrictive sample, the simulated and experimentally measured total-strain responses were compared for a disk specimen subjected to directionally applied magnetic fields. The specimen under study, labeled R3, was made from $Fe_{83}Ga_{17}$ rolled material that was subjected to a high-temperature final anneal. Production details for the specimen were described in section 2.3.2.3. Reviewing its manufacture, the rolled sheet was produced by a 96% hot and warm rolling reduction of an as-cast ingot. The disk specimen, 7.9 mm in diameter, was punched from the rolled material having a final thickness of 0.38 mm. A subsequent anneal of the disk for 5 h at 1100 °C in Ar induced secondary recrystallization and produced through-thickness grains with diameters up to ~400 μm.

To provide a basis for the MMFEM simulation, orientation imaging microscopy (OIM) was used to map each grain and its crystallographic orientation over a rectangular region encompassing the central portion of the disk. Figure 5.1 shows the rolling direction (RD) and the mapped region relative to a portion of the disk boundary. The dotted-square boundary outlines the strain-gage location used for actual and simulated strain measurements. The crystallographic misorientation of each grain, relative to a {001}<100> sheet texture, was recorded and plotted in Figure 5.2. The numbered data points correspond to grains of Figure 5.1, which lie within the strain-gaged region. The grain orientation deviations represented by the "x" correspond to the remainder of the mapped grains outlined by the larger rectangular area of Figure 5.1. A lack of data points clustered near the origin of the plot reflects the poor development of cube texture. Furthermore, the absence of data points in upper left half portion of the plot indicates that only grains with large deviations from the sheet normal had large deviations from the rolling direction. The cause of this peculiar orientation distribution remains unknown. To model the specimen with the FEMM method, a fitted mesh consisting of multiple 6-sided polyhedra subdivided the grain structure. These polyhedra compose the volume of the sheet and appear as four-sided polygons at the sheet surface. Each polyhedra is further subdivided into five tetrahedrons.

The actual and simulated strain states of the disk were analyzed for changes in the direction of the saturation magnetization vector from transverse to parallel with that of the rolling direction. To accomplish this analysis, the simulation was run separately for each magnetization direction with the difference noted between the two rolling direction strain results. (This approach is justified by assuming a common initial state of demagnetization.) The FEMM simulation, using material properties for $Fe_{83}Ga_{17}$ listed in Table 5.1, indicated that $\varepsilon_{tot,\ \parallel-\perp} = 177 \pm 3\ x10^{-6}$ relative to the rolling direction; this value falls between the measurements of 160 $x10^{-6}$ and 180 $x10^{-6}$ collected in two separate strain-gage installations. Note that the experimental results are sensitive to minor changes in gage location due to the low number of grains covered and their wide range of crystallographic orientation. The MMFEM was also used to simulate the RD components of stress and strain for a change from a demagnetized state to one of saturation magnetization in the RD. Grains having small angular deviations from the RD (such as 2, 4 and 9) exhibit the largest magnetostrictions with

$\varepsilon_{tot,\parallel}$ ranging from 127 x10^{-6} to 154 x10^{-6}. Variation in $\varepsilon_{tot,\parallel}$ of these grains is influenced by compressive stress levels varying up to 3.6 MPa. These compressive stresses are the result of misoriented neighboring grains having a low $\lambda_{\parallel}$ in the RD.

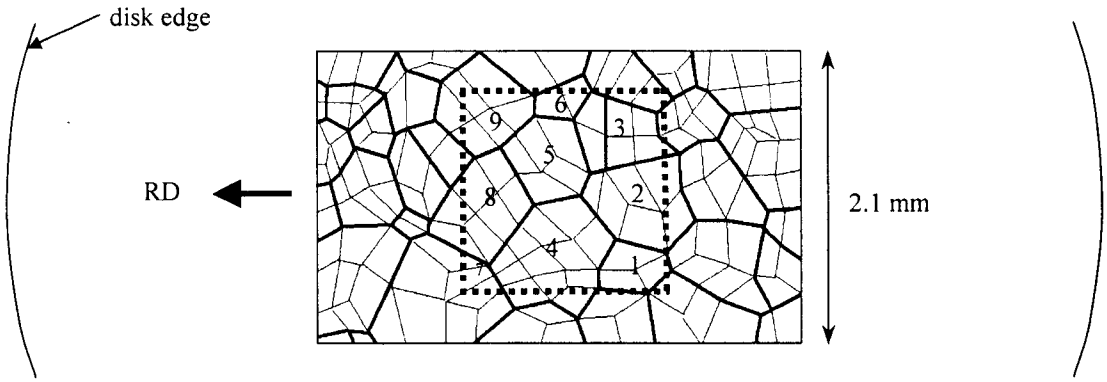

Figure 5.1 Grain map (bold lines) and MMFEM mesh (light lines) for 1100°C annealed rolled $Fe_{83}Ga_{17}$ disk specimen. Outer arcs indicate a portion of the disk boundary and the dotted line denotes the location of the strain-gaged area enclosing numbered grains.

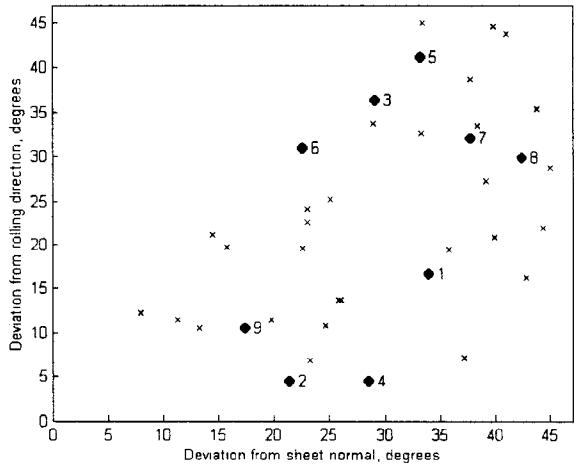

Figure 5.2 Angular deviations of grains' crystallographic orientation from a {001}<100> sheet texture in 1100°C annealed rolled $Fe_{83}Ga_{17}$. Numbered data points (•) correspond to grains in the strain gaged area of Figure 5.1 The data points indicated by (x) correspond to the remainder of the mapped grains outlined by the larger rectangular area of Figure 5.1.

5.4 Representation of an equiaxed grain structure

To carry out MMFEM simulations that explore the effects of crystallographic texture on magnetostriction, a suitable imitation of a polycrystalline metallic grain structure was needed. Once a grain structure is established, the crystallographic orientation of the grains may be assigned using Monte-Carlo techniques to generate random or specific textures having a Gaussian distribution.

5.4.1 Filling space

Observations of metallic microstructures show that they are composed of a network of convex polyhedral cells having planar faces, where the number of faces per polyhedral cell characterizes these grain structures. Typical polycrystalline metals (including the BCC metals) exhibit a distribution of 4 to 36 faces with an average of 14 to 15 faces [Smith 1952, Rhines 1974]. Space filling methods such as the three-dimensional Poisson-Voronoi tesselation scheme (i.e. arraying polyhedra in space) have been devised to simulate realistic grain structures possessing a distribution in polyhedral face numbers using Monte-Carlo techniques [Kumar 1992].

Although a grain modeling approach such as the Poisson-Voronoi tesselation scheme would most accurately represent an undeformed polycrystalline aggregate, a simpler approach was used for this investigation. Unless a specific grain structure was being modeled like the rolled and recrystallized specimen in the previous section, the MMFEM employed equiaxed grains having a constant number of polyhedral faces. Simulating a volume of equiaxed grains permitted this portion of research to focus on how a polycrystalline material's magnetostrictive capability is affected by crystallographic texture rather than grain morphology. Simulating the equiaxed grains of the polycrystalline aggregate, a three-dimensional tesselation of rhombic dodecahedrons was employed. The rhombic dodecahedron has 12 faces, which is near the mean of 14-15 faces determined by Smith, and meets the space-filling requirements without voids. The alternative of tessellating simple cubes was considered and then discarded, as it would provide an inferior representation of real grain morphology. It was also anticipated that cubes would exhibit excessive stress concentrations near the vertexes, with all edges meeting at 90°, compared to the larger angles

of the rhombic dodecahedron where the edges meet at 144.7°. Figure 5.3a depicts a 2x2x2 array of space filling rhombic dodecahedrons, which represents a total of nine grains when including the central polyhedra.

The rhombic dodecahedron representing each grain consists of 14 vertices, which are given by permutations of the groups of (x, y, z) coordinates as (± 1, ± 1, ± 1), (± 2, 0, 0), (0, ± 2, 0) and (0, 0, ± 2). The rhombic dodecahedron may then be subdivided into four equivalent rhombuses, which may be in turn subdivided into six tetrahedra having equal volumes (Figure 5.3b). In total, the rhombic dodecahedron is divided into 24 tetrahedral elements to provide the three-dimensional mesh of each grain in the MMFEM. This subdivision of each rhombic dodecahedron (i.e. grain) provides adequate resolution of the stress and strain fields to capture the major effect of grain interaction on the bulk magnetostriction of the polycrystalline aggregate. The tetrahedral edges make angles greater than 30° with one another to provide favorable aspect ratios for limiting errors in the application of the finite-element method.

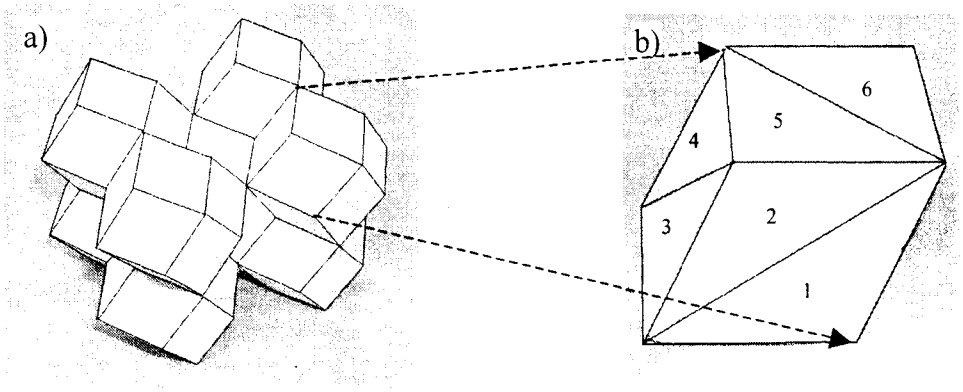

Figure 5.3 a) 2x2x2 array of rhombic dodecahedrons representing a portion of the grain structure for MMFEM simulations. Each rhombic dodecahedron represents a grain, with nine shown here including the central grain. Each rhombic dodecahedron is subdivided into 4 rhombuses which is in turn is subdivided into 6 tetrahedral elements. b) Rhombus with one face of each of the six tetrahedrons visible.

5.4.2 Assigning grain orientations

To prepare the MMFEM for a simulation run, the crystallographic texture of the polycrystalline aggregate was first defined. This involved assigning each grain its crystallographic orientation relative to the global coordinate system. The texture distributions of interest may be divided into two categories. The first is a random distribution, where grains have no preferred orientation. The random distribution is useful for simulating the texture of cast material containing equiaxed grains and for non-aligned powder Fe-Ga alloys. The second is a Gaussian distribution about a defined sheet texture. Crystallographic studies of polycrystalline metals have concluded that the Gaussian distribution provides a good representation of their textures [Barrett 1952]. This approach will find use for simulating deformation processed and aligned powder Fe-Ga alloys. The methods used to implement the random and Gaussian distributions are discussed next.

5.4.2.1 Random texture distribution

A random distribution of crystallographic orientations throughout the simulated polycrystalline material was achieved by defining three angular deviations, including yaw, pitch and roll for each grain. Angular deviations were limited to a range between +45° and -45° due to symmetry. Starting with a grain's local coordinate system (1, 2, 3) aligned with the global coordinate system (x, y, z), rotations were induced by sequential application of specific angular deviations. First, the yaw generated a rotation about the "3" axis. Next, the pitch angle generated a rotation about the newly oriented "2" axis. And finally, the roll angle generated a rotation about the newly oriented "1" axis. Figure 5.4 depicts the crystallographic orientation after the rotations have been applied. Pitch and roll are defined by the respective 1-axis and 2-axes angles relative to the x-y plane, while the yaw relates the 1-axis angle relative to the x-z plane.

Special consideration was needed in determining the yaw and pitch angles to avoid a skewed distribution of the 1-axis location over a solid angle. For example, equating the yaw and pitch angles to random choices of longitude and latitude, for a polar coordinate system projected on a sphere, results in a higher concentration of 1-axis locations at increasing latitudes. (Recall the convergence of lines of longitude near the poles of a globe.) To ensure a

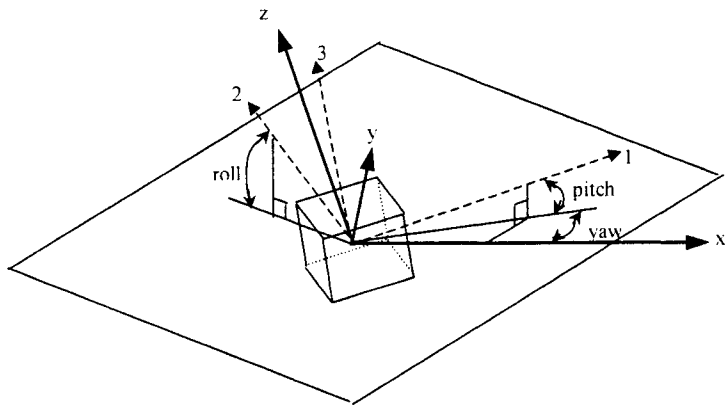

Figure 5.4 Crystallographic orientation of the material coordinate system (1,2,3) relative to the global coordinate system (x, y, z) as defined by angular deviations of yaw, pitch and roll.

random distribution of 1-axis locations, the surface of a sphere was divided into patches having equal areas. The random selections of patches, with their known locations, then provided the distribution of yaw and pitch angles.

5.4.2.2 Gaussian texture distribution

A Gaussian crystallographic orientation distribution was simulated for the polycrystalline material by assigning the angular divergence θ from a sheet texture's rolling direction (RD) and angular divergence φ from the plane normal (PN) direction. Each angular divergence from the RD and PN followed separately specified Gaussian distributions where each distribution was defined by an angular magnitude at one standard deviation. Implementation of the texture assignment in the MMFEM actually started with each grains's material coordinate system (1, 2, 3) aligned with the global coordinate system (x, y, z). Next, as depicted in Figure 5.5, the angular deviation θ between the 1-axis and x-axis was applied in a random direction as marked by the circle. The φ deviation between the 2 axis and x-y plane was then applied through a rotation about the new 1-axis to yield a misaligned grain. Thereafter, the predominant sheet texture was introduced by applying the appropriate rotational coordinate transformation to the misaligned grain.

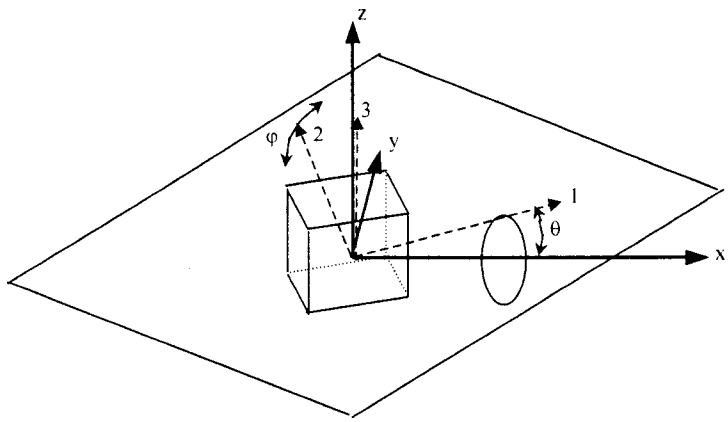

Figure 5.5 Crystallographic orientation of the material coordinate system (1, 2, 3) relative to the global coordinate system (x, y, z) as defined by angular deviations from the RD by angle θ and PN by angle φ.

In the limit, the Gaussian distribution could theoretically provide a crystallographic texture that approaches that of a single crystal if the Gaussian distribution was defined to have an angular divergence of zero at one standard deviation. In contrast, a crystallographic texture that approaches that of a pure randomness could be created using a Gaussian distribution that approaches an infinite angular divergence at one standard deviation. Despite the possibility of using the Gaussian distribution to approximate a random distribution, a "random texture approach" (Section 5.4.2.1) was retained in the MMFEM given its intrinsic randomness.

5.5 MMFEM results of various textures

The MMFEM was used to further explore the bulk magnetostrictive properties of polycrystalline Fe-Ga alloys. Comparisons between simulated and experimental measurements for random, extruded and cold-rolled textures were made to provide further validation of the MMFEM. Additionally, simulations of hypothetical specimens having various textures and stoichiometries lead to predictions of bulk magnetostrictive performance.

5.5.1 Random texture

MMFEM simulations were carried out for randomly oriented polycrystalline $Fe_{83}Ga_{17}$, $Fe_{80}Ga_{20}$ and $Fe_{72.8}Ga_{27.2}$ alloys for comparison with the Akulov and Vladimirsky approximations in addition to experimental observations of sintered non-aligned $Fe_{80}Ga_{20}$ powder. Throughout all simulations, the grain structure was modeled using a 6x6x6 space-filling array of non-dimensional rhombic dodecahedrons to give a total of 666 grains when including off-raster interior grain sites. (Recall that the 2x2x2 array in Figure 5.3 contains 9 grains.) With 24 elements per grain, the total system included 15984 tetrahedral elements demarcated by 3425 nodes. Monte-Carlo techniques provided a random crystallographic distribution for use throughout multiple simulation runs as described previously in Section 5.4.2.1. Total strain calculations were based on 81 separate strain vectors distributed at one-half grain diameter intervals throughout the interior cross section of the crystal array. To accurately model the material's bulk strain response for interacting grains, these interior vectors lay at least one-grain diameter inside of the simulated material surface and joined nodes to within one-grain diameter of the material's opposing faces. These strain vectors were oriented parallel to the applied magnetic field direction, which lies in the global x-direction. Reported values in this direction are referred to by the "||" subscript.

Figure 5.5 summarizes the FEMM results for ten simulation runs for each of the three alloys using the material properties listed in Table 5.2. The first column of the figure shows histograms for tetrahedral elements with respect to the x-direction saturation magnetostriction developed by non-interacting grains. The upper and lower magnetostriction limits (i.e. λ_{100} and λ_{111}) are dictated by material properties for each stoichiometry while intermediate values arise due to deviations in crystallographic orientation from the <100> or <111> directions. The collocated arrows, marking the simulation mean values and Akulov approximations for magnetostriction, confirm that there is excellent agreement between this aspect of the numerical simulation and the analytic method.

The second column of Figure 5.5 shows histograms of the internal x-vectors' total strain distribution, their mean values, the Vladimirsky approximation and for the Fe-20Ga alloy, the range of experimental observations. In each case the mean strain value falls well below that of the Akulov approximation (value indicated in the left hand column) yet higher

than that of the Vladimirsky approximation. This reveals that elastic grain interactions significantly reduce the material's bulk magnetostrictive capability, although not as adversely as supposed by the Vladimirsky method. The experimental values of $(2/3)(\varepsilon_{tot,\|-\perp})$ for the sintered powder metal range from 40 to 51 $x10^{-6}$, which is in good agreement with the simulation mean result. Of the three stoichiometries examined, the Fe-27.2Ga alloy has the largest bulk magnetostrictive capability with $\varepsilon_{tot,\|} = 77\ x10^{-6}$. Should this material be tested as a disk under directionally applied fields or as a rod-shaped specimen under coaxial compressive loads and fields, one would expect the maximum magnetostrictive strain output of $\varepsilon_{tot,\|-\perp} = (3/2)\ \varepsilon_{tot,\|} = 116\ x10^{-6}$. Use of the (3/2) factor is appropriate given the isotropic bulk magnetostriction developed in a random texture. Valid use of the (3/2) factor was confirmed by additional simulation runs for $\varepsilon_{tot,\|-\perp}$.

The final column of Figure 5.5 shows histograms for the element count with respect to internal stress in the x-direction. On the whole, the compressive and tensile elemental stresses balance one another to give a mean stress equal to zero. However, the shape and magnitude of the stress distribution provide an indication of the level of grain interactions. Considering the Fe-17Ga result with $\varepsilon_{tot,\|} = 33\ x10^{-6}$, the indicated 7.2 MPa stress level at one standard deviation illustrates that two thirds of the grain elements are subjected to this or lower magnitude stress conditions. It follows that at two standard deviations, 95% of the grains experience less than 14.4 MPa magnitude stress levels. Comparing the Fe-20Ga case, the lower stress magnitude of 4.3 MPa at one standard deviation facilitates a 55% larger bulk magnetostrictive response of $\varepsilon_{tot,\|} = 51\ x10^{-6}$ despite the small 13% increase in $\lambda_{\|,s}$. The lower stress levels may in part be attributed to the smaller difference between λ_{100} and λ_{111} of 151 $x10^{-6}$ for Fe-20Ga compared to the difference of 216 $x10^{-6}$ for Fe-17Ga. Consistent with this trend, the Fe-27.2Ga alloy's stress magnitude is again larger, as is the difference between λ_{100} and λ_{111} which increases to 227 $x10^{-6}$. (Values for λ_{100} and λ_{111} were taken from Figure 2.4.) Undoubtedly, elastic anisotropy also plays a role in the grain interaction and ultimately the stress distributions. Although elastic anisotropy effects are automatically accounted for in the MMFEM, their influence is not easily separated from those of the magnetostrictive constants.

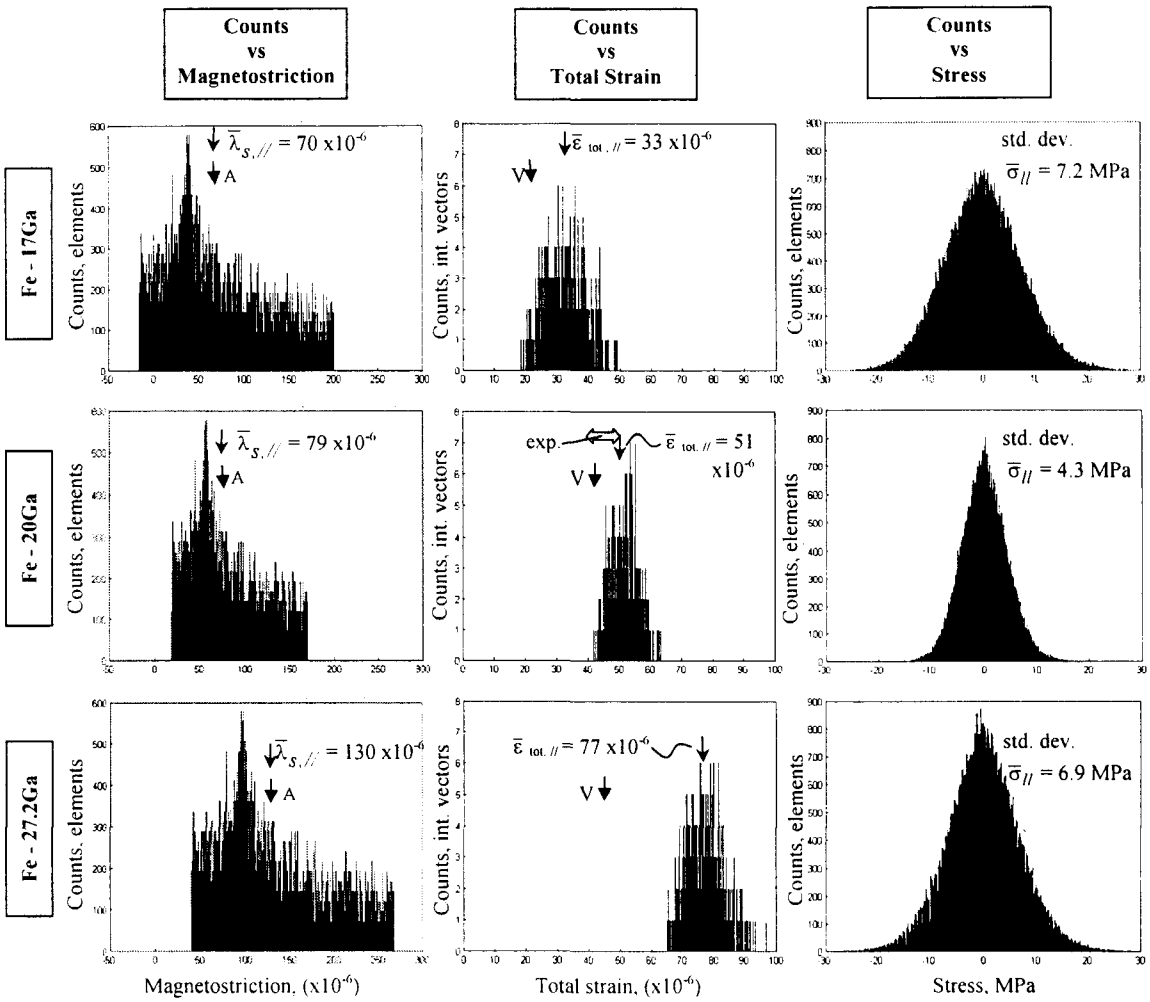

Figure 5.5 MMFEM Monte-Carlo simulation of randomly oriented Fe-Ga polycrystal having different stoichiometries. Histogram of magnetostriction, total strain and stress in the applied field direction. Total strain corresponds to the bulk magnetostrictive response when accounting for misaligned grain interaction. The "A", "V" and "exp." annotations correspond respectively to the Akulov and Vladimirsky approximations (Table 5.1) and experimental results (Section 2.3.3). (Note that histograms for magnetostriction and stress are based on 15984 element responses while total strain reflects the response of 81 x-direction vectors.)

	Magnetostriction Constants x10^{-6}		Elastic Constants, GPa		
	λ_{100}	λ_{111}	c_{11}	c_{12}	c_{44}
$Fe_{83}Ga_{17}$	200	-16	225	181	128
$Fe_{80}Ga_{20}$	170	19	170	136	119
$Fe_{72.8}Ga_{27.2}$	267	40	196	156	120

Table 5.2 Fe-Ga alloy material properties used in simulations. These properties reflect those of furnace cooled alloys.

5.5.2 [110] fiber texture

MMFEM simulations were used to investigate how crystallographic orientation deviations from a [110] fiber texture affect a $Fe_{83}Ga_{17}$ alloy's bulk magnetostrictive performance. Comparisons are made to the annealed-extruded $Fe_{83}Ga_{17}$ specimen, whose manufacture, crystallographic texture and magnetostrictive properties were previously described in Section 3.3.2.1. The grain structure was modeled using the 3-dimensional array of 666 rhombic dodecahedrons, where grain orientations were assigned using Monte-Carlo techniques to give a Gaussian distribution relative to the direction of strain measurement. The strain measurement direction was defined to be coincident with the extruded rod's longitudinal axis.

The net strain and stress response to an orthogonal change in applied field direction are shown in Figure 5.6. Each data point represents the combination of ten simulation runs for a particular Gaussian orientation distribution defined by the angular divergence from the [110] direction of the ideal fiber texture. The ideal [110] fiber texture, having zero angular deviation, consists of grains with their [110] direction parallel to the rod axis and a random rotational orientation about the longitudinal axis. As usual, the orthogonal change in applied field consists of a rotation into a final direction that is parallel with that of the direction of strain measurement. The net strain $\varepsilon_{tot,\parallel\text{-}\perp}$ of the bulk material (Figure 5.6a) is small and negative for the ideal [110] fiber texture. As the angular deviation defining the texture increases, the net strain increases to approach 50 $x10^{-6}$ for Gaussian distribution angles near 60°. This demonstrates that a strong [110] fiber texture is undesirable compared to one of a more random texture from the standpoint of achieving larger net strain outputs. The maximum net strain observed here is consistent with that of the random distribution simulations where $(3/2)\varepsilon_{tot,\parallel} = 49.5\ x10^{-6}$ based on Figure 5.5's value of $\varepsilon_{tot,\parallel} = 33\ x10^{-6}$. Offered for comparison, the net magnetostriction $\lambda_{\parallel\text{-}\perp}$ for non-interacting grains was also included in Figure 5.6a. The significantly larger strain values of $\lambda_{\parallel\text{-}\perp}$ emphasize that elastic interactions are an important factor limiting the bulk magnetostrictive response $\varepsilon_{tot,\parallel\text{-}\perp}$. Highlighted by the increasing level of internal stress (Figure 5.6b), these elastic grain interactions increase as the crystallographic orientations deviate further from the ideal.

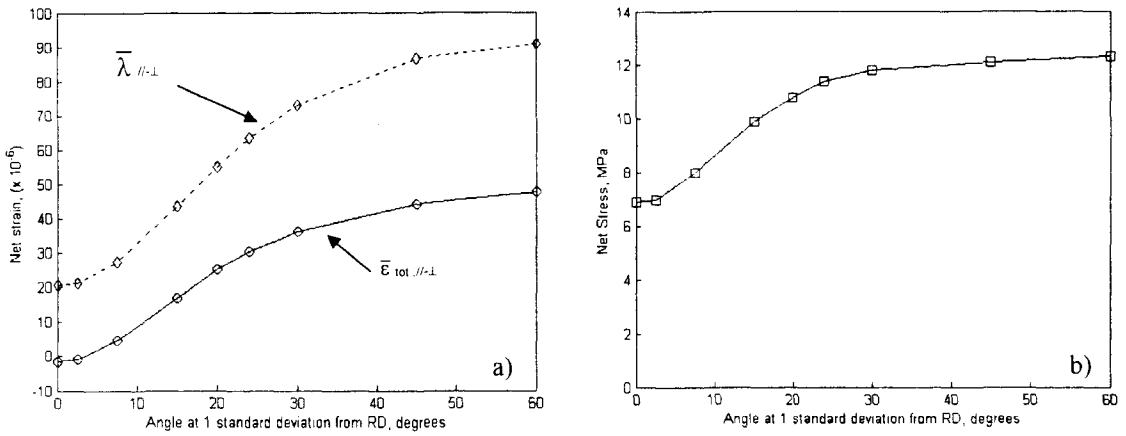

Figure 5.6 Ten-run summary for $Fe_{83}Ga_{17}$ fiber texture using MMFEM simulation response to 90° field rotation into direction of strain measurement. Abscissa reflects the angle at 1 standard deviation from an ideal [110] orientation: a) Net change in magnetostriction and total strain; b) Net stress level at 1 standard deviation. Material properties include: λ_{100} = $200x10^{-6}$, λ_{111} = $-16x10^{-6}$, c_{11} = 225, c_{12} = 181, c_{44} = 128 GPa.

A comparison of the experimental measurement of the annealed-extruded specimen with simulation results shows agreement for a 24° deviation in the Gaussian distribution angle. In this case $(3/2)\lambda_s$ and $\varepsilon_{tot,\|\text{-}\perp}$ are both approximately 30 $x10^{-6}$ for the respective experimental and simulated values. Examination of the specimen's pole plot (Figure 2.8) suggests that although the simulated texture distribution has been greatly over simplified, it is generally reasonable. Additional insights to the polycrystalline material's response may be gained by considering the 24° angular deviation simulation results. The histograms of Figure 5.7 show that a broad range of magnetostrictions, from $-30\ x10^{-6}$ to $300\ x10^{-6}$, would occur for non-interacting grains. Somewhat counterintuitive, the observed $\lambda_{\|\text{-}\perp} = -30\ x10^{-6}$ value is more negative than the material property $\lambda_{111} = -16\ x10^{-6}$. Further analysis using Equation 1.4 shows that this is indeed possible, for example, for off-axis rotations into the <112> direction. Despite the large range in grain magnetostrictions, elastic interactions constrain the total strain response $\varepsilon_{tot,\|\text{-}\perp}$ between $10\ x10^{-6}$ and $60\ x10^{-6}$. Coinciding with these strains, the net stress change may be as high as ±60 MPa with the range of stresses quantified by an 11.4 MPa value at one standard deviation.

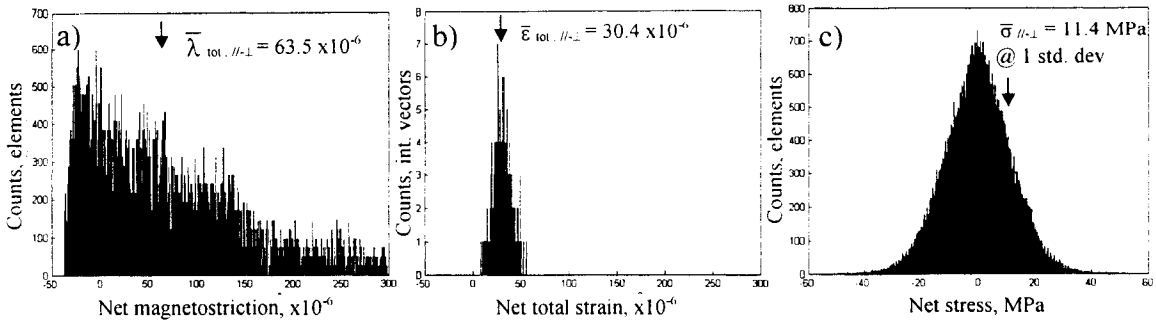

Figure 5.7 MMFEM simulation of $Fe_{83}Ga_{17}$ fiber texture with a Gaussian distribution defined by a 24° misorientation value at 1 standard deviation from an ideal [110] fiber orientation. Histograms of: a) Net-magnetostriction for non-interacting grains; b) Internal measurement vector of net-strain; c) Net-stress change. Note that histograms for magnetostriction and stress are based on 15984 element responses while total strain reflects the response of 81 x-direction vectors.

Although the annealed-extruded specimen's bulk strain response was in good agreement with the MMFEM simulation, the response of the non-heat treated extruded specimen is more difficult to reconcile. According to the OIM analysis (Figure 2.7), the non-heat treated extruded specimen also possessed a [110] wire/fiber texture, but its experimental strain response of $(3/2)\lambda_s = 60 \times 10^{-6}$ is twice as large as that of the annealed result. Considering that the simulated [110] fiber texture for $Fe_{83}Ga_{17}$ (Figure 5.6) gives a maximum net strain of $\varepsilon_{tot.||-\perp} \sim 50 \times 10^{-6}$, one could conclude that actual the crystallographic texture of the specimen is somewhat different than indicated.

5.5.3 Cold rolling texture

A comparison of a MMFEM simulation and experimental measurements was conducted on the fine-grained polycrystalline $Fe_{83}Ga_{17}$ specimen labeled R9 from Chapter 2. This specimen was produced by hot rolling of an as-cast ingot followed by warm rolling and finally by cold rolling to a final thickness of 0.10 mm. A disk-shaped specimen of the material was then annealed at 590 °C for 1 h in Ar to induce stress relief without secondary recrystallization. X-ray analysis indicated the presence of two predominant textures at the surface. The first texture, {001}<110>, comprises roughly 65% of the surface area with the second texture, {111}<211>, covering the balance. The angular deviation of grain

orientations from both textures was assumed to follow a Gaussian distribution with one standard deviation at 20°. The rolled material's grain geometry approaches a width to length to depth ratio of 50x500x1 with ~10-μm wide grains. The MMFEM of this material used simulated grains having a width to length to depth ratio of 4x12x1. However, solutions to MMFEM simulations using increasing length ratios converged quickly, verifying that the computationally cheap grain configuration of 4x12x1 should accurately represent the material's strain response.

Using the two texture distributions, ten simulations were conducted on a 6x3x4 matrix of grains. The strain responses over interior elements were used to minimize edge effects. Relative to the rolling direction, simulations gave $\varepsilon_{tot,\|-\perp} = 30 \times 10^{-6}$, and $\lambda_{\|-\perp} = 54 \times 10^{-6}$. The $\varepsilon_{tot,\|-\perp}$ result agreed with the 30×10^{-6} experimental result. Given the large {001}<110> texture content, simulations show that $\varepsilon_{tot,\|-\perp} \sim 157 \times 10^{-6}$ is expected at a angle of 45 degrees from RD, but the experimental observation of $\varepsilon_{tot,\|-\perp} = 37 \times 10^{-6}$ ppm in this direction is inconsistent with this result. This discrepancy suggests that a significant texture change occurs throughout the specimen's thickness or that the alloy's magnetostrictive characteristics have been significantly altered during processing.

5.5.4 Cube texture sensitivity analysis

A sensitivity analysis of a $Fe_{83}Ga_{17}$ polycrystal's bulk magnetostrictive output as a function crystallographic misorientation was performed to reveal how precise a texturing process must be to obtain high quality actuation/sensing material. MMFEM simulations were carried out for varying degrees of angular deviation from an ideal cube or {001}<100> texture. As was the case for the extruded and random specimen simulations, a 3-dimensional 666 grain array of rhombic dodecahedrons was used. Monte-Carlo techniques were employed to assign each grain its crystallographic orientation using a Gaussian distribution relative to the direction of strain measurement in addition to an independent Gaussian distribution relative to the plane normal. Separate number generator initializations ensured that each distribution was independent.

A summary of combined simulation runs (ten at each distribution deviation angle) includes averages of the net strain output $\varepsilon_{tot,\|-\perp}$, net magnetostriction $\lambda_{\|-\perp}$, and internal

stresses developed for orthogonal magnetic field changes. As shown in Figure 5.8a, the net strain is observed to fall off rapidly with increasing misorientation angles through ~ 18°, thereafter the loss in strain output declines at a decreasing rate to eventually approach that of a randomly oriented material. Comparing net strain output and net magnetostriction, the increasing difference between them indicates that grain interaction becomes more significant as grain misorientations increase. This is substantiated by the increase in net internal stress with angular misorientation as shown in Figure 5.8b.

Given as an example, if one were to seek a net stain output of 225 $x10^{-6}$ or better, the Gaussian distribution defining the grain orientations must be 12° or less at 1 standard deviation. Histograms of the simulation results for the 12° case (Figure 5.9) indicate that the net magnetostriction $\lambda_{\|\text{-}\perp}$ of the grains range widely between 0 and 300 $x10^{-6}$, however elastic grain interactions limit the bulk response to give a strain output $\varepsilon_{tot,\|\text{-}\perp}$ ranging from 201 $x10^{-6}$ to 258 $x10^{-6}$. In this case the respective net magnetostriction and mean net strain-output values are 263.1 $x10^{-6}$ and 228.5 $x10^{-6}$. Internal net stress magnitudes, generated by the magnetostriction, were simulated to be as high as 60 MPa for some grain elements, however ~ 2/3 of the grains experienced stress magnitude changes of 8.9 MPa or less as indicated by the value at 1 standard deviation. Although Fe-Ga texturing efforts will have to

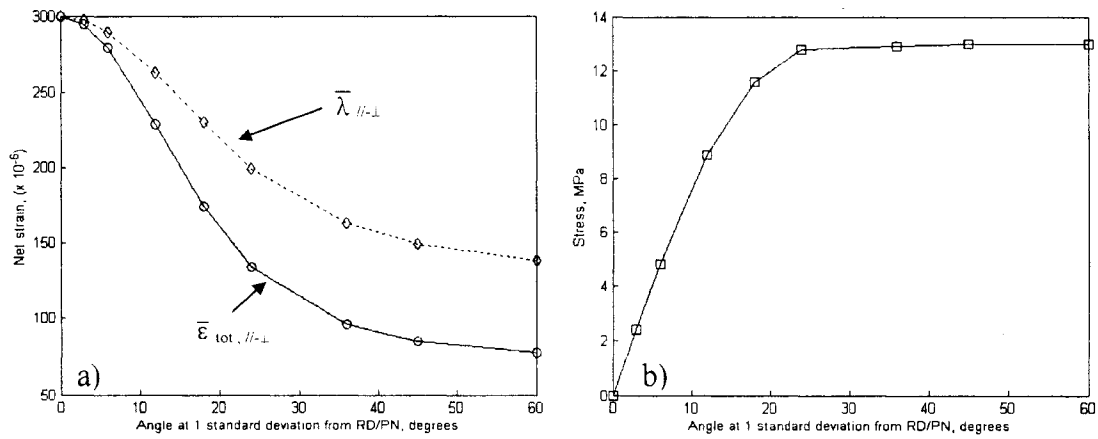

Figure 5.8 Ten-run summary for $Fe_{83}Ga_{17}$ cube texture using MMFEM for the simulated response to a 90° field rotation into direction of strain measurement. Abscissa reflects the angle at 1 standard deviation from ideal {001}<100> RD and PN orientations. a) Net change in magnetostriction and total strain; b) Net stress level at 1 standard deviation. Material properties include: $\lambda_{100} = 200x10^{-6}$, $\lambda_{111} = -16x10^{-6}$, $c_{11} = 225$, $c_{12} = 181$, $c_{44} = 128$ GPa.

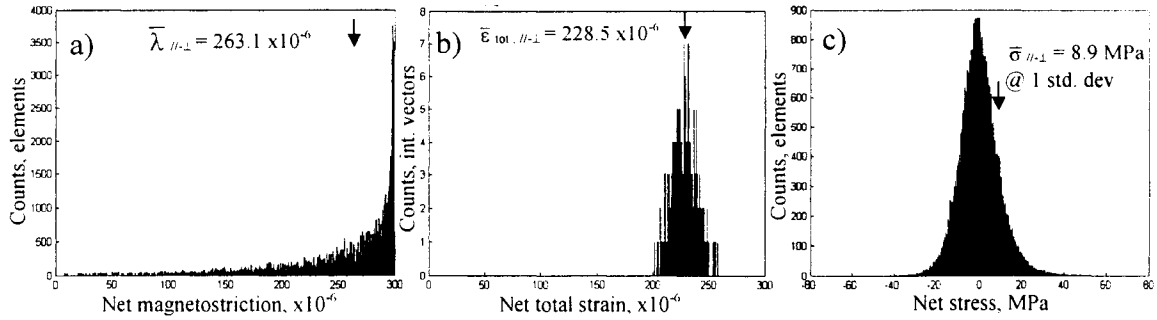

Figure 5.9 MMFEM simulation of $Fe_{83}Ga_{17}$ with a Gaussian distribution defined by a 12° misorientation value at 1 standard deviation from {001}<100> cube texture. Histograms of: a) Element net-magnetostriction for non-interacting grains; b) Internal measurement vector of net-strain; c) Element net-stress change.

achieve a high degree crystallographic alignment to give good strain performance, it is encouraging to that note cube orientation distributions tighter than 12° have been produced in the Fe-Si alloys [Walter 1965].

Exploring a variation on the cube texture, a simulation was conducted to examine the total strain output of a [100] fiber texture where the RD possesses a perfect [100] orientation and grain orientations relative to the PN are random. In this instance $\varepsilon_{tot,||-\perp} = \lambda_{||-\perp} = 300$ x10^{-6}, which is consistent with Equation 1.4 where grain interaction is neglected. In fact, simulation results show that the internal stresses developed by interacting grains remain small, being on the order of 0.01 MPa given their common alignment along the material direction containing the major magnetostriction constant λ_{100}. This result substantiates that a [100] fiber texture is just as good as the cube texture as far as magnetostrictive strain capability is concerned. However, the fiber texture will likely remain somewhat more difficult to magnetize as well as being more hysteretic given a mix of "hard" and "easy" axes in the PN direction.

5.6 Modeling summary

The MMFEM successfully captures the combined magnetostrictive and micromechanical response of polycrystalline Fe-Ga alloys. Simulation results were in good agreement with the experimental strain measurements for the $Fe_{80}Ga_{20}$ random, $Fe_{83}Ga_{17}$ rolled high-temperature anneal (with through thickness grains) and $Fe_{83}Ga_{17}$ annealed-

extruded specimens. In each of these cases, the specimen's crystallographic orientation distribution was well defined. Despite these satisfactory modeling results, simulated and experimental measurements were in poor agreement for the $Fe_{83}Ga_{17}$ rolled low-temperature annealed and $Fe_{83}Ga_{17}$ non heat-treated extruded specimens. The experimentally determined texture distributions for these two specimens were most likely not well characterized. In the former case, the X-ray texture analysis represented only the surface of the rolled sheet and the texture may have changed through the thickness. (This is in contrast to the well-known orientation for each of the through thickness grains in the high-temperature annealed rolled specimen.) In the later case, OIM analysis techniques were used. The discrete nature of OIM analysis could have led to systematic errors in which subtle yet important texture components were excluded.

The comparison of the total strain output of the MMFEM simulations, analytic approximation methods and experimental results for random specimens clearly indicated that the currently available analytic approximation methods are in disagreement. Depending on the alloy stoichiometry and consequently its material properties, assumptions of constant stress (Akulov method) lead to an over prediction of the total strain output by up to factor of two, while the spherical stress field (Vladimirsky method) and constant strain (Voigt method) approximations significantly under predict the total strain output.

Simulations addressing variations in grain misorientation from the ideal <110> fiber and ideal {100}<001> cube textures demonstrated that grain interactions can result in significant internal stresses, (magnitudes exceeding 40 MPa) which substantially limit the material's total strain output. As a result, the magnetostriction prediction for non-interacting grains consistently over predicts (in some cases by as much as a factor of two) the material's actual total strain capability.

Lending optimism to the success of future texturing efforts, the cube texture allows a reasonable margin of grain misalignment while still producing substantial bulk magnetostrictive strains. Adding further encouragement, the [100] fiber texture, provided it has a high degree of [100] alignment in the RD, sustains this bulk magnetostrictive strain capability equally well.

6. AUXETICITY AND ITS APPLICATIONS

Auxetic materials are characterized by their negative Poisson's ratios ν, in which an extension in the loading direction is accompanied by an extension in one or more directions transverse to that of the load application. This auxetic behavior contrasts with the positive Poisson's ratio behavior of conventional materials, which are often polycrystalline and isotropic in nature. A comparison of the Poisson's ratios for several conventional materials and auxetic materials are listed in Table 6.1.

A variety of "macroscopic" auxetic materials are prevalent including keyed brick structures, composites, skin, bone, polymeric foams, metallic foams and honeycombs. The auxetic behavior of these materials arises from the mechanical action of macroscopic geometries such as the reentrant cell structure of foam as depicted in the schematic of Figure 6.1. The list of known molecular auxetic materials, in which auxeticity is an intrinsic property, is significantly shorter and includes sintered ceramics, α-cristobalite, liquid crystalline polymers and a number cubic metals [Alderson 1999].

	Material	ν
Conventional	Rubber	0.50
	Polyurethane	0.45
	Steel	0.25 to 0.35
	Foam plastic	0.2
	Cork	0
Auxetic	Reentrant foam plastic[1]	-0.25
	Anisotropic cross-ply composite[2]	0 to -1.0
	$Fe_{72.8}Ga_{27.2}$ single crystal	-0.75

Table 6.1 Poisson's ratios for conventional and auxetic materials [1][Lakes 1988], [2][Gibson 1994].

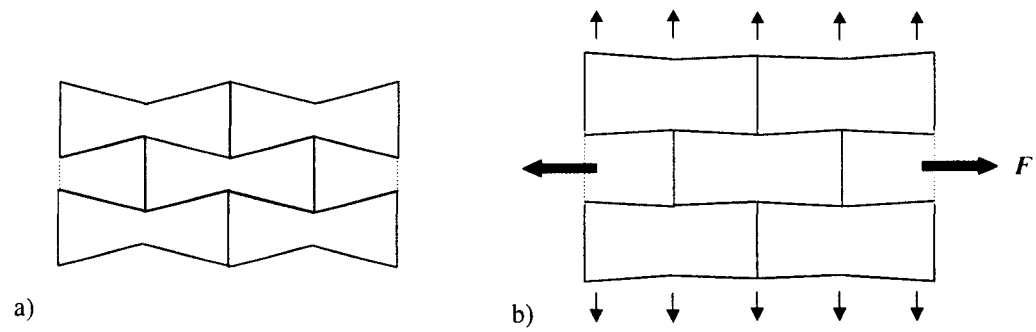

Figure 6.1 Two-dimensional representation of reentrant foam exhibiting auxetic material behavior: a) Unloaded; b) Uniaxial tensile load F producing longitudinal and transverse expansions.

Of these auxetic materials, the behavior of cubic metals and in particular Fe-Ga alloys is focused upon next. Their auxetic properties combined with high strengths and stiffness, compared to foam and biological materials offer a broad design scope for structural as well as functional applications. The "in-plane" auxetic characteristics of BCC materials are reviewed first. Several proposed applications are then explored that capitalize on material changes in one or more dimensions. These applications are presented as concepts to spur new research and development.

6.1 In-plane auxetic properties

Discussed in the theoretical elastic treatment of Section 1.5.2 and observed in the experimental elastic measurements of Sections 4.1.4 and 4.2, the Fe-Ga alloys exhibit in-plane auxetic behavior. These materials produce a transverse expansion in a dimension normal to an applied tensile load in one particular plane (a negative Poisson's ratio), while a contraction is produced normal to this plane (a positive Poisson's ratio). The schematic of Figure 6.2a depicts this response for the [110] loading of a (001) plane. This loading direction and plane exhibit the maximum auxeticity for cubic materials [Rovati 2002].

The in-plane auxetic response reflects a high degree of elastic anisotropy, which may be found in certain single crystal and highly textured polycrystalline materials. A number of metals and alloys exhibit in-plane auxetic behavior including Cu, CuZn, CuBe, Co, Ni, Li, Na, K, Fe, and FeAl among others. (see Table 4.6 for values). From observations made in

this research, FeGa alloys currently exhibit the largest known magnitudes of elastic anisotropy and auxeticity of any metal. Table 4.5 demonstrated increasing magnitudes with increasing Ga substitution levels to give A = 19.9, $\nu_{[1\bar{1}0]}$ = -0.75 and $\nu_{[001]}$ = 1.64 for a [110] loading condition in single crystal $Fe_{72.8}Ga_{27.2}$. For comparison, a survey by Jain *et al.* lists the next largest in-plane auxetic response for Li with A = 9.2, $\nu_{[1\bar{1}0]}$ = -0.55 and $\nu_{[001]}$ = 1.3 [Jain 1990].

A model for the in-plane auxetic behavior in BCC metals was proposed by Baughman *et al.*, in which the material response is governed by the pair-wise interaction of neighboring atoms [Baughman 1998]. Although other theories exist for auxeticity (such as Jain's electron gas model [Jain 1990]), Baughman's model is useful for visualizing the phenomenon. A schematic for this model is depicted in Figure 6.2b for two adjacent BCC unit cells where the plane formed by atoms 1, 3, 5 and 6 lie in a (001) plane. Collinear with the force F, a [110] tensile loading direction includes the 1 and 3 numbered atoms. As the tensile load is increased, atoms 2 and 4 are drawn towards one another through their nearest-neighbor interactions with atoms 1 and 3. This generates a negative strain in the [001] direction (a positive Poisson's ratio). In response to the decrease in the 2 - 4 atomic spacing, nearest-neighbor interactions cause the distance between atoms 5 and 6 to increase, thereby generating a positive strain in the [1 $\bar{1}$ 0] direction (a negative Poisson's ratio).

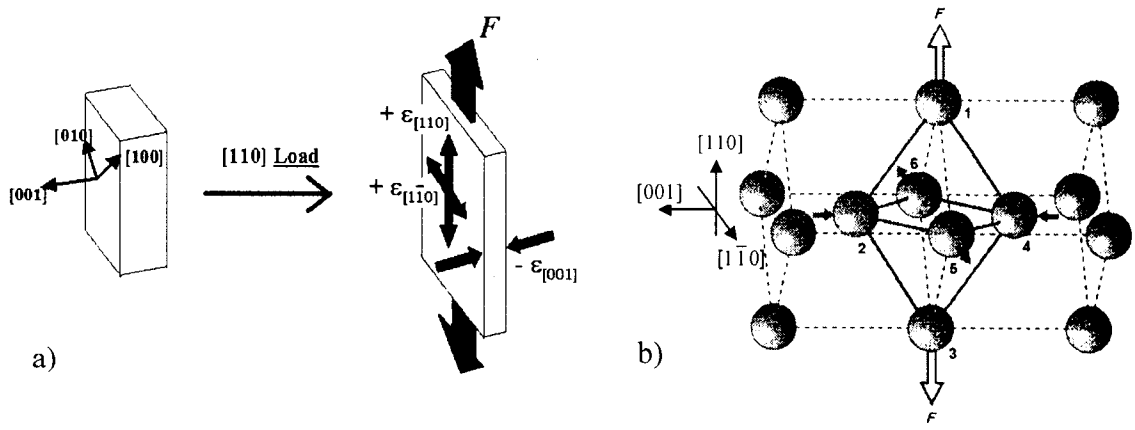

Figure 6.2 a) Schematic of in-plane auxetic response to uniaxial tensile loading; b) Schematic of two BCC unit cells undergoing tensile loading by force F to yield in-plane auxetic behavior through nearest neighbor-atomic interactions (solid lines). After [Baughman 1998].

6.2 In-plane auxetic applications

Novel engineering applications fulfilling combined functional and structural purposes are possible utilizing mechanically robust in-plane auxetic materials such as the Fe-Ga alloys. Recalling the results of Chapter 4 for the [110] loading direction in $Fe_{83}Ga_{17}$ single crystal: σ_{yield} = 450 MPa, $E_{[110]}$ = 160GPa, $\nu_{[1\bar{1}0]}$ = -0.37 and $\nu_{[001]}$ = 0.45. These mechanical properties provide an order of magnitude increase in yield strength and stiffness compared to auxetic polymeric and metallic foams and will facilitate the material's use in a structural capacity. However, successfully exploiting the in-plane auxetic properties will require using the proper crystallographic orientation of single crystals and highly textured polycrystalline alloys. The applications to be discussed next, including fastening devices, pumps and enhanced sensors, exploit the combined properties of in-plane auxeticity, strength and high stiffness.

6.2.1 Fastening devices

The performance of friction-fit fastening devices could be significantly improved using in-plane auxetic materials. A two-dimensional finite-element analysis by Shilko examined the tangential friction force developed by the interference fit of a slider in its casing as a function of the slider's Poisson ratio [Shilko 1995]. Distinguishing the problem formulation, the normal force and contact area between the slider and casing are not known in advance due to localized changes in tangential force with changing tensile load on the slider. Consequently, an iterative computational approach was taken with incremental changes in tensile load. A plot of the simulation result (Figure 6.3) shows the tangential load as a function of slider displacement for various Poisson's ratios between -0.9 and 0.4. The tangential load at impending slip for ν = -0.9 was over double that of the ν = 0.4 case. Additional modeling of self-locking friction-fit interfaces using negative Poisson ratio materials are discussed in [Shilko 1996] and [Kinkaid 2002]. The latter work employs a one-dimensional model of an axisymmetric press-fitted joint where a boundary value formulation of the problem is solved numerically.

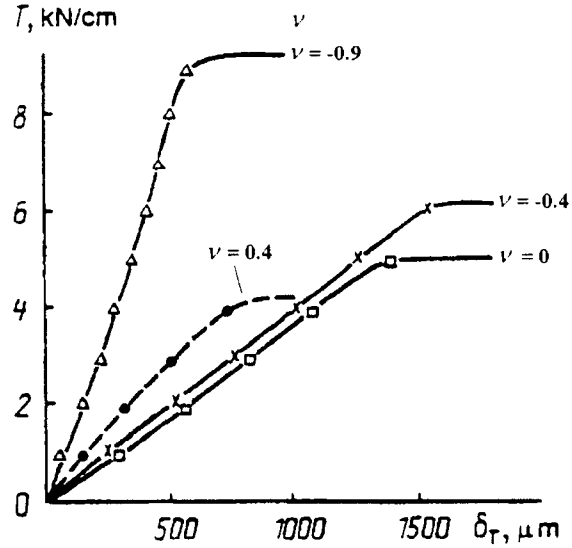

Figure 6.3 Tangential load T of a slider in its case as a function of displacement δ_T for various Poisson's ratios. Results determined by two-dimensional finite element simulation of an anisotropic cross-ply composite [Shilko 1995].

Monolithic components using in-plane auxetic materials such as the Fe-Ga alloys could be designed to produce interference fits. These components could be assembled using light compressive loads yet be bound tightly together by friction when placed under tension as shown in the schematic of Figure 6.4. Fundamental to the device's operation, as the in-plane auxetic fastener is compressed longitudinally along the [1 1 0] direction during insertion, its lateral dimension in the $[1\,\bar{1}\,0]$ direction contracts from width (A) to (A′) thus allowing it to slip more easily into the receptacle's gap of width (B). The receptacle could be made from either a non-auxetic material or alternatively from an auxetic material oriented to allow the gap width to expand during fastener insertion. As a consequence of compressive loading during insertion, the fastener increases in thickness from (C) to (C′) since the material's has a positive Poisson ratio in this direction. The expansion in thickness, however, is not detrimental to the fastener's proper function. If an attempt is made to pull the fastener and receptacle apart, the tensile load causes the fastener to try and expand laterally to width (A″). Since the receptacle impedes this lateral expansion, the normal force rises and the resulting friction force between them increases, thus limiting slip.

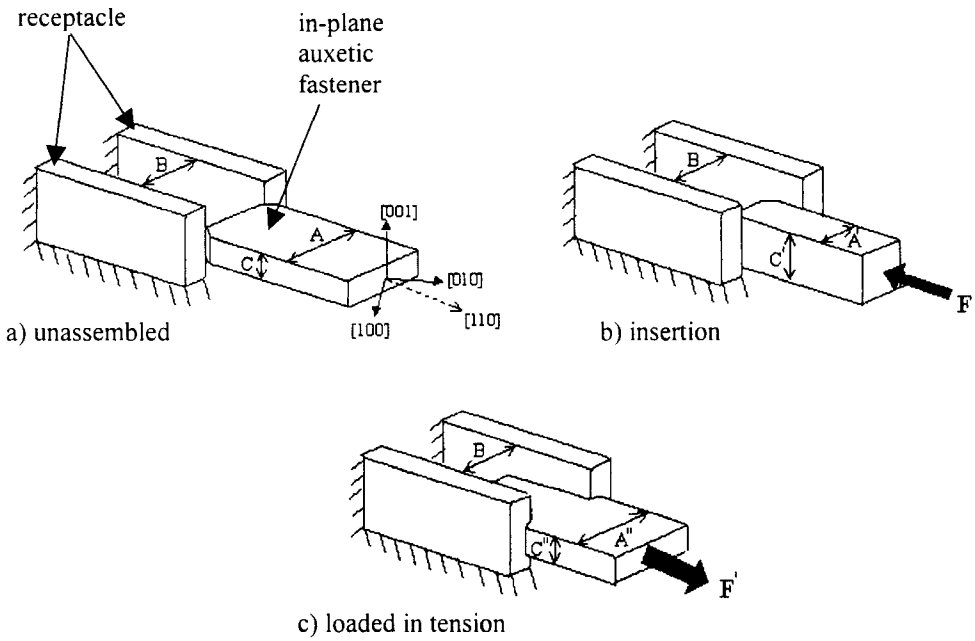

Figure 6.4 Fastening device using an in-plane auxetic component (fastener) and non-auxetic material (receptacle). a) Unmated components prior to assembly with the crystallographic orientation indicated; b) Strained fastener resulting from compression during insertion under load F; c) Installed fastener resisting pullout by tensile load F'. Note that $F' > F$ at impending slip.

Fastening applications could also capitalize on the interference fit of tube structures where mating tubes would be made to press easily together (by hand for instance) but refuse to pull apart. This concept would utilize a rigid receptacle (or one that decreases in diameter with tensile loading) and a male fastener component that increases in diameter under tensile loading. The male fastener would take the form of a tube constructed from oriented polycrystalline in-plane auxetic sheet. The fabrication of such a tube is depicted in Figure 6.5 where opposing edges of a thin {001}<110> oriented sheet are bonded to form a right cylinder. The material's [110] direction is parallel with tube's longitudinal axis and the material's [001] axis lies in the tube's radial direction. Axial tensile loading of the tube results in positive strain in the sheet's $[1\bar{1}0]$ direction, which in turn increases the tube's circumference and ultimately increases the tube's diameter. Accompanying the circumferential increase, the sheet thickness would decrease due to negative strain in the [001] direction. Provided that ratio of the tube diameter to the sheet thickness is large enough a net diameter increase would still be achieved.

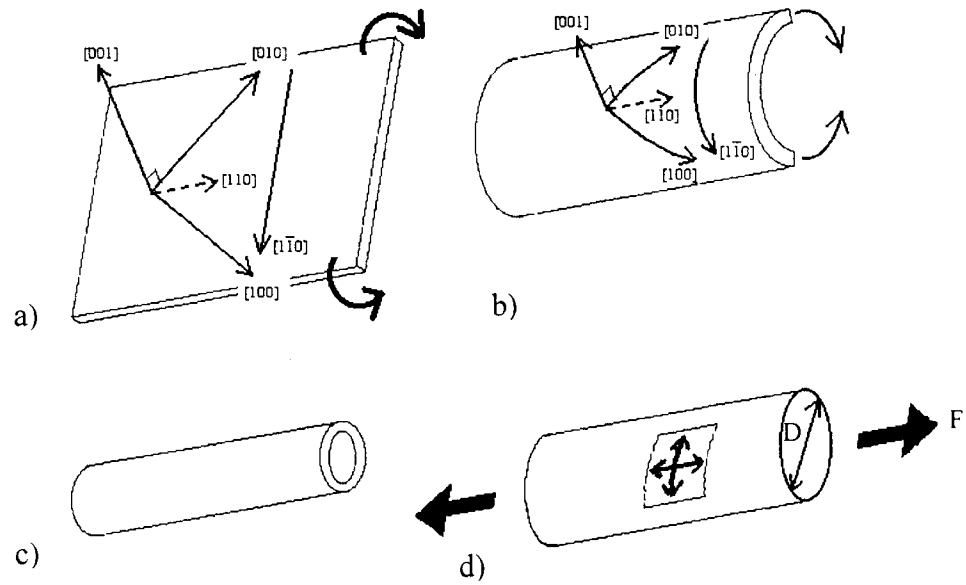

Figure 6.5 Auxetic tube formed from bending of a thin in-plane auxetic polycrystalline sheet. a) {001}<110> oriented sheet b) Sheet before edges are bonded. c) Finished tube. d) Finished tube under axial tensile load where arrows indicate positive longitudinal and circumferential strains to give increase in diameter D.

6.2.2 Solid-state pump

A solid-state pump (Figure 6.6) might also be constructed using the auxetic tube, (made from {001}<110> Fe-Ga sheet as described in the previous section). The auxetic tube would act as a diaphragm-like enclosure for producing volume and pressure changes. Directional fluid flow would be generated provided that the ends of the tube are sealed with one-way check valves. To actuate the pump, two rod-shaped magnetostrictive drive element (such as an [100] longitudinally oriented Fe-Ga alloy) and solenoids could be used to impose a tensile load on the tube. Under tension, the tube's length and diameter increase to provide a volume increase for generating the pump's intake stroke. Next, releasing the applied tensile load would allow the tube to contract elastically against the enclosed fluid to produce the output pressure stroke. This type of pump has the potential to produce high-pressure outputs and may prove to be extremely robust since there are no moving parts aside from the check valves. If the in-plane auxetic sheet forming the tube is made from a ferromagnetic alloy (such as Fe-Ga), the auxetic tube itself could be part of the magnetic circuit for the magnetostrictive actuators.

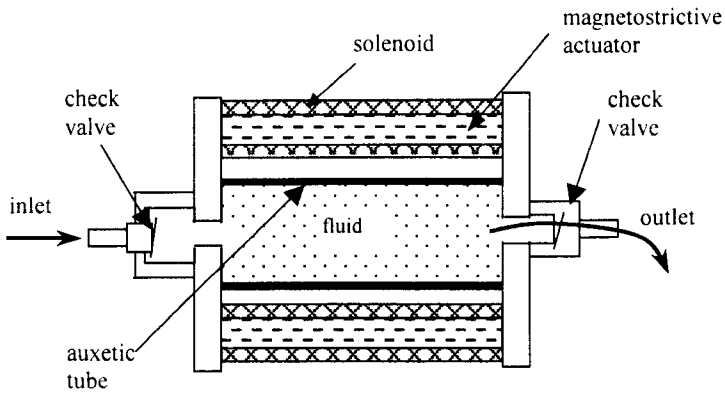

Figure 6.6 Cross section of a solid-state pump using auxetic tube and magnetostrictive drive elements.

6.2.3 Useful area change

The in-plane auxetic behavior allows for the surface area of a material to change in an unconventional fashion. Under tensile loading the in-plane auxetic sheet undergoes simultaneous longitudinal and lateral extensions to produce a significant area increase. This response is evident by considering a rectangular sheet of length L and width W, which has an original surface area $A = LW$. Subjecting the sheet to tensile loading along its length results in the sheet's new area A':

$$A' = L(1 + \varepsilon_L)W(1 + \varepsilon_T)$$

where ε_L and ε_T are the longitudinal and transverse strains along the direction of L and W respectively. Substituting for the Poisson's ratio $\nu = -\varepsilon_T/\varepsilon_L$ and discarding second order terms, the fractional area change becomes:

$$\frac{A' - A}{A} = \varepsilon_L(1 - \nu) \tag{6.1}$$

A calculation for a {001}<110> oriented $Fe_{72.8}Ga_{27.2}$ single crystal with ν = -0.75 and for steel with ν = 0.3, using Equation 6.1, gives results of their respective fractional area changes as $1.75\varepsilon_L$ and $0.7\varepsilon_L$. In other words, the in-plane auxetic Fe-Ga alloy sheet increases in area by a factor of $0.75\varepsilon_L$ and the steel sheet decreases in area by a factor of $0.3\varepsilon_L$. In this case, the

in-plane auxetic material clearly gives a larger areal response (2.5 times larger) and one of opposite sign relative to that undergone by the traditional engineering metal.

Applications that might take advantage of the areal increase of in-plane auxetic sheet include force and pressure sensors having improved sensitivity. It may also be possible to bond the in-plane auxetic sheet to piezoelectric material to form a composite with improved coupling coefficients and enhanced sensing capability. Additionally, if a ferromagnetic in-plane auxetic material is used (such as the Fe-Ga alloys), force and pressure changes could be sensed magnetically through changes in the materials' state of magnetization.

6.2.4 Other possibilities

The transmission of sound and vibration in structures are governed by the mechanical properties of the transmission material and its boundary conditions. Novel applications using in-plane auxetic materials could capitalize on their high degree of elastic anisotropy and internal magnetic/mechanical coupling. Applications using tailored sound and vibration transmission properties could offer improved sensing/transmission devices as well as variably damped structures and components through magnetic control. Applications using the in-plane auxetic metals can also function in a higher frequency regime compared to auxetic polymers, polymeric foam and metallic foams due to their larger modulus of elasticity.

6.3 In-plane auxetic application summary

Single and/or polycrystalline materials possessing in-plane auxetic behavior, such as the iron-gallium alloys, provide unique and novel solutions to a range of engineering applications. These solutions rely on combined material characteristics of high strength, stiffness and in-plane auxeticity, which cannot be found in current polymeric or metallic auxetic foams or traditional engineering metals. Broad classes of engineering applications to be addressed include: easily assembled, high-strength self-locking fastening devices; simple geometries providing useful area and/or volume change that act as solid-state pumps and sensors; and structures and sensors with unique high frequency sound, vibration transmission and damping characteristics.

7. CONCLUSIONS

The goal of this research was to increase the understanding of Fe-Ga alloys' magnetic, magnetostrictive and mechanical properties and apply this knowledge to advance the material's development and function in crystallographically textured polycrystalline forms for combined transduction and structural applications. In pursuit of this goal, the existing base of research knowledge was drawn upon to provide a guide for subsequent material processing, characterization, modeling and conceptualization of new applications.

A review of existing work (Chapter1) provided background information pertaining to the magnetic and mechanical properties of Fe-Ga alloys. This included the magnetization and magnetostrictive processes of ferromagnetic materials along with equations describing the anisotropic magnetostrictive response of single crystals to saturating magnetic fields. The latest theory characterizing the source of Fe-Ga alloys' magnetostrictive nature was reviewed, as well as descriptions of the material's variation in magnetostrictive capacity as a function of Ga substitution level and heat treatment. The known effects of grain morphology on the elastic and plastic properties of BCC metals were examined, as they are important factors in the development and use of textured polycrystalline forms of the alloy. Given the similarity of Fe-Al and Fe-Si alloy mechanical characteristics to those of the Fe-Ga alloys, a survey of proven Fe-Al and Fe-Si alloy crystallographic texturing methods was conducted to provide guidelines for texturing efforts in Fe-Ga alloys. The background review concluded with an analysis of cubic-crystal elasticity relationships to provide a foundation for modeling the magnetoelastic interactions anticipated in polycrystalline Fe-Ga alloys.

Various methods of material processing were undertaken to maximize the magnetostrictive output of polycrystalline Fe-Ga alloys using techniques intended to impart a high degree of [100] crystallographic texture (Chapter 2). Magnetic and mechanical characterization were carried out for textured material produced using directional growth, deformation processing and magnetically aligned powder metallurgy techniques. Of these approaches, from the standpoint of magnetostrictive performance, the two most successful approaches to texturing of polycrystalline alloy ($Fe_{83}Ga_{17}$) were directional solidification and rolling with a post-rolling high-temperature anneal. Directionally solidified and annealed rolled specimens gave respective net magnetostriction results of 170 $x10^{-6}$ and 160 $x10^{-6}$.

However, additional improvement in texturing is desired since the $Fe_{83}Ga_{17}$ textured magnetostrictive results give only ~ 55% that of [100] oriented single crystal $Fe_{83}Ga_{17}$, which has a net magnetostriction of 300 $x10^{-6}$. Further grain refinement is also needed as both specimens possessed large grains that were susceptible to intergranular brittle failure. Other processing results include: extruded rod, which was mechanically robust but possessed a dominant <110> longitudinal texture with net magnetostrictions limited to only 30 $x10^{-6}$ to 60 $x10^{-6}$; hot and cold forged specimens with modest texture development and low net magnetostrictions of ~ 35 $x10^{-6}$, this might be improved with larger deformations; cold rolled sheet with good ductility and high strengths, but containing mixed {001}<110> and {111}<211> surface textures with low net magnetostrictions of ~ 30 $x10^{-6}$; and sintered magnetically "aligned" <20-μm powder, which retained a random texture with net magnetostrictions of only 60 $x10^{-6}$ to 76 $x10^{-6}$.

Select single-crystal and polycrystalline Fe-Ga specimens were subjected to quasi-static magnetic testing to quantify the effects of stress and temperature on their magnetostrictive performance (Chapter 3). The magnetic response of $Fe_{81.0}Ga_{19.0}$ single crystal was well behaved over a -21°C to 80°C temperature range where the maximum magnetostriction and magnetization results decreased monotonically by 12% and 3% with increasing temperature from their respective maximum values of 340 $x10^{-6}$ and 1313 kA/m at -21°C. Achieving near-maximal magnetization and magnetostriction values required low-applied magnetic fields of only ~ 400 Oe for compressive stress conditions up to 87.1 MPa. Constant temperature tests showed that compressive stresses greater than 14.4 MPa were needed to achieve the maximum magnetostriction. Minor-loop cyclic magnetic field tests, at room temperature, established that the single crystal generates magnetostrictions of ~ 200 $x10^{-6}$ with good linearity and low hysteresis for compressive stresses up to 87.1 MPa using a 30 Oe amplitude AC field superimposed on a bias field of 150 Oe. The room temperature magnetization response of the directionally solidified specimen (at a 14.4 MPa compressive stress) was very similar to that of the single crystal. Under the same conditions however, the extruded and extruded plus annealed specimens exhibited greater magnetic anisotropy due to the presence of misoriented grains having magnetically hard axes in the direction of the applied magnetic field. These unfavorable grain orientations likely include <110> and <111>

texture components. Magnetization trends were corroborated by the magnetostriction measurements whose values were 170 $x10^{-6}$, 60 $x10^{-6}$ and 30 $x10^{-6}$ for the directionally solidified, extruded and extruded plus annealed specimens respectively.

The $Fe_{81.0}Ga_{19.0}$ single crystal was also subjected to major-loop cyclic stress testing under various levels of DC magnetic field (Chapter 3) to characterize its magnetomechanical properties for use in actuation and sensing applications. Analysis of the stress versus strain response demonstrated a maximum delta-E effect of 104%, where a soft modulus of 28 GPa coincided with maximum magnetic moment rotation and a stiff modulus of 57 GPa reflected elastic behavior with limited magnetic moment rotation. Stress-induced magnetization changes gave a maximum sensitivity of $d^*_{33} \sim 22.5$ tesla/Pa over a 20 MPa stress range. Optimizing this sensitivity for sensing applications will require the proper choice of combined DC applied magnetic field and stress.

Single-crystal specimens of $Fe_{83}Ga_{17}$ having {001}<100> and {001}<110> orientations were tested in tension at room temperature to evaluate the alloy's mechanical properties (Chapter 4). These tests revealed that {110}<111> and {211}<111> slip occurred at respective critical resolved shear stresses of 220 and 240 MPa. Depending on crystal orientation, yielding began at 0.3% to 0.8% elongation for yield stresses of 450 to 515 MPa and continued through ~ 2% without failure. Slip was discontinuous in the {001}<100> oriented sample and first occurred at a maximum stress of 515 MPa. The ultimate tensile strength of the {001}<110> specimen was 580 MPa. The results for the active slip systems, shear stresses and yield strengths provide insight to the possible development of texture in polycrystalline forms of the Fe-Ga alloys and will guide their use in combined transduction and structural applications.

Tensile testing also quantified the $Fe_{83}Ga_{17}$ single crystals' elastic properties (Chapter 4), which revealed a high degree of mechanical anisotropy. The Young's modulus was 160 GPa for loading in the [110] crystal direction with a Poisson's ratio of -0.37 on the (001) major face, while a Young's modulus of 65 GPa was observed for loading in the [100] crystal direction with a Poisson's ratio of 0.45 on the (001) major face. The combined effect of these Poisson's ratios is to generate an in-plane auxetic behavior. The corresponding elastic constants are $c_{11} = 225 \pm 20$ GPa, $c_{12} = 181 \pm 20$ GPa and $c_{44} = 128 \pm 2$ GPa with an

elastic anisotropy of 5.7. An analysis of elastic constants of other Fe-Ga stoichiometries (from other researchers' acoustic measurements) identified a significant in-plane auxetic behavior with a minimum Poisson's ratio of -0.75 and elastic anisotropy value of 19.9 for single-crystal $Fe_{72.8}Ga_{27.2}$. The magnitudes of the intrinsic elastic anisotropy and negative Poisson's ratio values are the largest of any material known to date. Further analysis of the elastic properties for various stoichiometries revealed highly-correlated quadratic relationships between the Poisson's ratios with respect to the level of Ga substitution in Fe. A similar observation in the Fe-Al alloy system substantiates the likelihood of a physical basis for these correlations, which deserves further investigation.

Tensile testing of a fine-grained cold-rolled $Fe_{83}Ga_{17}$ polycrystalline specimen was conducted (Chapter 4) to further explore the material's elastic and plastic properties for use in harsh mechanical environments. Yielding began at 0.4% elongation and 600 MPa, while the ultimate tensile strength was 840 MPa for elongations reaching at least 1.5%. Although the net magnetostriction of this specimen was low (~30 $x10^{-6}$ reported in Chapter 2), these tensile test results provide confirmation that a fine-grained polycrystalline Fe-Ga alloy has sufficient ductility and strength for use as a rugged transduction material.

A magnetostrictive micromechanics finite-element model (MMFEM) was successfully developed and used to capture the combined magnetostrictive and micromechanical response of polycrystalline Fe-Ga alloys to saturating magnetic fields (Chapter 5). Simulation results were in good agreement with the experimental strain measurements for random, rolled (with through thickness grains) and annealed-extruded specimens. In each of these cases, the specimen's crystallographic orientation distribution was well defined. Although simulated and experimental measurements were in poorer agreement for the rolled low-temperature annealed and non heat-treated extruded specimens, this was very likely due to a deficiency in knowledge of their texture distributions. A comparison of the total strain output of the MMFEM simulations, analytic approximation methods and experimental results for random specimens clearly indicated that the analytic approximation methods are in disagreement. Assumptions of constant stress lead to an over prediction of the total strain output by up to factor of two, while the spherical stress field and constant strain approximations under predict the total strain output.

A sensitivity analysis addressing variations in grain misorientation from an ideal cube texture in a $Fe_{83}Ga_{17}$ alloy demonstrated that grain interactions generate internal stresses with magnitudes exceeding 40 MPa, which substantially limit the material's total strain output. There is cause for optimism regarding the success of future texturing efforts. Simulations show that an imperfect cube texture having up to a 12° margin of grain misalignment (relative to ideal) will still produce bulk magnetostrictive strains of ~ 225 $x10^{-6}$ (75% of the maximum for $Fe_{83}Ga_{17}$). Adding further encouragement, a [100] fiber texture having a high degree of alignment in the actuation direction (i.e. alignment of grains' [100] crystallographic direction along the axis of actuation with random orientations of the grains [001] crystal direction about that axis), sustains this bulk magnetostrictive strain capability equally well.

The identification of a large-magnitude negative Poisson's ratio and hence the in-plane auxetic behavior in elastically anisotropic metals such the Fe-Ga alloys has expanded the potential design envelope beyond that of existing engineering and transduction materials. In-plane auxetic behavior provides unique and novel solutions to a range of engineering applications, which rely on combined material characteristics of high strength, stiffness and in-plane auxeticity that cannot be found in current polymeric or metallic auxetic foams or conventional engineering metals. Broad classes of engineering applications were addressed (Chapter 6) including self-locking fastening devices and simple geometries that provide useful area and/or volume change for use as solid-state pumps and sensors. Structures and sensors with unique high-frequency sound, vibration transmission and damping characteristics are also possible.

To summarize several important aspects of this work with respect to future directions:

- Fe-Ga alloys exhibit excellent transduction capabilities, unique auxetic behavior and robust mechanical attributes. Achieving the material's maximum utility and its widespread use in diverse applications will require the production of textured polycrystalline forms in sufficient quantities for commercialization. To this end, future work should pursue improving the crystallographic texturing methods having the potential for high yield outputs. Promising approaches include directional

solidification and rolling, although a fine grain structure must be retained to achieve the best mechanical performance.

The MMFEM proved successful in simulating the combined magnetostrictive and micromechanical behavior for saturation magnetization conditions in polycrystalline Fe-Ga alloys. However, the model has the potential to facilitate the future development as well as expand the study and understanding of magnetostrictive materials. The model could be extended to account for inhomogeneous stoichiometric distributions and crystallographic phase variations as well as accommodating an unlimited range of grain morphologies. Although it would be a challenging undertaking, the regime of non-saturation magnetization and magnetostriction responses could also be addressed by allowing system energy (including applied field, magnetocrystalline and elastic anisotropy and irreversible losses) to dictate the material's magnetic domain structure while accounting for the material's three-dimensional crystallographic attributes. Such a model would allow the transduction response to be predicted for magnetostrictive materials having any size, shape and crystallographic structure for any level of applied magnetic field and stress.

APPENDIX A: ROLLING PROCEDURE

The following schematic describes the rolling-deformation processing of a $Fe_{83}Ga_{17}$ cast ingot. The procedures included hot, warm and cold rolling to yield the specimens referred to in Chapter 2-7. The following label conversions were used for quoting the rolling specimens in the main text of the dissertation.

Dissertation	Schematic	Dissertation	Schematic
R1	B0	R6	B9A
R2	B2	R6	B9A_7
R3	B5_1	R6	B9A_6
R4	B3_2	R7	B7_4
R5	B4	R7	B7_2

all measurements in inches
all temperatures in degress C

	deg.C	deg. Kelvin
Tmelt	1450	1723

cast ingot	width	length	thickness
in oxidized stainless steel 304 can	2.0	2.0	0.375
sealed in argon atmosphere			

- seal in stainless 321 (preoxidized @ 900C) can, backfilled with argon and evacuated
- hot soak at 1000 deg. C for 30 min, argon flow over can - 4 liter/min by O2 calib.
- hot roll 55.5 % reduction rollers @ 300 deg.C and 22.5 fpm
  reduced in 72 passes, rollers set in 0.003"/pass, reheat @ 1000 for 6 min every 3 passes
- remove can

rolled thick plate	width	length	thickness
	2.4	3.5	0.167

- section width into two equal pieces with diamond band saw
- section length into two equal pieces
- trimmed rolled product to give plates B, D, E,F; corners saved as coupon **A1**
- remove contaminants with 50/50 HCl/H2O plus H2O2

coupon **A1**
trimmed pieces hot rolled thick plate
thickness 0.167

sectioned thick plate **B**

width	length	thickness
1.125	1.63	0.167

Nishihara proc. @ 700 deg.C

Nishihara texturing process, Patent# 3,279,960 (designed for 2-6%wt Al) revised 1/18/02 page B1

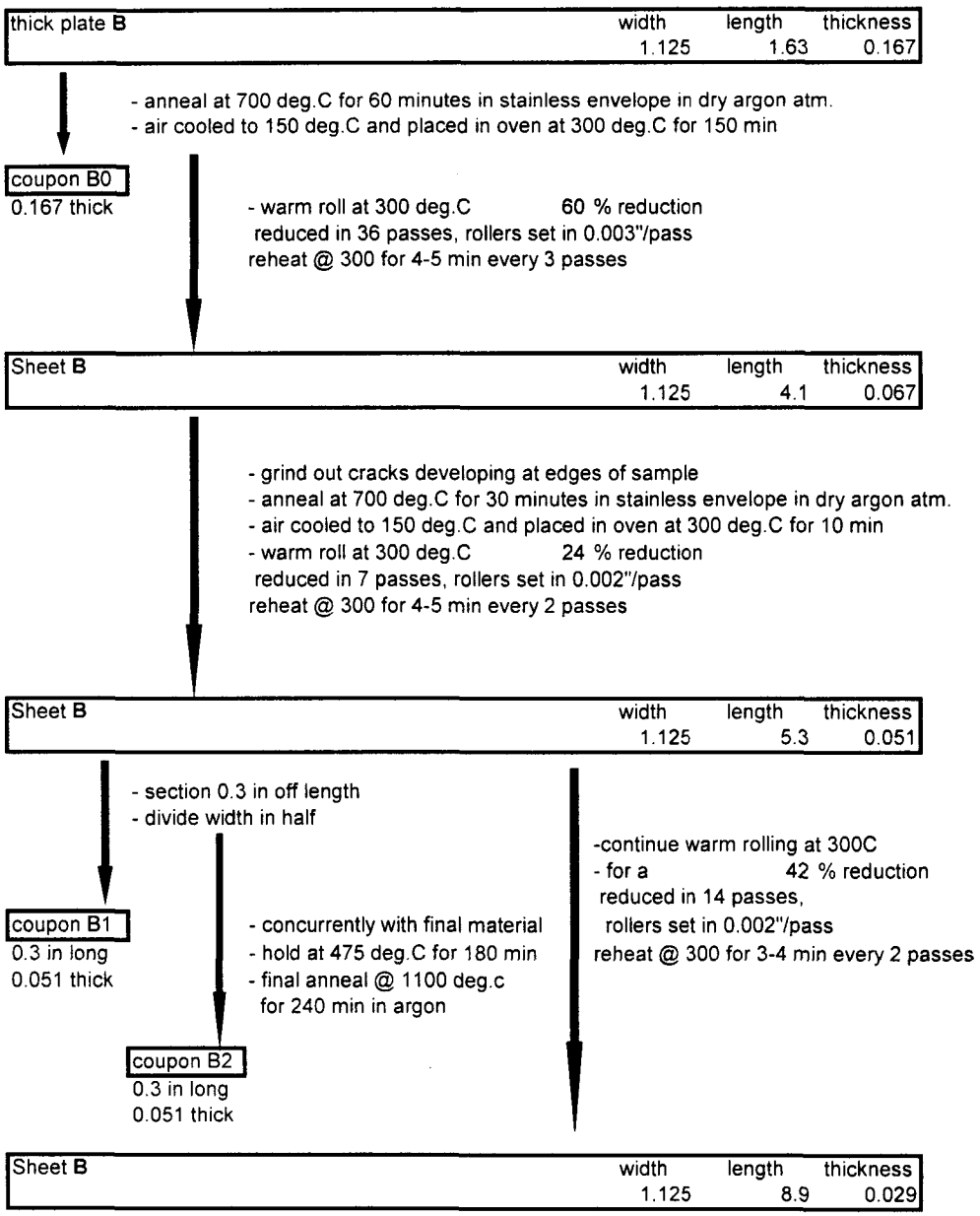

Nishihara texturing process, Patent# 3,279,960 (designed for 2-6%wt Al) revised 1/18/02 page B2

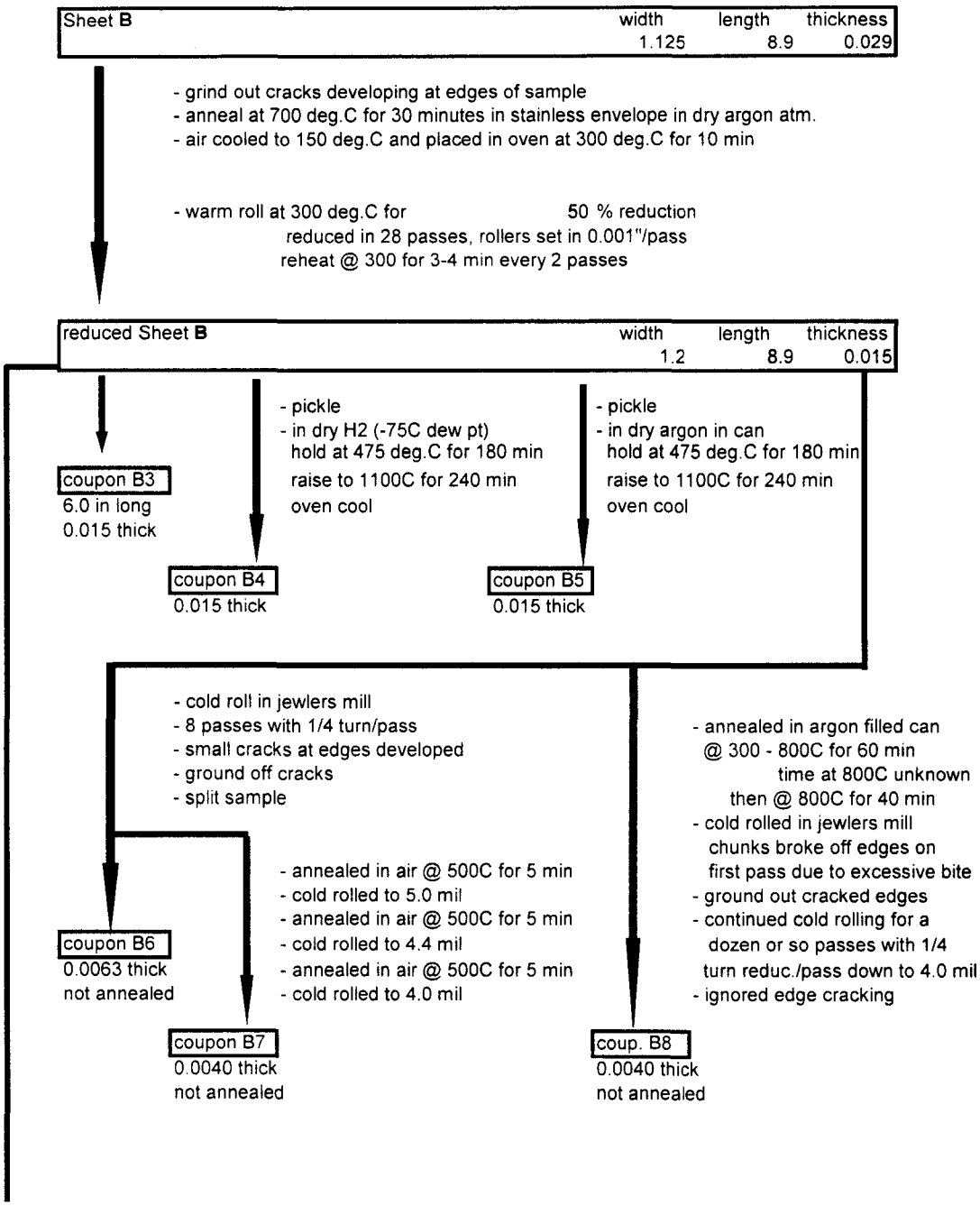

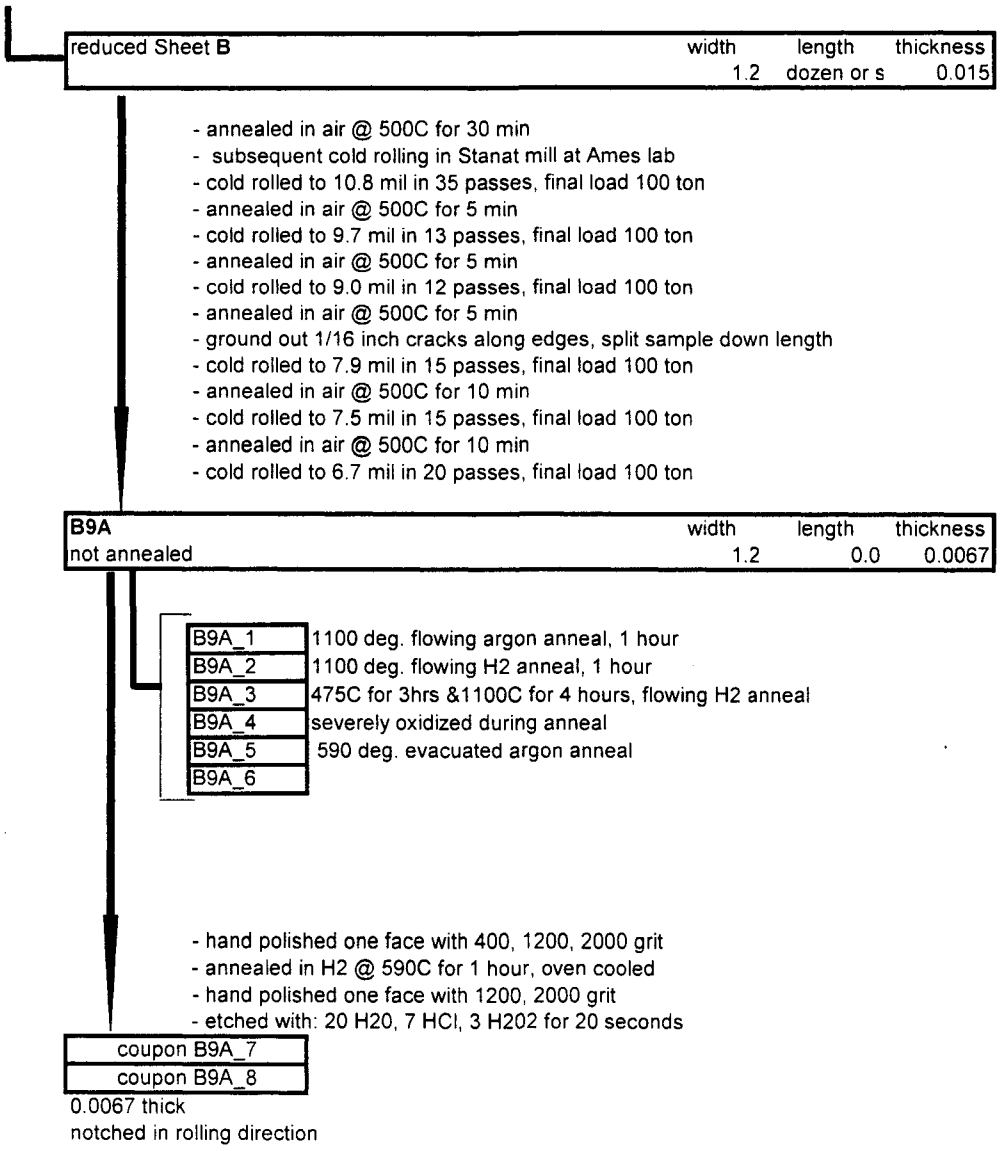
reduced Sheet B
width 1.2
length dozen or s
thickness 0.015
- annealed in air @ 500C for 30 min
- subsequent cold rolling in Stanat mill at Ames lab
- cold rolled to 10.8 mil in 35 passes, final load 100 ton
- annealed in air @ 500C for 5 min
- cold rolled to 9.7 mil in 13 passes, final load 100 ton
- annealed in air @ 500C for 5 min
- cold rolled to 9.0 mil in 12 passes, final load 100 ton
- annealed in air @ 500C for 5 min
- ground out 1/16 inch cracks along edges, split sample down length
- cold rolled to 7.9 mil in 15 passes, final load 100 ton
- annealed in air @ 500C for 10 min
- cold rolled to 7.5 mil in 15 passes, final load 100 ton
- annealed in air @ 500C for 10 min
- cold rolled to 6.7 mil in 20 passes, final load 100 ton
B9A
not annealed
width 1.2
length 0.0
thickness 0.0067
B9A_1
B9A_2
B9A_3
B9A_4
B9A_5
B9A_6
1100 deg. flowing argon anneal, 1 hour
1100 deg. flowing H2 anneal, 1 hour
475C for 3hrs &1100C for 4 hours, flowing H2 anneal
severely oxidized during anneal
590 deg. evacuated argon anneal
- hand polished one face with 400, 1200, 2000 grit
- annealed in H2 @ 590C for 1 hour, oven cooled
- hand polished one face with 1200, 2000 grit
- etched with: 20 H20, 7 HCl, 3 H202 for 20 seconds
coupon B9A_7
coupon B9A_8
0.0067 thick
notched in rolling direction

APPENDIX B: $Fe_{81}Ga_{19}$ SINGLE-CRYSTAL MAGNETIC RESPONSE

The quasi-static magnetic response of $Fe_{81.0}Ga_{19.0}$ single crystal was examined at compressive stresses of 14.4, 45.3 and 87.1 MPa and temperatures of -21, 22, 50 and 80°C. Magnetostriction and material induction were recorded as a function of applied magnetic field. All measurements were made at 0.05 Hz in the thermally controlled transducer (Chapter 3). To facilitate comparison of magnetization and magnetostriction curves, two types of plots are presented using the same source data. The first type includes various stress levels at constant temperature and the second type includes various temperature levels at constant stress.

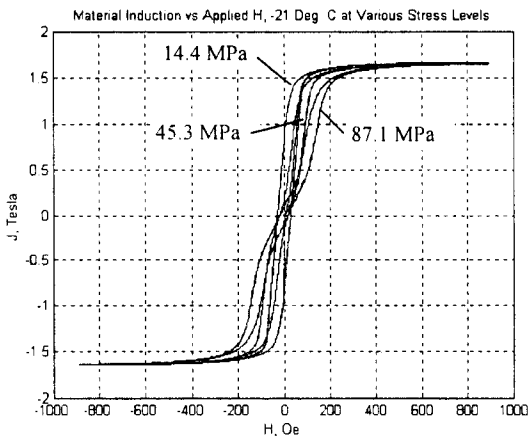

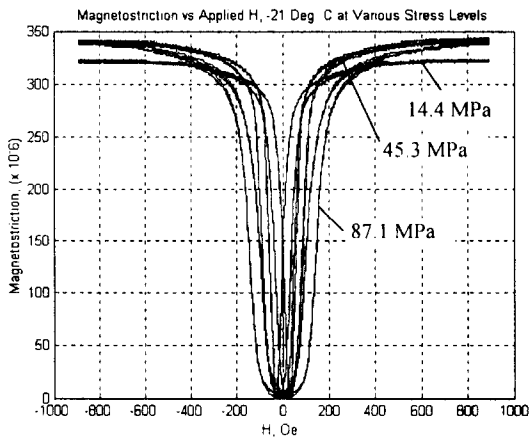

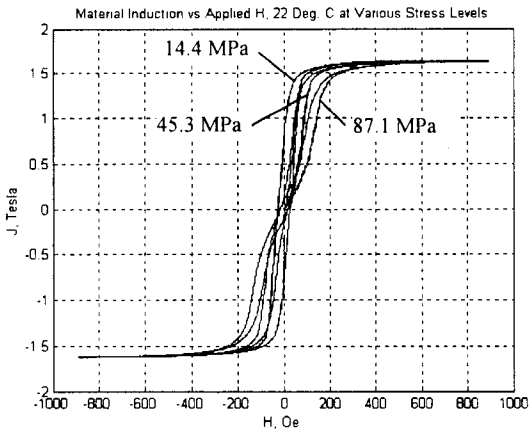
Material Induction vs Applied H, 22 Deg. C at Various Stress Levels
14.4 MPa
45.3 MPa
87.1 MPa
J, Tesla
H, Oe

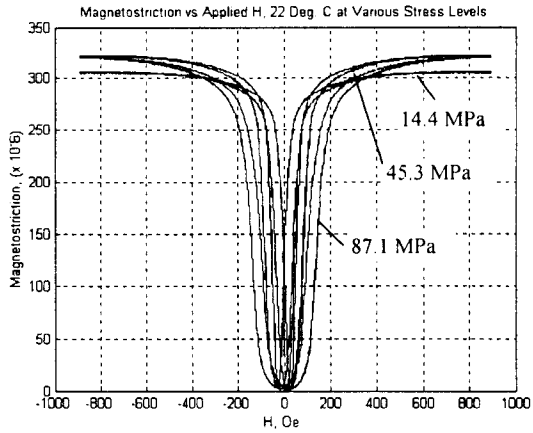
Magnetostriction vs Applied H, 22 Deg. C at Various Stress Levels
14.4 MPa
45.3 MPa
87.1 MPa
Magnetostriction, (x 10^6)
H, Oe

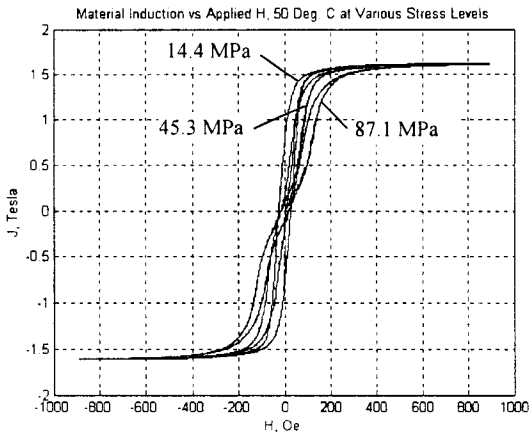
Material Induction vs Applied H, 50 Deg. C at Various Stress Levels
14.4 MPa
45.3 MPa
87.1 MPa
J, Tesla
H, Oe

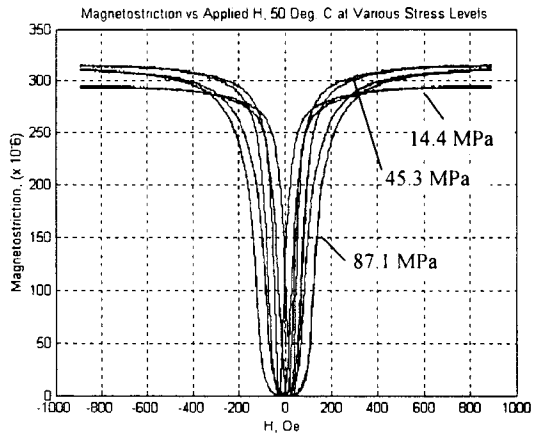
Magnetostriction vs Applied H, 50 Deg. C at Various Stress Levels
14.4 MPa
45.3 MPa
87.1 MPa
Magnetostriction, (x 10^6)
H, Oe

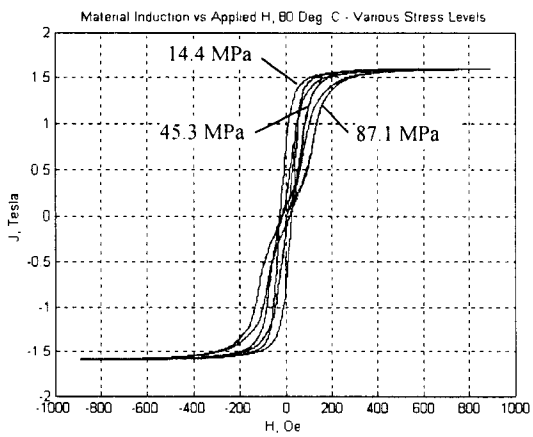
Material Induction vs Applied H, 80 Deg. C - Various Stress Levels
14.4 MPa
45.3 MPa
87.1 MPa
J, Tesla
H, Oe

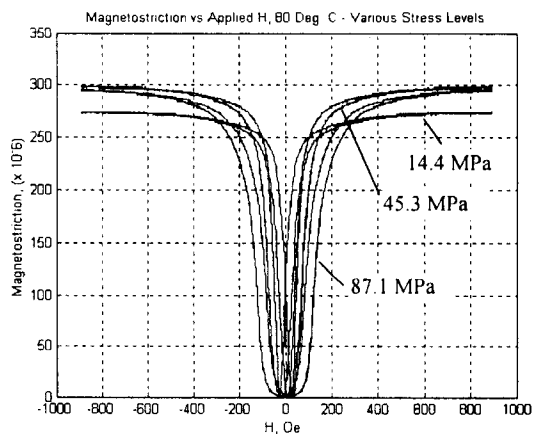
Magnetostriction vs Applied H, 80 Deg. C - Various Stress Levels
14.4 MPa
45.3 MPa
87.1 MPa
Magnetostriction, (x 10^6)
H, Oe

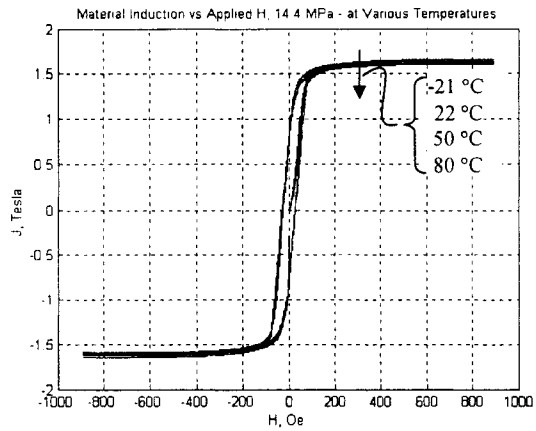
Material Induction vs Applied H, 14 4 MPa - at Various Temperatures
J, Tesla
H, Oe
-21 °C
22 °C
50 °C
80 °C

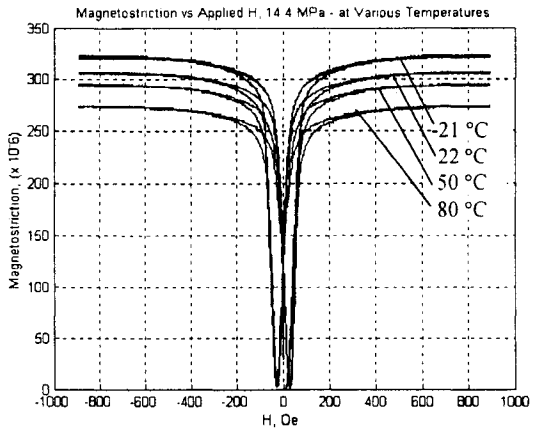
Magnetostriction vs Applied H, 14 4 MPa - at Various Temperatures
Magnetostriction, (x 10 6)
H, Oe
-21 °C
22 °C
50 °C
80 °C

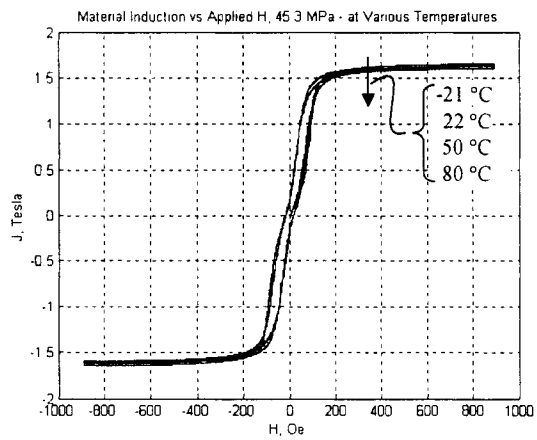
Material Induction vs Applied H, 45 3 MPa - at Various Temperatures
J, Tesla
H, Oe
-21 °C
22 °C
50 °C
80 °C

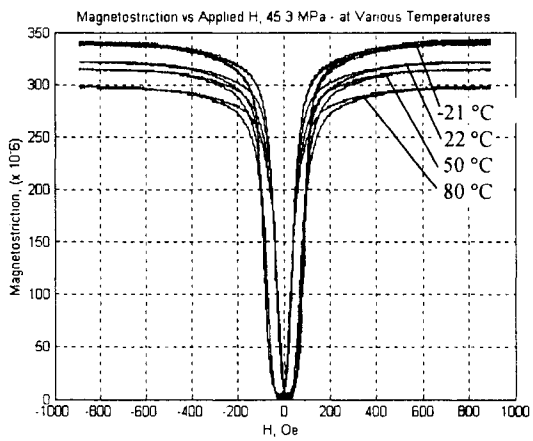
Magnetostriction vs Applied H, 45 3 MPa - at Various Temperatures
Magnetostriction, (x 10 6)
H, Oe
-21 °C
22 °C
50 °C
80 °C

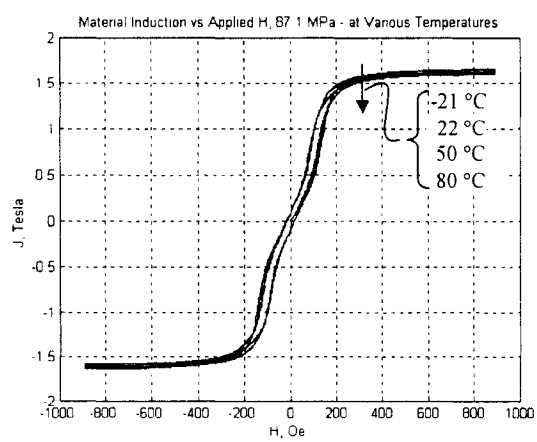
Material Induction vs Applied H, 87 1 MPa - at Various Temperatures
J, Tesla
H, Oe
-21 °C
22 °C
50 °C
80 °C

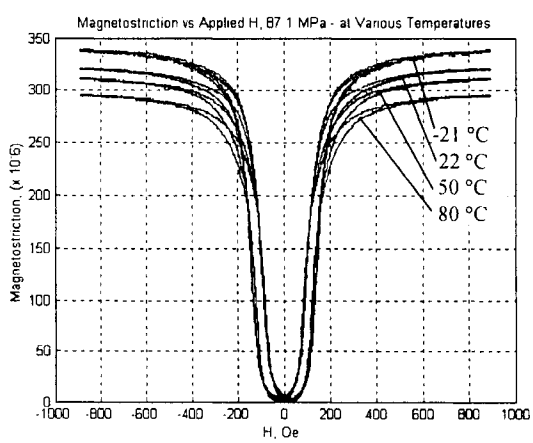
Magnetostriction vs Applied H, 87 1 MPa - at Various Temperatures
Magnetostriction, (x 10 6)
H, Oe
-21 °C
22 °C
50 °C
80 °C

APPENDIX C: POISSON'S RATIOS OF Fe-Al ALLOYS

Calculated Poisson's ratios and quadratic fits for [110] loading of $Fe_{100-x}Al_x$, where $x = 0 \leq x \leq 40.1$. The Poisson's ratios $\nu_{[1\bar{1}0]}$ and $\nu_{[001]}$ are in orthogonal directions which lie respectively in the (001) and $(1\bar{1}0)$ planes (see schematic of Figure 6.2). Their values are calculated from Equations 1.20 and 1.21 using data in Table A.1. The trend lines are based on data excluding the highest four Al substitution levels.

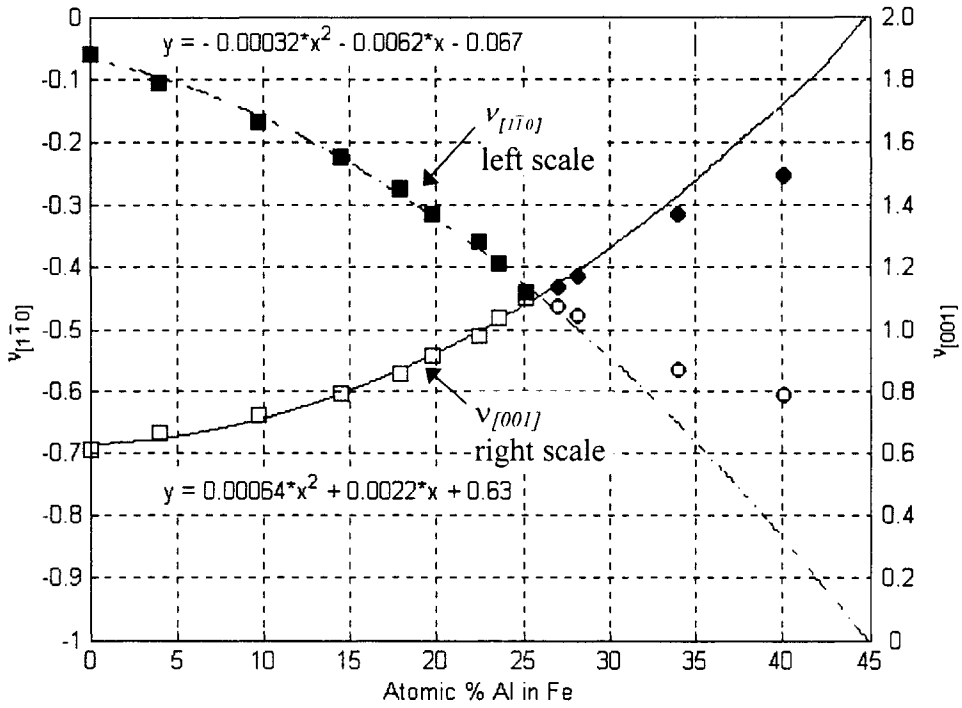

Table A.1 Elastic constants for cubic Fe-Al.

at.% Al	0	4.0	9.7	14.5	17.9	19.8	22.4
c_{11} GPa	228.0	220.9	205.2	193.8	185.4	179.5	174.3
c_{12} GPa	132.0	132.5	127.2	125.0	124.6	124.9	125.5
c_{44} GPa	116.5	120.2	122.6	124.3	125.2	125.5	126.2

at.% Al	23.6	25.1	27.0	28.1	34.0	40.1
c_{11} GPa	174.8	171.0	166.5	166.3	171.8	181.1
c_{12} GPa	130.0	130.6	125.1	122.5	113.6	113.7
c_{44} GPa	128.2	131.7	130.6	131.0	129.5	127.1

REFERENCES

Alderson, A., "A triumph of lateral thought," Chemistry and Industry, May 17, 1999.

Baker, I., Wu, D., and George, E.P., "The low temperature tensile behavior of FeAl single crystals," Structural Intermetallics, p. 279-288, 2001.

Barrett, C.S., and Levenson, L.H., AIME Trans. **135** p.296, 1939.

Barrett, C.S., *Structure of Metals, 2nd Ed.*, (McGraw-Hill Book Co., 1952)

Baughman, R.H., Shacklette, J.M., Zakhidov, A. A., and Stafstrom, S., "Negative Poisson's ratios as a common feature of cubic metals," Letters to Nature **392** p. 362-365, 1998.

Bily, M., Ed., *Cyclic Deformation and Fatigue of Metals*, (Elsevier, New York, 1993).

Birkenbeil, H.J., and Cahn, R.W., "Induced magnetic anisotropy created by magnetic of stress annealing of iron-aluminum alloys," Journal of Applied Physics, **32** p. 362S-363S, 1961.

Boresi, A.P., Schmidt, R.J., Sidebottom, O.M., *Advanced Mechanics of Materials, 5th ed.*, (John Wiley & Sons, Inc., New York. 1993), Chapter 2.

Bozorth, R.M., *Ferromagnetism*, (Van Nostrand, New York, 1951), p. 968.

Bowman, H.B., *Handbook of Precision Sheet, Strip and Foil*, (American Society for Metals, Metal Park Ohio, 1980).

Butler, J.L., *Application Manual for the Design of Etrema Terfenol-D Magnetostrictive Transducers*, (Etrema Poducts, Inc., Ames, Iowa, 1988).

Calkins, F.T., *Design, Analysis, and Modeling of Giant Magnetostrictive Transducers*, (Ph.D dissertation, Iowa State University, Ames, Iowa, 1997).

Callen, H.B., and Goldberg, N., "Magnetostriction of polycrystalline aggregates," Journal of Applied Physics, **36** p. 976 - 977, 1965.

Chandrupatla, T.R., and Belegundu, A.D., *Introduction to Finite Elements in Engineering*, 2nd ed. (Prentice Hall, Englewood Cliffs, NJ, 1991).

Clark, A.E., "Magnetostrictive rare earth-Fe2 compounds," *Ferromagnetic Materials*, Volume 1, E. P. Whohlfarth, editor, (North-Holland Publishing Company, Amsterdam, 1980), p. 531-589.

Clark, A.E., Wun-Fogle, M., Restorff, J.B., Lograsso, T.A., Ross, A.R., and Schlagel, D.L., "Magnetostrictive Galfenol/Alfenol single crystal alloys under large compressive stresses," Actuator 2000, submitted March 29, 2000a.

Clark, A.E., Wun-Fogle, M., Restorff, J.B., Lograsso, T.A., and Schlagel, D.L., "Magnetostrictive properties of b.c.c. Fe-Ga and Fe-Ga-Al alloys," *Proceedings of the Intermag 2000 Conference*, Toronto, Canada, April 10-13, 2000b.

Clark, A.E., Restorff, J.B., Wun-Fogle, M., Lograsso, T.A., and Schlagel, D.L., "Magnetostrictive properties of body-centered cubic Fe-Ga and Fe-Ga-Al alloys," IEEE Transactions on Magnetics, **36** p. 3238-3240, 2000c.

Clark, A.E., Wun-Fogle, M., Restorff, J.B., Lograsso, T.A., and Cullen, J.R., "Effect of quenching on the magnetostriction of $Fe_{1-x}Ga_x$ ($0.13<x<0.21$)," *8th Joint MMM-Intermag Conference*, Jan 7 - 11, 2001.

Clark, A.E., Wun-Fogle, M., Restorff, J.B., and Lograsso, T.A., Proc. Pacific Rim International Conference on Advanced Materials and Processing, Honolulu, Hawaii, Dec. 11-15, 2001b.

Clark, A.E., Restorff, J.B., Wun-Fogle, M., and Lograsso, T.A., "Magnetostrictive properties of Galfenol alloys under compressive stress," Materials Transactions (Japan) **43** p. 881-886, 2002a.

Clark, A.E., Hathaway, K.B., Wun-Fogle, M., Restorff, J.B., Lograsso, T.A., Keppens, V.M., Petculescu, G., and Taylor, R.A., Journal of Applied Physics, **93** p. 8621, 2003.

Cox, J.J., Mehl, R.F., and Horne, G.T., Trans. Am. Soc. Met. **49** 118, 1957.

Cullen, J.R., Clark, A.E., WunFogle, M., Restorff, J.B., and Lograsso, T.A., "Magnetoelasticity of Fe-Ga and Fe-Al alloys," ICM Abstract Designation 1G-02, no date.

Cullen, J.R., Clark, A.E., Wun-Fogle, M., Restorff, J.B., and Lograsso, T.A., "Magnetoelasticity of Fe-Ga and Fe-Al alloys," Journal of Magnetism and Magnetic Matererials, **226** p. 948-949, 2001.

Cullity, B.D., *Introduction to Magnetic Materials*, (Addison-Wesly Publishing Co., Reading MA, 1972), Chapter 8.

Dieter, G.E., *Mechanical Metallurgy: SI Metric Edition*, (McGraw-Hill, London, 1988), p. 126.

Dunn, C.G., and Walter, J.L., "Surface energies and other surface effects relating to secondary recrystallization textures in high-purity iron, zone-refined iron and 0.6 pct. Si-Fe," Transaction of the Metallurgical Society of AIME, **224** p. 518 – 533, June 1962.

Gibson, R.F., *Principles of Composite Material Mechanics*, (McGraw-Hill, New York, 1994).

Hall, R.C., "Single crystal anisotropy and magnetostriction constants of several ferromagnetic materials including alloys of NiFe, SiFe, AlFe, CoNi, and CoFe," Journal of Applied Physics, **30**(6) p. 816 - 819, June 1959.

Hall, R.C., "Single crystal magnetic anisotropy and magnetostriction studies in iron-based alloys," Journal of Applied Physics, **31**(6) p. 1037 - 1038, June 1960.

Honda, K., Kaya, S., "On the magnetization of single crystals of iron," Sci. Reports, Tohoku Univ., p. 721 – 753, 1926.

Jain, M. and Verma, M.P., "Poisson's ratios in cubic crystals corresponding to (110) loading," Indian Journal of Pure and Applied Physics, **28** p. 178-182, 1990.

Jiles, D.C., Atherton, D.L., "Theory of ferromagnetic hysteresis," Journal of Magnetism and Magnetic Materials, **61** p. 48 - 60, June 1986.

Jiles, D.C., "Theory of the magnetomechanical effect," Physics D: Applied Physics, **28** p. 1537 - 1546, 1995.

Jiles, D.C., *Introduction to Magnetism and Magnetic Materials, Second Edition*, (Chapman & Hall, London, 1998).

Jimenez, J.A., Frech, W., Ruano, O.A., and Frommeyer, G., "Microstructure and mechanical properties of rapidly solidified Fe-25%Cr-5%Al ribbons produced by planar flow casting," Steel Research, **66**(6) p. 251 – 253, June 1995.

JCPDS – International Centre for Diffraction Data, PCPDFWIN v. 1.30, 1997.

Kad, B.K., Schoenfeld, S.E., Asaro, R.J., McKamey, C.G., and Sikka, V.K., "Deformation textures in Fe_3Al alloys," Acta Maerialia **45** p. 1333-1350, 1997.

Kawamiya, N., Adachi, K., Nakamura, Y., "Magnetic properties and Mossbauer investigations of Fe-Ga alloys," Journal of the Physical Society of Japan, **33**(5) p. 1318 - 1327, Nov. 1972.

Kellogg, R.A., and Flatau, A.B., "Blocked force investigation of a Terfenol-D transducer," Proc. SPIE **3668** p. 184-195, 1999.

Kellogg, R.A., *The Delta-E Effect in Terfenol-D and its Application in a Tunable Mechanical Resonator*, (Masters Thesis, Iowa State University, August 2000).

Kellogg, R.A., Flatau, A.B., Clark, A.E., Wun-Fogle, M., and Lograsso, T.A., "Temperature and stress dependencies of the magnetic and magnetostrictive properties of $Fe_{81}Ga_{19}$," Journal of Applied Physics, **91** p. 7821 2002.

Kinkaid, N.M., "Pulling apart a press-fitted joint, Mathematics and Mechanics of Solids," **7** p. 307-318, 2002.

Kittel, C., "Physical theory of ferromagnetic domains," Reviews of Modern Physics, **21** p. 541-583, 1949.

Kramer, J.L., "Nucleation and growth effects in thin ferromagnetic sheets: a review focusing on surface energy-induced secondary recrystallization," Metallurgical Transactions A, **23A** p. 1987 - 1992, July 1992.

Kumar, S., Kurtz, S.K., Banavar, J.R, and Sharma, M.G., "Properties of a three-dimensional Poisson-Voronoi tesselation: a Monte Carlo study," Journal of Statistical Physics, **67** p. 523-551, 1992.

Kubaschewski, O., *Iron - Binary Phase Diagrams*, (Springer-Verlag Berlin Heidelberg, New York, 1982).

Kurzydlowski, K.J., Ralph, B., Bucki, J.J., Garbacz, A., "Grain boundary character distribution on the flow stress of polycrystals: The influence of crystal lattice texture," Materials Science and Engineering A, **A205**(1-2) p. 127-132, January 1996.

Lakes, R.S., Park, J.B., and Friis, E.A., Proc. Amer. Soc. Compos 3-rd Tecj. Conf., Basel, p. 527-533, 1988.

Leamy, H., Gibson, E.D., and Kayser, F.X., "The elastic stiffness coefficients of iron-aluminum alloys - I Experimental results and thermodynamic analysis," Acta Metallurgica, **15** p. 1827-1837, December 1967a.

Leber, C.S., ASM Trans., **53** p. 697, 1961.

Lograsso, T.A., Unpublished results from preliminary tension tests to failure of polycrystalline Galfenol, Iowa State University, Fall, 2000.

Lograsso, T.A. Ross, A.R. Schlagel, D.L., Clark, A.E., and Wun-Fogle, M., "Structural transformations in quenched Fe-Ga alloys," Journal of Alloys and Compounds, **350** p. 95-101, 2003.

Lyman, T., Ed., *Metals Handbook, 1948 Edition*, (American Society for Metals, Cleveland, Ohio, 1948).

Mason, W. P. *Physical Acoustics and the Properties of Solids*, (D. Van Nostrand Princeton, New Jersey 1958), A1.

Massalski, T., Editor, *Binary Alloy Phase Diagrams 2nd Ed.*, (ASM International, Materials Park, Ohio, 2002).

McLean, D., *Mechanical Properties of Metals*, (John Wiley & Sons, Inc., New York, 1962).

McLean, K.O., and Smith, C. S., Journal of Physics and Chemical Solids (USA) **33** p. 279, 1972.

Milstein, F., and Huang, K. "Existence of a negative Poisson ratio in fcc crystals," Physical Review B, **19** p. 2030-2033, 1979.

Moffatt, W.G., Pearsall,G.W., and Wulff, J., *The Structure and Properties of Materials, Vol I*, (John Wiley & Sons, Inc., New York, 1964).

Nachman, J.F., and Buehler, W.J., "16 Percent aluminum-iron alloy cold rolled in the order-disorder temperature range," Journal of Applied Physics, **25** p. 307-313, March 1954.

Nabarro, F., Proc. R. Soc. (London) A **381** p. 285, 1982.

Novikov, V., *Grain Growth and Control of Microstructure and Texture in Polycrystalline Materials*, (CRC Press, New York, 1997).

Nye, J.F., *Physical Properties of Crystals*, (Clarendon, Oxford, 1985).

Orlans-Joliet, B., Driver, J.H., Montheillet, F., "Plane strain compression of silicon-iron single crystals," Acta Metallurgica **38** p. 581-594, 1990.

Prasad, Y.V., "Texture dependent mechanical properties of metals and alloys," Transactions of the Indian Institute of Metals, **37**(4) p. 399 - 410, Aug. 1994.

Random House, *College Dictionary*, Revised Ed. 1980.

Rhines, F.N., and Craig, K.R., "Mechanism of steady-state grain growth in aluminum," Metallurgical Transactions, **5A** p. 413-425, 1974.

Rovati, M., "On the negative Poisson's ratio of an orthorhombic alloy," Scripta Materialia, **48** p. 235-240, 2003.

Smith, C.S., *Metal Interfaces*, (American Society for Metals, Cleveland, Ohio, 1952).

Sawyer, B., and Smoluchowski, R., Journal of Applied Physics, **28** p. 1069, 1957.

Smoluchowski, R., and Turner, R.W., Journal of Applied Physics, **20** p. 745, 1949.

Shilko, S.V., "Friction of anomalously elastic bodies, negative Poisson's ratio, part 1 self-locking effect," Journal of Friction and Wear, **16** p. 19-25, 1995.

Shull, R.D., Okamoto, H., and Beck, P.A., "Transition from ferromagnetism to mictomagnetism in Fe-Al alloys," Solid State Communications, **20** p. 863-868, 1976.

Stephens, R.I., Fatemi, A., Stephens, R.R., and Fuchs, H.O., *Metal Fatigue in Engineering, 2nd Ed.*, (John Wiley & Sons, Inc., New York, 2001).

Tatsumoto. E., and Okamoto, T., "Temperature dependence of magnetostriction constants in iron and silicon iron," Journal of the Physical Society of Japan, **14**(11) p. 1588-1599, 1959.

Titorov, D.B., "Texture as a factor of improving the technological properties of materials," Metal Science and Heat Treatment, **29**(11-12) p 840-843, May 1998.

Waeckerle, T., Couty, J.M., Comut, B., and Brun, C., "Effect of process on the rise of texture in magnetic iron sheets," IEEE Transactions on Magnetics, **29** p. 3538- 3540, 1993.

Walter, J.L., "Control of texture in magnetic material by surface energy," Journal of Applied Physics, **36** p. 1213-1220, 1965.

Wu, D., and Baker, I., "Effect of environment and strain rate on the room temperature tensile properties of FeAl single crystals," Intermetallics, **9** p. 57-65, 2001.

Wu, R., "Origin of large magnetostriction on Fe-Ga alloys," Journal of Applied Physics, **91** p. 7358-7360, May 2002.